MEMS BASED RESONANT MASS SENSORS WITH FEEDTHROUGH CURRENT ELIMINATION FOR IN-LIQUID CELL DETECTION APPLICATIONS

A THESIS SUBMITTED TO
THE GRADUATE SCHOOL OF NATURAL AND APPLIED SCIENCES
OF
MIDDLE EAST TECHNICAL UNIVERSITY

BY

MUSTAFA KANGÜL

IN PARTIAL FULFILLMENT OF THE REQUIREMENTS
FOR
THE DEGREE OF MASTER OF SCIENCE
IN
ELECTRICAL AND ELECTRONICS ENGINEERING

SEPTEMBER 2015

Approval of the thesis:

MEMS BASED RESONANT MASS SENSORS WITH FEEDTHROUGH CURRENT ELIMINATION FOR IN-LIQUID CELL DETECTION APPLICATIONS

submitted by **MUSTAFA KANGÜL** in partial fulfillment of the requirements for the degree of **Master of Science in Electrical and Electronics Engineering Department, Middle East Technical University** by,

Prof. Dr. Gülbin Dural Ünver
Dean, Graduate School of **Natural and Applied Sciences**

Prof. Dr. Gönül Turhan Sayan
Head of Department, **Electrical and Electronics Engineering**

Prof. Dr. Haluk Külah
Supervisor, **Electrical and Electronics Eng. Dept., METU**

Examining Committee Members:

Prof. Dr. Tayfun Akın
Electrical and Electronics Engineering Dept., METU

Prof. Dr. Haluk Külah
Electrical and Electronics Engineering Dept., METU

Assoc. Prof. Yeşim Serinağaoğlu Doğrusöz
Electrical and Electronics Engineering Dept., METU

Asst. Prof. Dr. Kıvanç Azgın
Electrical and Electronics Engineering Dept., METU

Asst. Prof. Dr. M. Yusuf Tanrıkulu
Electrical and Electronics Engineering Dept., Adana STU

Date:

I hereby declare that all information in this document has been obtained and presented in accordance with academic rules and ethical conduct. I also declare that, as required by these rules and conduct, I have fully cited and referenced all material and results that are not original to this work.

Name, Lastname: Mustafa Kangül

Signature:

ABSTRACT

DEVELOPMENT OF
RESONANT MASS SENSORS FOR MEMS BASED
REAL TIME CELL DETECTION APPLICATIONS

Kangül, Mustafa

M. S., Department of Electrical and Electronics Engineering

Supervisor: Prof. Dr. Haluk Külah

September 2015, 98 pages

This thesis represents design and implementation of MEMS based resonant mass sensors for cell detection applications. The main objective of the thesis is real-time detection inside liquid medium and obtaining the results by electronic means, without the assistance of bulky optical instruments.

Novel resonant based mass sensor architectures that have various improvements over selected benchmark design are presented. Purpose of the new structures is to establish real-time mass detection by improving the quality factor, increasing the sensor gain and eliminating the feedthrough current effect. Proposed sensors oscillate in the lateral direction and are coated with a thin parylene layer to prevent liquids flow through the narrow gaps of the device, further improving the quality factor. The resonator is located on top of a microchannel. A thin gold film on the oscillating proof mass is employed as an antibody based cell capture surface.

Theoretical background of the physical resonators is investigated to diagnose the design issues of the sensors in the literature. Capacitive actuation, sensing optimization, and feedthrough current elimination methods are presented. In the

light of these theoretical studies and finite element modeling simulations, four new resonating structures are proposed for the purpose of real-time mass sensing by enabling self-oscillation.

A new process flow consisting SOI, glass, and polymer micromachining methods has been utilized for resonator fabrication. Each device has a foot print area of 18 x 6 mm^2, a significant percent of which is used for the inlet and outlet connections of the microchannels.

Resonance characterization results in air are presented to see the improvements over the benchmark design, which is previously developed in METU BioMEMS research group. Total sensor mass has been decreased without any loss in the sensor gain. Even two orders of magnitude increase in the gain is achieved with the same mass. There is also quality factor enhancement up to ten times. These improvements are established without changing the anchor structure or cell capturing surface area of the benchmark design. Feedthrough current is also eliminated to make self-oscillation possible. According to the conducted mass measurement results, the mass of a single Sigma-Aldrich® polystyrene microbead is 0.53 ng, whereas the mass is given as 0.55 ng ±30% in its datasheet. In-liquid functionality was also tested. The quality factor of the sensor is reduced from 402, in air, to only to 183 in wet environment. Reported improvements enable real time cell detection in liquid environment.

Keywords: Resonant mass sensor, cell detection, parylene, hydrophobic coating, quality factor improvement, microresonator, fabrication of suspended structures.

ÖZ

SIVI ORTAMDA HÜCRE TESPİTİ UYGULAMALARI İÇİN KAÇAK AKIMI ELEYEN MEMS TABANLI RESONANT KÜTLE SENSÖRLERİ

Kangül, Mustafa

Yüksek Lisans, Elektrik ve Elektronik Mühendisliği Bölümü

Tez Yöneticisi: Prof. Dr. Haluk Külah

Eylül 2015, 98 sayfa

Bu tez gerçek zamanli hücre tespiti uygulamalari için MEMS tabanli ataletsel rezonatör sensörleri geliştirilmesini anlatmaktadır. Tezin temel amacı optik cihazlar kullanmadan, eletronik arayüz sayesinde sıvı ortamda gerçek zamanlı tespit yapabilmektir.

Kıyaslanabilecek tasarımlara göre bir çok iyileştirmesi olan özgün resonatör temelli kütle sensor yapıları sunulmuştur. Yeni yapıların amacı sensör kazancını ve kalite faktörünü arttırıp elektrik akımını da eleyip gerçek zamanlı tespiti mümkün kılmaktır. Önerilen sensörler yatay düzlemde salınırlar ve boşluklara sıvı dolmasını engelleyen ince bir parilen katman ile kaplanmışlardır. Rezonatörler mikrokanalın üzerine yerletirilmiştir. Salınım yapan kütlenin üzerindeki ince bir altın film antibody kullanarak hücre yakalamayı mümkün kılmaktadır.

Fiziksel rezönatör yapılarının teorik altyapısı araştırılmıştır. Bu sayede literatürdeki sensörlerin eksikliklerinin tanısı konulmuştur. Kapasitif harekete geçirme ve algılama optimizasyonları yapılmış, istenmeyen çıkış akımlarını elemek için metodlar önerilmiştir. Bu bilgiler ışığında dört yeni rezönatör yapısı tasarlanmıştır.

SOI, cam ve polimer üretim teknikleri kullanılarak oluşturulan üretim şeması verilmiştir. Üretilen her cihaz 18 x 6 mm^2 lik alan kaplamaktadır.

Sensörlerin havadaki rezonans karakteristikleri çıkarılmış, literature göre kaydedilen ilerlemeler tespit edilmiştir. Sensör kazancının büyüklüğü sensör kütlesi değiştirilmeden 100 kata kadar arttırılmıştır. Kalite faktörü de 10 katına kadar çıkarılmıştır. Bu iyileştirmeler hücre yakalamak için ayrılmış alanda ya da asılı duran sensörü tutan yapılarda herhangi bir değişiklik yapılmadan elde edilmiştir. Kütle ölçümü deneyi mikro parçacıklarla yapılmış ve bir tanesinin ağırlığı 0.53 ng olarak ölçülmüştür. Sıvı ortamdaki performansı da test edilmiş olup havada 402 olarak ölçülen kalite faktörünün sadece 183'e düştüğü gözlenmiştir. Raporlanan bu gelişmeler için gerçek zamanlı hücre tespiti mümkün kılınmıştır.

Anahtar Kelimeler: Ataletsel rezönatör, hücre algılama, parylene hidrofobik kaplama, kalite faktörü iyileştirilmesi, havada asılı yapıların üretilmesi.

To my family

ACKNOWLEDGEMENTS

TABLE OF CONTENTS

LIST OF TABLES

TABLES

LIST OF FIGURES

FIGURES

CHAPTER 1

INTRODUCTION

Improvements in IC fabrication techniques open the doors between reality and one of the fascinating fictions: making non-visibly small tools. Famous physicist Feynman expressed his enthusiasm on infinitesimal machines by saying that "(small but movable machines) may or may not be useful, but they surely would be fun to make". Micro Electro Mechanic Systems (MEMS) not only have been fun to make but also have changed daily habits of the society by introducing handy tools. Today, MEMS market reaches over \$10B with devices such as; inkjets, pressure sensors, inertial sensors and projection systems.

Future size of MEMS fabrication grabbed the attention of bio-researchers. Comparable dimensions of MEMS with biological and chemical particles were convincible enough to lead a new research area: biomedical microelectromechanical systems (BioMEMS) (Figure 1-1).
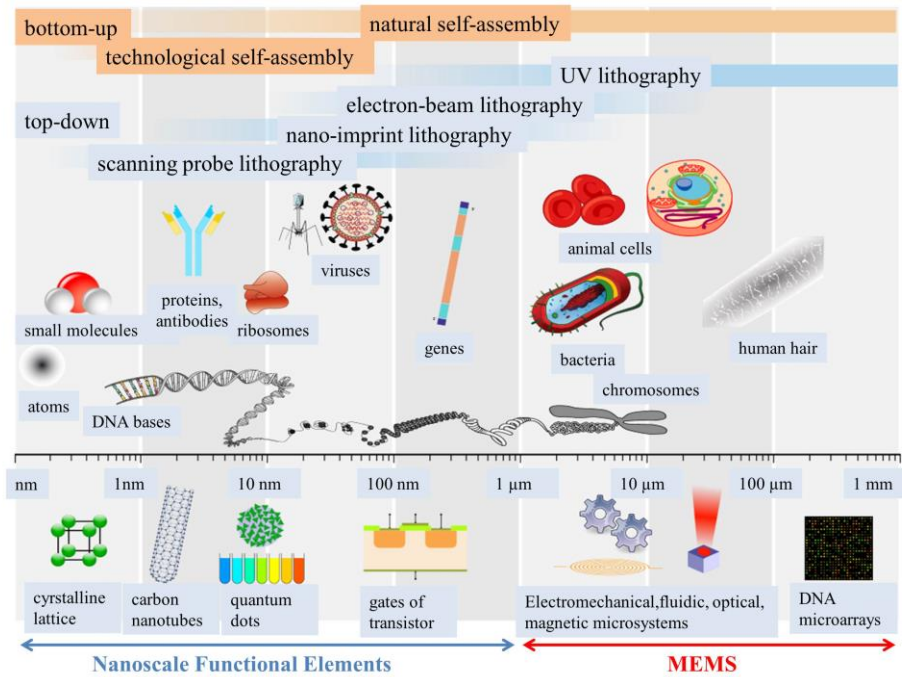
Figure 1-1 Dimensions of microsystems and biological agents [1]

Realization of the significance of the utilizing MEMS technology in biomedical applications makes BioMEMS an extremely important researched area with a wide variety of applications [2]. Focus of the BioMEMS research is to develop micro-devices with abilities of detection, separation, and any kind of manipulation of the biological or chemical units.

In order to understand the importance of BioMEMS, its advantages over macro scale counterparts should be analyzed. These advantages can be listed as [3]:

- less reagent consumption (at the order of microliters or nanoliters),
- better sensitivity,
- reduced analysis durations,
- enhanced heat transfer due to higher surface area-to-volume ratio,
- point-of-care analysis feasibility,
- portability due to low weight and low power consumption,
- *in-vivo* and *in-vitro* usage possibility, and

- improved safety (trace amounts of hazardous chemical material is used in micro analysis systems.).

Some of the BioMEMS originated devices can also be named as Lab-on-a-chip (LoC) or micro total analysis systems (μTAS). As the names imply shrinking a biological analyze laboratory inside a microchip is the eventual point of the related devices. LoC devices consists of several parts that are connected each other by microchannel. Each part is responsible for a unique job. Heating, mixing, separating and counting the target particles are some of the objectives of LoC parts. Figure 1-2 shows a LoC example.
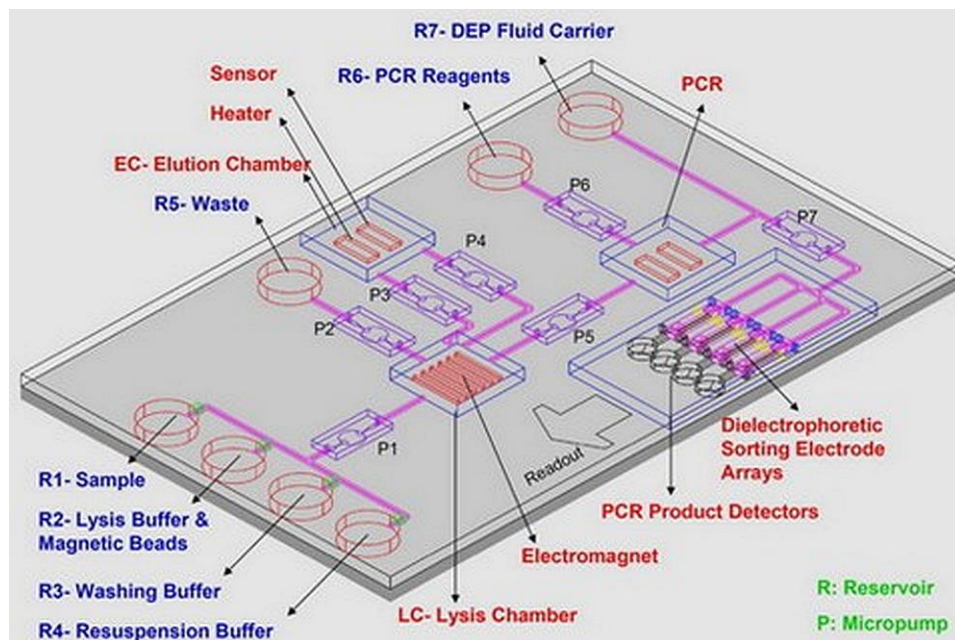
Figure 1-2 An LoC diagram indicating typical components

Detection and quantization of biological or chemical entities is one of the most exciting and promising subject that is studied in the scope of BioMEMS[4]. Virus detection (HIV, HBV) [5]–[7], cancer cell detection [8], [9], and specific blood cell detection (Leukocytes) [10] are some of the breakthrough examples in the literature.

This thesis reports a resonance based gravimetric detection system with the purpose of enabling real time cell detection in liquid media.

In this chapter different detection techniques are investigated and background information for purposed design is given. In section 1.1 micro scale detection techniques are categorized and each category briefly introduced with the state-of-art examples from the literature. Section 1.2 focuses on the gravimetric detection. Studies from literature are given to further understanding of reasons behind proposed thesis work.

1.1 Micro Scale Detection Techniques

Detection techniques of biological entities in micro scale can be categorized according to detected parameters. Three most widely sensed parameters can be listed as; optical, electrical, and mechanical [11].

Optical BioMEMS devices are based on the change of the optical properties of target with the interaction of the biocatalyst. Reflectance, fluorescence, chemiluminescence, UV-Vis absorption are taken into account as the mostly used optical properties for the identification of the sample. Sensitivity, flexibility and resistance to electrical noise are the advantages of the optical detection whereas expensive and bulky optical setup is the main disadvantage[2], [5].

Electrical or electrochemical detection methods are commonly used in many of the BioMEMS sensors. Easy miniaturization makes electrical or electrochemical detection devices more favorable than bulky optical detection setups. Electrical/electrochemical sensors are classified under three categories [12]. The first one is amperometric sensors. They measure the change in the electrical current which is the result of a redox process [13]. The second type of electrochemical sensors is potentiometric. They sense the variations of electric potential which is the consequence of ions created by a redox process [14]. The third and the last type is conductometric sensor. These sensors are based on the measurement of the conductance. Conductance between two ports changes as the ionicity of the medium changes[15]. Coulter counter is one of the good examples of the method [16].

Mechanical detection methods are based on the transduction of the mechanical energy. Transducing mechanical energy to sensible entity has been already used since the early MEMS devices (accelerometers, gyroscopes, etc.). One of the most commonly utilized structures as mechanical transducers is micro-cantilevers. Any displacement of a suspended micro-cantilever can be measured by using electronic or optical interfaces. Generally, there are two mechanical parameters that are sensed in the cantilever employed sensors; stress and mass. In the stress sensing devices, surface stress changes with a selective biochemical reaction. This change results in a measurable bending of the cantilever [17]. On the other hand, mass detection sensors track the change in the resonance frequency of the cantilever. Mass change due to the sample capturing creates a shift in the resonance frequency of cantilever. The amount of added mass can be found simply by measuring the frequency shift. In the following section resonant based mass detection sensors are explained in detail.

1.2 Resonant Based Gravimetric Detection

Principle of the resonant based gravimetric detection is the mass and resonance frequency relation. As illustrated in Figure 1-3 resonance frequency of a cantilever is related to mass with an inversely quadratic equation. Any change in the mass can be extracted from the resonance frequencies of loaded and unloaded resonators.

Mass Change Detection
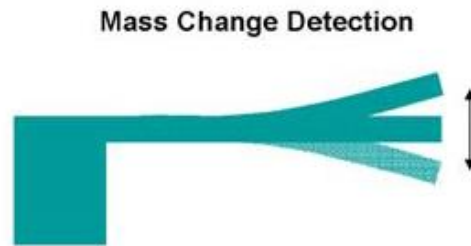
$$f = \frac{1}{2\pi}\sqrt{\frac{k}{m}}$$

$$\Delta m = \frac{k}{4\pi^2}\left(\frac{1}{f_1^2} - \frac{1}{f_o^2}\right)$$

- k = spring constant
- m = mass of cantilever
- f_o = unloaded resonant frequency
- f_1 = loaded resonant frequency

Figure 1-3 Relation of resonance frequency change with system mass change [1].

In the most of the studies in the literature, cantilevers are used as the resonating structure of the gravimetric sensors. An application of silicon resonant cantilever employed mass sensor was proposed by Wasisto *et al.*, [18]. Aim of the sensor is to detect airborne engineered nano-particles that have potential risks on human respiratory system. A piezoelectric actuator and a piezoresistive strain gauge were designed in order to actuate and detect the oscillation of the cantilever sensor, respectively. Quality factor of 1206 and mass sensitivity of 10 Hz/ng was reported. Figure 1-4 shows the images of the sensor and its mass sensing performance.
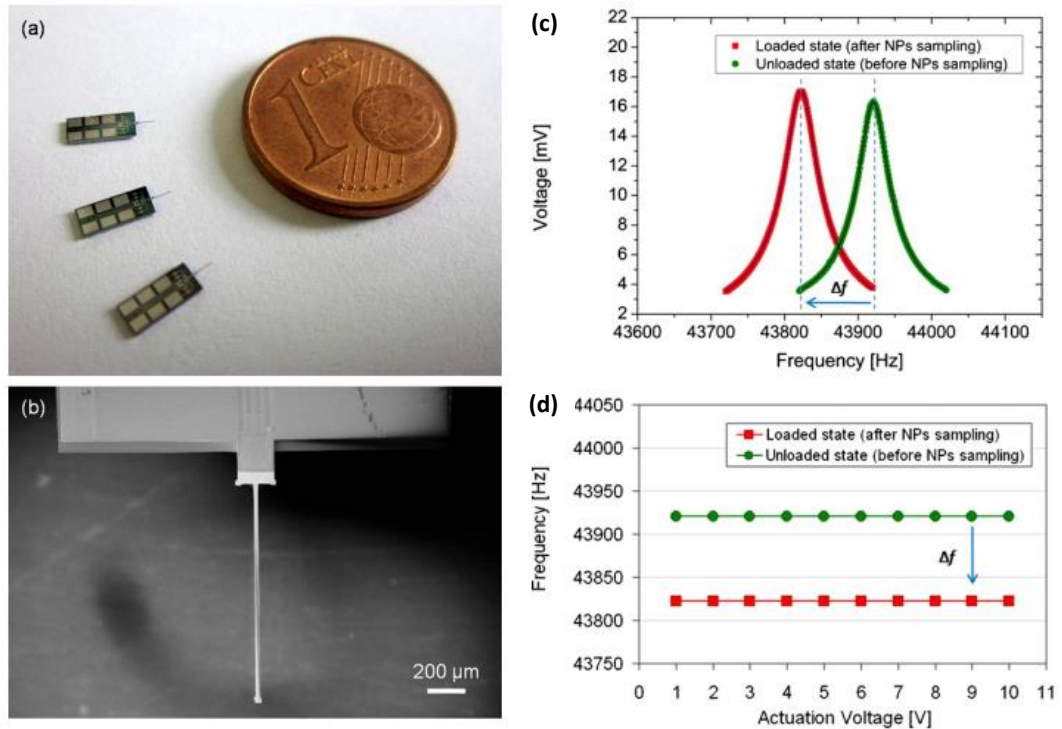
Figure 1-4 Optical (a) and scanning electron micro photographs (b) of the proposed sensor is presented. Frequency shift at an actuation voltage of 9 V (c) and at different actuation voltages (d) is also shown [18].

Although mass sensing performance of the reported sensor in air may be considered as sufficient for the airborne engineered nanoparticle detecting, employing it in a microchannel filled with cell medium would destroy the sensor functionality due to high viscous damping. Note that vaporizing the cell medium is not a solution for the sake of cell integrity.

A breakthrough in resonance-based mass detection in liquid medium has been made by Burg *et al*., [19]. The authors suggested placing the solution inside a hollow, vacuum surrounded resonator structure to eliminate the viscous damping. Figure 1-5 illustrates the resonator structure and sensing mechanism. When there is cell inside the channel resonance frequency of the cantilever decreases. Olcum et al. reported mass sensing resolution of 0.85 attograms in 1-kHz bandwidth by using the same resonator structure [20]. In this work optical actuation and sensing, which increases the application cost, was used. Although, the approach in this study is one of the most novel and successful ideas in the literature, sensing is limited with small sized

particles. For a wider range of targets, including medium sized cells, the microchannel inside the cantilever would be blocked. Increasing the dimensions of the cantilever is not a reasonable solution since it decreases the quality factor and mass sensing resolution.
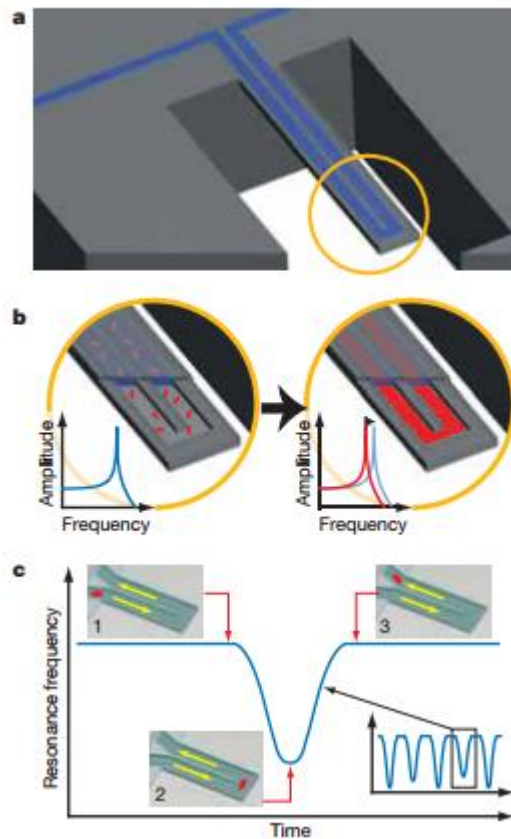
Figure 1-5 Illustration of mass measurement by a fluid-filled microcantilever

Another cantilever based mass sensing study was presented by Park *et al*., [21]. Purpose of the proposed sensor is to make the single-cell mass measurement possible. Dielectrophoresis was used to capture the injected HeLa cells in a microfluidic channel. Captured cell mass was calculated from the resonance frequency shift and results were found close to the reported values in the literature. They also cultured the captured cells and monitored the cell growth. Figure 1-6 shows the schematic of the cantilever array and the measurement setup.
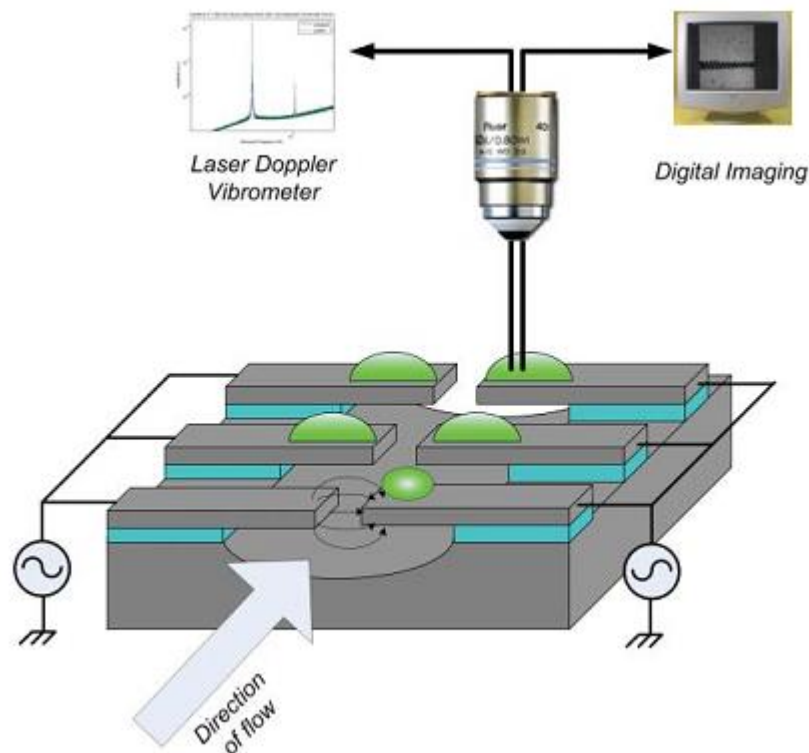
Figure 1-6 Schematic diagram of living cantilever array. As the captured cells are cultured on the array, their mass changes are measured using the resonance frequency shift [21].

Proposed sensor in this study not only measures the single-cell mass but also enables monitoring of the cell growth and analyzes its lifetime. However, requirement of additional equipment makes it unsuitable for widespread usage in the analysis laboratories.

Bayraktar *et al*. reported design, fabrication and test results of MEMS based gravimetric resonator with lateral motion capability to eliminate the drawbacks of the traditional cantilever-based detectors [22]. This structure decreases the squeeze film damping and it is experimentally verified that the system is capable of achieving 5.91 fg/Hz mass sensitivity by measuring the mass of a single 3 μm diameter polystyrene bead. One of the key features of the design is parylene coating. Hydrophobicity of parylene prevents liquid flow through gaps of the sensor and enables the in-liquid measurements by reducing the slide film damping significantly [23]. Figure 1-7 shows the design and test results.
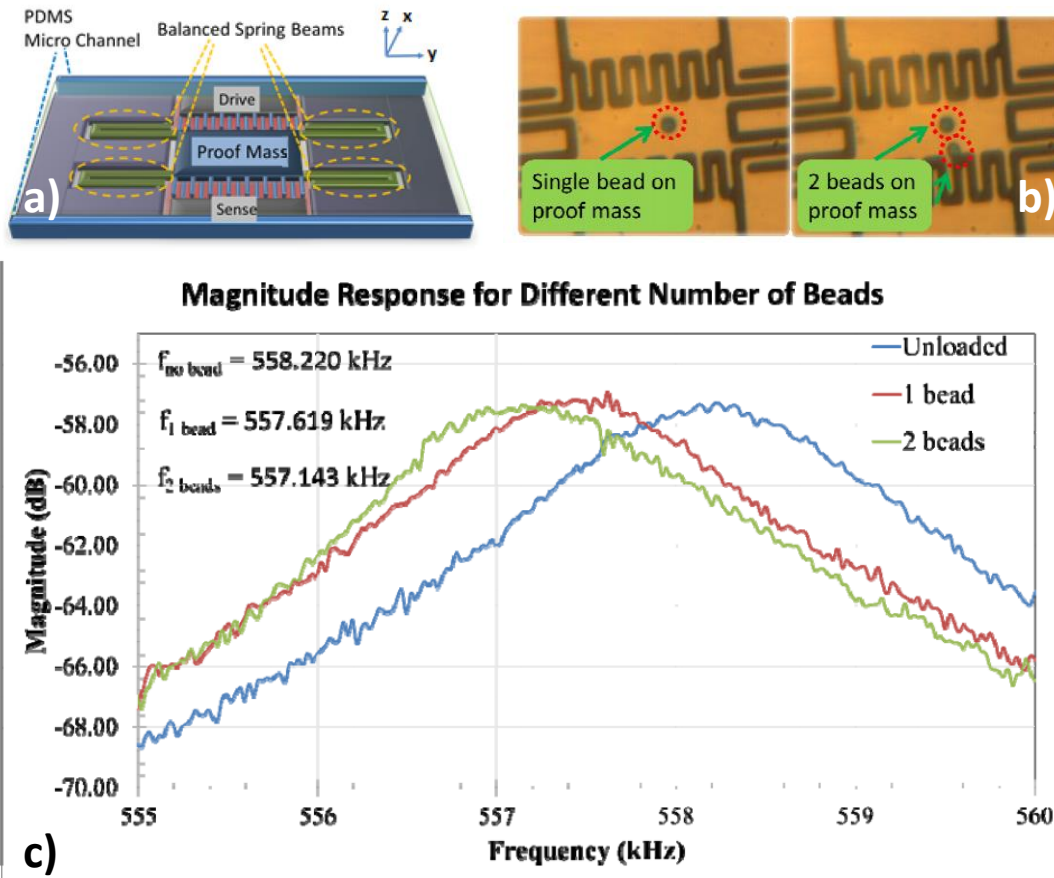
Figure 1-7 Design illustration (a), microscope image of under test device (b) and test results (c) were presented [16].

As a progress for this study, Eroglu *et al.* reported uniform mass sensitivity and high linearity with the same sensor. It is stated that standard deviation in resonance frequency shift is 1.9% for different capture sites [24]. It should be noted that, in the case of a cantilever based mass sensor capture site is decisive in the amount of the frequency shift since it also changes the damping of the resonator.
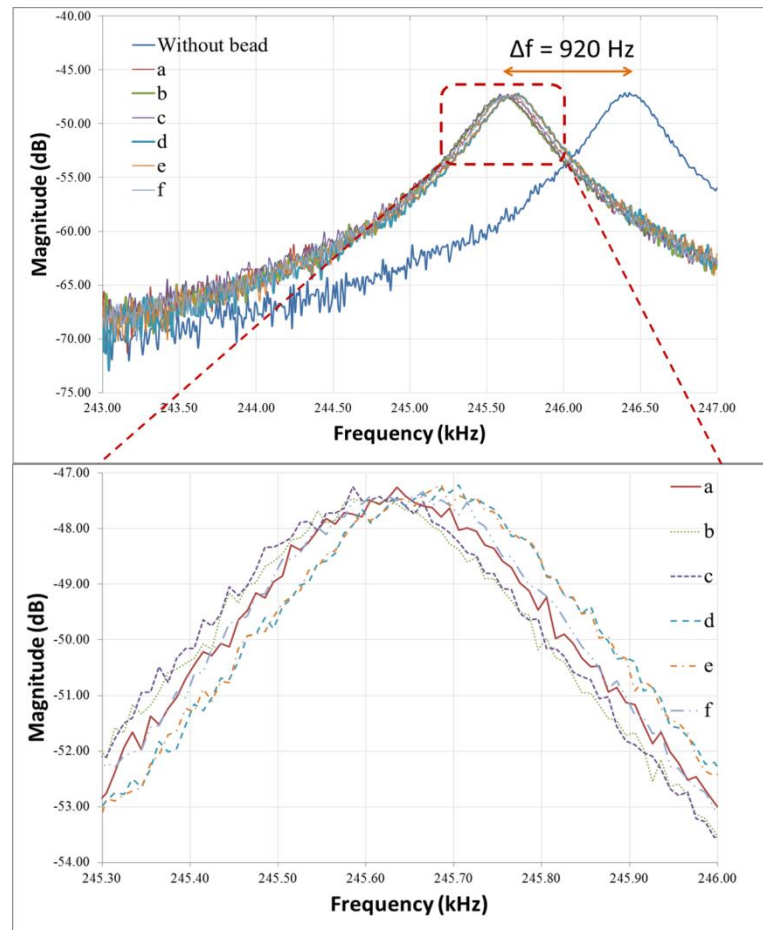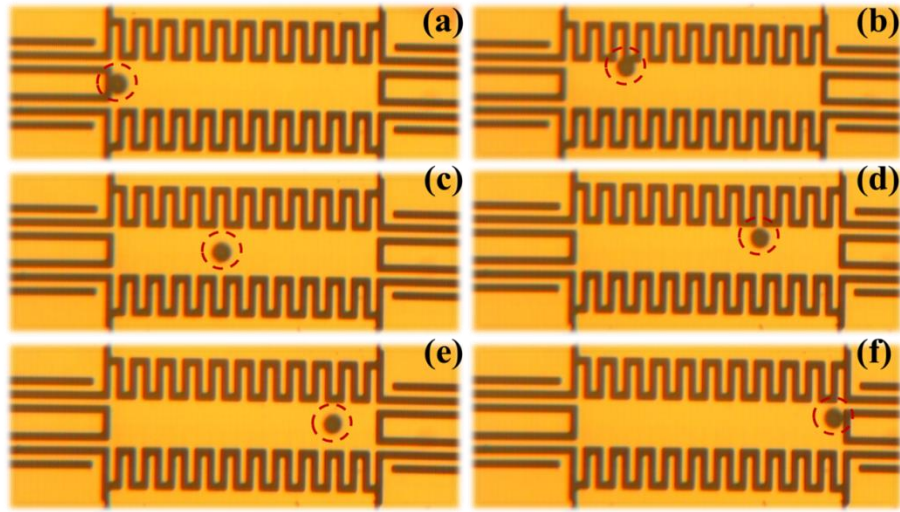
Figure 1-8 Frequency response for unloaded resonator and different bead locations [24]

Ability of capacitive mass sensing in liquid filled microchannel distinguishes this work from others. Proposed sensor in [17] is accepted as benchmark design in this thesis due to its unique characteristics. Even though the advanced properties, it has

design issues that prevents the real-time sensing. There is a capacitive crosstalk between input and output, and the amount of crosstalk electrical current increases when the microchannel is filled. Since the gain of the proposed sensor is low due to inefficient capacitive actuation and sensing, crosstalk current (feedthrough current) prevents the real time sensing as it is an obstacle for the self-oscillation. Reasons and solutions of the problems of this sensor will be discussed after essential background theory will be given.

In this section, high-impact examples of gravimetric detection sensors were introduced. It is seen that although there is a benchmark design that solves some of the traditional problems of gravimetric devices, it still cannot enable real time in-liquid cell detection.

1.3 Research Objectives and Thesis Organization

Objectives of the thesis are to solve the issues related with existing gravimetric sensors in the literature with the capability of real-time mass measurement. To this end,

- increasing the gain by capacitive actuation and sensing optimizations;
- decreasing damping while keeping the gain of the transfer function and mass sensitivity;
- eliminating the effect of feedthrough current that prevents the self-oscillation of the resonator has been selected as the objectives of the thesis.

The thesis is organized as follows:

Chapter 2 gives the essential theoretical background to analyze the operation of micromechanical resonators. Second order mass, spring, damper system is used for mathematical analyses of physical resonator. After that, capacitive actuation and sensing methods are introduced. Next, feedthrough current effect, which is the primary obstacle of real-time detection, is presented and some elimination methods are proposed. After the necessary theoretical background, the design procedure of the devices is presented together with the Comsol finite element analysis results.

Chapter 3 is about the fabrication of the resonators. Previous process flow for fabrication is given and fabrication related problems are analyzed. A new process flow is proposed to solve the mentioned fabrication problems. Fabrication of the proposed sensors was established by following the new flow.

Various measurements are presented in chapter 4. First, the experimental setup including test electronics is briefly given. Then, resonance characterizations of each design are presented. After, mass detection test procedure and result is introduced. Finally, resonance characterization of a wet sensor is shown.

Finally, chapter 5 concludes the thesis. Accomplished research objectives and possible future work suggestions are given.

CHAPTER 2

THEORY & DESIGN

In this chapter, the theoretical background of the resonant based capacitive gravimetric sensor and the mathematical analysis of the device design procedure are presented.

Section 2.1 explains the theory behind the operation of the sensor in two parts; the resonator-by utilizing a second order mass, spring, damper model-and the capacitive actuation and sensing. This section also introduces the reasons and the effects of the feedthrough current. Section 2.2 gives the device structures with the design parameters and the design procedure.

2.1   Working Principles of a Resonant Based Capacitive Gravimetric Sensor

A resonant based sensor can be analyzed under two subtopics. The first one is the mechanical resonator. It simply converts the applied force to displacement. The second subtopic contains the actuation and the sensing mechanisms. The actuation is the part that converts the applied input to the force that is necessary to make the resonator move. On the other hand, the sense part transforms the displacement of the resonator into a detectable parameter.

In a resonant based capacitive gravimetric sensor (RCGS), applied electrical potential is the input that is converted to the force (actuation), this force creates a displacement on a suspended mass (resonator), and finally the displacement is converted to the electrical current (sensing) that can be sensed by proper electronics.

Theory of the resonator is given in section 2.1.1. Displacement of a resonator under applied force is investigated. The capacitive actuation and the sensing mechanisms are analyzed in section 2.1.2 to get the ideal transfer function of a resonant based

capacitive gravimetric sensor. To complete the theoretical aspect of the resonant based capacitive sensor, feedthrough current should also be investigated. In a capacitive actuation and sensing there is an inevitable stray current directly between the actuation and the sense parts which is named as feedthrough current. Section 2.1.3 explains the effect of the feedthrough current in detail.

2.1.1 Resonator Theory

Second order mass, spring, damper system can be used for modelling a resonator. Such a system can be represented as the schematic in Figure 2.1 where k denotes the spring constant, B indicates the damping constant, m represents the resonating mass, and F stands for the applied force.
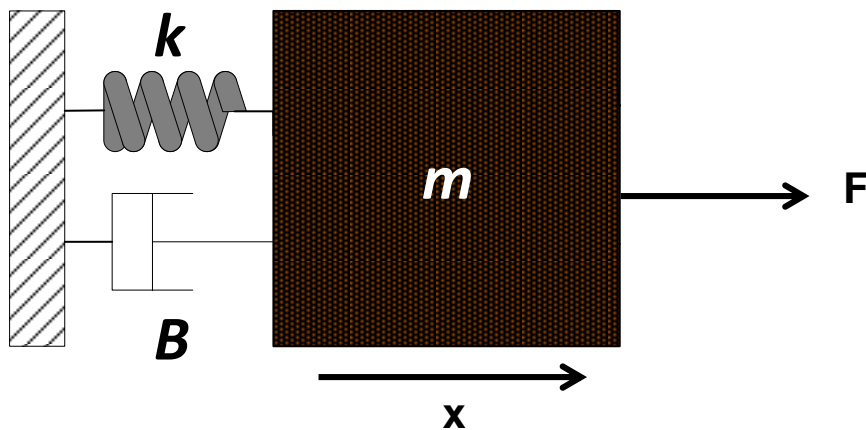
Figure 2-1 Schematic view of the second order mass, spring, damper system.

Equation (2.1) relates the displacement of a resonating mass, x, and the applied force, F.

$$m\ddot{x} + B\dot{x} + kx = F \qquad (2.1)$$

In order to make the frequency analyzes of the transfer function of force to displacement, the Laplace transform of the transfer function should be analyzed. Equation (2.2) shows the Laplace transform of the transfer function which is given in Equation (2.1).

$$\frac{X(s)}{F(s)} = \frac{1}{ms^2 + Bs + k} \qquad (2.2)$$

Natural frequency of a spring mass system is defined as:

$$\omega_n = \sqrt{\frac{k}{m}} \qquad (2.3)$$

However, natural frequency is not the frequency that system gain has its maximum value in a damped system. The frequency of oscillation, the frequency that the gain is the maximum, can be expressed as in Equation (2.4):

$$\omega_d = \omega_n \sqrt{1 - {\xi_d}^2} \qquad (2.4)$$

where ξ_d represents the damping ratio and it can be defined as:

$$\xi_d = \frac{B}{2\sqrt{mk}}. \qquad (2.5)$$

Damping ratio is an important parameter especially for the self-oscillation. If the damping ratio is greater than 1, then oscillation frequency becomes an imaginary number which means oscillation at any frequency cannot be achieved. Such a system can be named as an overdamped system. On the other hand, if the damping ratio is less than 1, the system becomes underdamped. Oscillation frequency of an underdamped system becomes closer to the natural frequency of the system as the damping ratio decreases further.

In order to measure how much underdamped the system is, there is a parameter namely quality factor (Q). Quality factor can be defined as:

$$Q = \frac{1}{2\xi_d \sqrt{1 - {\xi_d}^2}}. \qquad (2.6)$$

In this work, lateral resonators are studied and damping ratio of a lateral resonator is usually smaller than even 0.05 in air. Therefore, Equation (2.6) can be expressed as follows:

$$Q \cong \frac{1}{2\xi_d} = \frac{\sqrt{km}}{B}. \qquad (2.7)$$

2.1.2 Electrostatic Capacitive Actuation and Sensing

Mechanical resonator systems in MEMS application can have several types of actuation and sensing mechanisms such as thermal[25], [26], optic[27], [28], electrostatic[29] etc. In our case, actuation is handled by electrostatic force and the displacement of the resonator is sensed by detecting the injected output electrical current.

The source of electrostatic force on the capacitive plates is the change in the stored electrostatic energy. Basically, gradient of this energy gives the electrostatic force on the plates. In order to extract the actuation force, capacitance and stored energy should be formulized.

The schematic view of a parallel plate capacitor is seen in Figure 2-2 and the total capacitance of a parallel plate structure is given in Equation (2.7) where ε_r is the medium relative permittivity, ε_0 is the vacuum permittivity, $L_{overlap}$ is the capacitive overlap length, h is the plate height and d_{gap} is the distance between the capacitive plates.
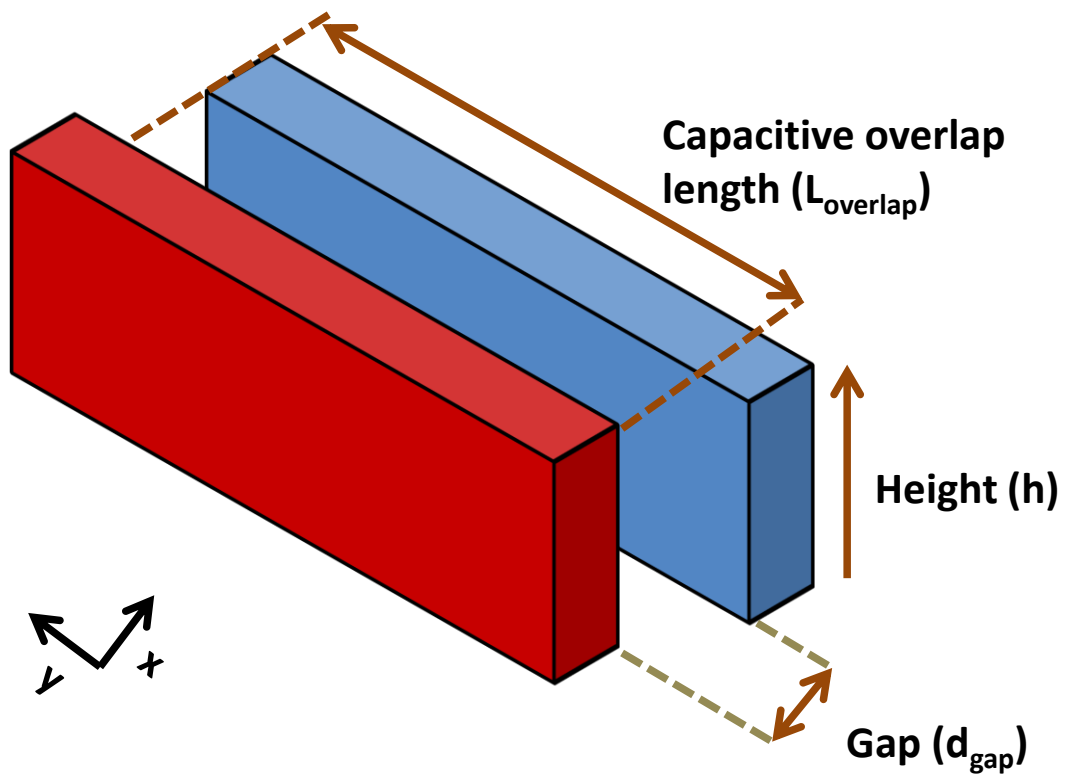
Figure 2-2 Schematic view of a parallel plate capacitor with associated variables.

$$C = \varepsilon_r \varepsilon_0 \frac{L_{overlap} * h}{d_{gap}} \tag{2.7}$$

Stored electrostatic energy on the capacitive plates is an outcome of the applied electrical potential. The expression for the electrostatic energy is presented in Equation (2.8).

$$E = \frac{1}{2} CV^2 \tag{2.8}$$

As it is already stated, force can be extracted by taking the gradient of the electrostatic energy:

$$\mathbf{F} = \nabla E.$$

(2.9)

Let's say that the capacitor plates can only move in the x-axis (the resonators designed in this thesis have one dominant axes of motion) the electrostatic force expression reduces to:

$$\mathbf{F} = \frac{\partial E}{\partial x} = \frac{1}{2}\frac{\partial C}{\partial x}V^2.$$

(2.10)

Now assume that a voltage that consists of both DC and AC components, as in the Equation (2.11), is applied to one of the capacitor plates.

$$V = V_{DC} + V_{ac}\sin(\omega t)$$

(2.11)

Then, the expression of the electrostatic force becomes as in Equation (2.12).

$$F = \frac{1}{2}\frac{\partial C}{\partial x}\left[\left(V_{DC}^2 + \frac{V_{ac}^2}{2}\right) + 2V_{DC}V_{ac}\sin(\omega t) - V_{ac}^2\cos(2\omega t)\right]$$

(2.12)

Consider one of the capacitive plates as a surface of movable resonator and the other one as fixed. Equation (2.12) and Equation (2.1) show that applying only a DC potential alone would result in movable plate displacement until the spring force and the electrostatic force become equal. On the other hand, applying an AC potential introduces two varying force components with angular frequencies of *w* and *2w*. The force component with the angular frequency of *2w* is an unintended side effect and in order to eliminate the effect of this force, choosing a DC potential which is very larger than the AC potential is sufficient. Assuming that DC voltage is far greater than the AC voltage, Equation (2.12) can be simplified as:

$$F = \frac{1}{2}\frac{\partial C}{\partial x}\left[V_{DC}^2 + 2V_{DC}V_{ac}\sin(\omega t)\right]. \tag{2.13}$$

Proposed resonator has symmetric and stationary sense and drive ports on the displacement axis. DC voltage is applied to the suspended resonating part and AC voltage is applied to the stationary actuation part. Therefore, the net force on the movable part does not have V_{DC}^2 part due to symmetry. The net force on the suspended part and its Laplace transform can be seen in Equation (2.14) & (2.15)

$$F_x(t) = \frac{\partial C}{\partial x}V_{DC}V_{ac}\sin(\omega t) \tag{2.14}$$

$$F_x(s) = \frac{\partial C}{\partial x}V_{DC}V(s) \tag{2.15}$$

While the electrostatic actuation is caused by a change in the stored energy on the capacitive plates, the sensing mechanism is based on a change in the stored charge. Change in the capacitance of the plates crates a change in the stored charge of the capacitor. As a result of stored charge variance, a current injection through the capacitor occurs. Therefore the injected current can be formulated as the rate of change of the stored charge as in Equation (2.16).

$$i(t) = \frac{\partial Q}{\partial t} = \frac{\partial C}{\partial t}V + C(t)\frac{\partial V}{\partial t} \tag{2.16}$$

As previously rationalized $V_{DC} \gg V_{ac}$, so the second term in Equation (2.17) can be neglected and the equation reduces to:

$$i(t) \cong \frac{\partial C}{\partial t}V_{DC} = \left(\frac{\partial C}{\partial x}\frac{\partial x}{\partial t}\right)V_{DC}. \tag{2.17}$$

Laplace transform of the system is also necessary for analyzing the frequency response of the system:

$$I(s) = \frac{\partial C}{\partial x} s X(s) V_{DC}.$$

(2.18)

To conclude, applying a voltage that has AC and DC parts creates an electrostatic force and as a result of this electrostatic force, displacement of the movable part takes place. Displacement of the capacitive plate is the reason of the capacitance change and the current injection through the sense part. Therefore, the input of the system is the applied voltage and the output is the sense current. The overall transfer function of the system which relates the injected output current to the applied input voltage can be extracted by multiplying three transfer functions (V to F, F to x, x to I). Equation (2.19) shows the overall transfer function. A possible frequency response of Equation (2.19) is given in Figure 2-3.

$$H_{total}(s) = \frac{I(s)}{V(s)} = \frac{X(s)}{F(s)} \frac{F(s)}{V(s)} \frac{I(s)}{X(s)} = \frac{s\left(\frac{\partial C}{\partial x} V_{DC}\right)^2}{ms^2 + bs + k}$$

(2.19)
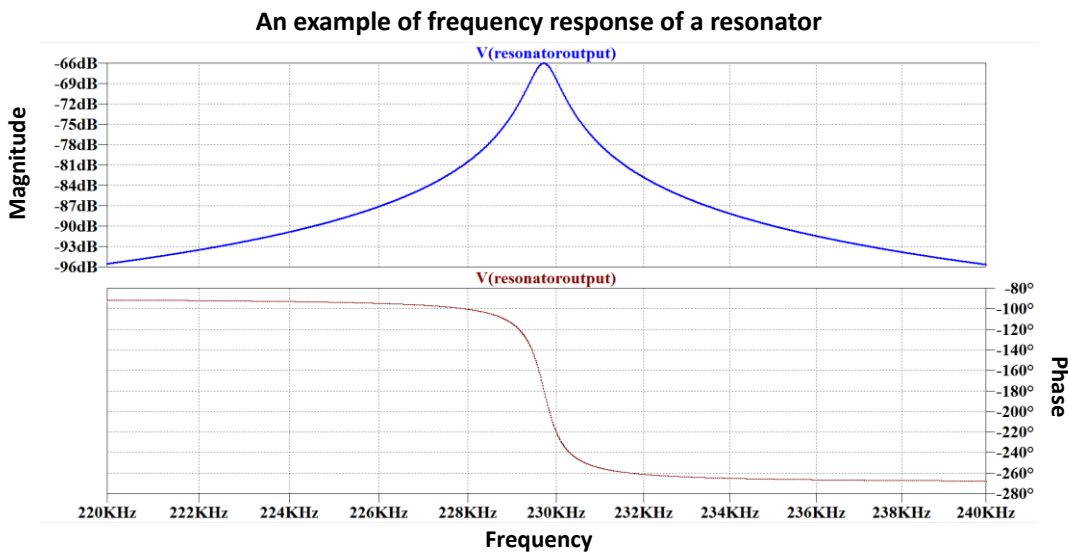
Figure 2-3 A possible frequency response of Equation (2.19)

Figure 2.3 shows that the resonator system behaves as a band-pass filter. Maximum gain is achieved at resonance frequency and the phase response changes from 90° to -90° and it is 0° at resonance frequency.

It can be seen from Equation (2.19) that the magnitude of the transfer function is proportional with the applied DC voltage, V_{DC}, and the capacitance change with an infinitesimal displacement on the movement direction, $\frac{\partial c}{\partial x}$. As it is already explained, capacitance is proportional with the ratio of the capacitive area and gap. Displacement of a capacitive plate may change the capacitive overlap area and/or the gap between capacitive surfaces. Therefore capacitive resonators can be investigated under two categories according to the method of the capacitance change; varying overlap area and varying gap.

2.1.2.1 Varying overlap area capacitance

In the varying overlap area capacitive actuation, the structure is allowed to move in such a direction that only the capacitive overlap area of the plates changes with the displacement. An example of such movement is illustrated in Figure 2-4.
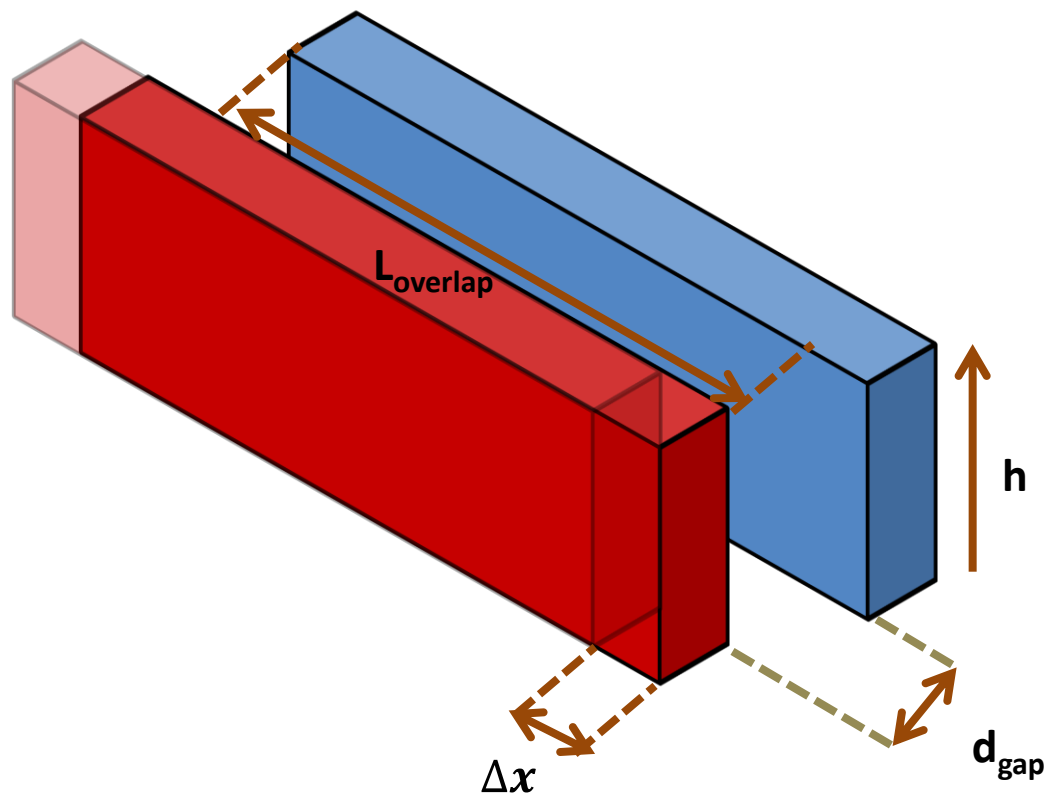
Figure 2-4 Illustration of varying overlap capacitance

Illustrated displacement of Δx in Figure 2-4 changes the capacitance between the plates by changing $L_{overlap}$. The change in the capacitor with an infinitesimal displacement of Δx is calculated in Equation (2.20).

$$\frac{\partial C}{\partial x} = \frac{\partial \left(\varepsilon \frac{(L_{overlap} + \Delta x) * h}{d_{gap}} \right)}{\partial x} = \varepsilon \frac{h}{d_{gap}} \qquad (2.20)$$

Equation (2.20) emphasizes that the length of the capacitor plates has no role in the capacitive change with displacement. The other result that can be extracted is the linearity of the capacitance change. Simply, amount of the capacitance change is not a function of the displacement.

2.1.2.2 Varying gap capacitance

Capacitive structures that are allowed to move in such a direction that only the distance between capacitive plates changes as it moves are named as varying gap capacitance. Figure 2-5 displays an example of such a displacement.
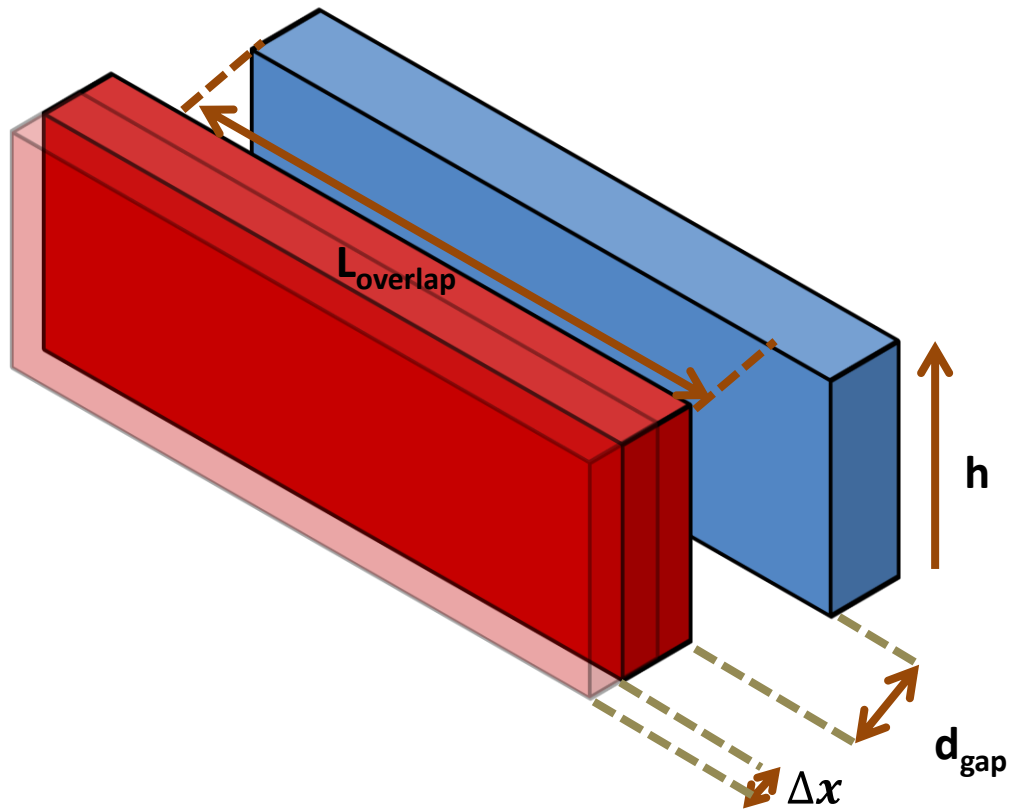
Figure 2-5 Illustration of varying gap capacitance

Equation (2.21) shows that the capacitance change is a function of both overlap length, $L_{overlap}$, and displacement, x. Although it seems that amount of displacement effects the capacitive change, this affect is negligible if x is too small when compared to the gap between the plates, d_{gap}.

$$\frac{\partial C}{\partial x} = \frac{\partial \left(\varepsilon \frac{L_{overlap} * h}{d_{gap} - x} \right)}{\partial x} = \varepsilon \frac{L_{overlap} * h}{\left(d_{gap} - x \right)^2} \qquad (2.21)$$

2.1.3 The feedthrough current and elimination methods

Feedthrough current can be defined as a capacitive leakage current from the actuation pad to the sense pad directly on undesired capacitance between those pads.

Magnitude of the feedthrough current continuously increases with frequency since the impedance of capacitance decreases with frequency. Therefore, magnitude of the output current becomes greater at higher frequencies than the resonance frequency. However, it is desired that the output current should be at its maximum value at the resonance frequency.

In order to analyze the effect of feedthrough current further, feedthrough term should be added to overall transfer function. Equation (2.22) shows the updated transfer function that contains feedthrough current term.

$$H_{total}(s) = \frac{I(s)}{V(s)} = \frac{s\left(\frac{\partial C}{\partial x}V_{DC}\right)^2}{ms^2 + bs + k} + sC_{feedthrough} \qquad (2.22)$$

At the resonance frequency, mechanical resonance based part of the transfer function has only real part. Since the feedthrough current is a capacitive current, it adds only imaginary part to the transfer function. As a result of this situation, magnitude peak and phase change at resonance is suppressed by the feedthrough current. Figure 2-6 illustrates the feedthrough current effect on resonance characteristics.
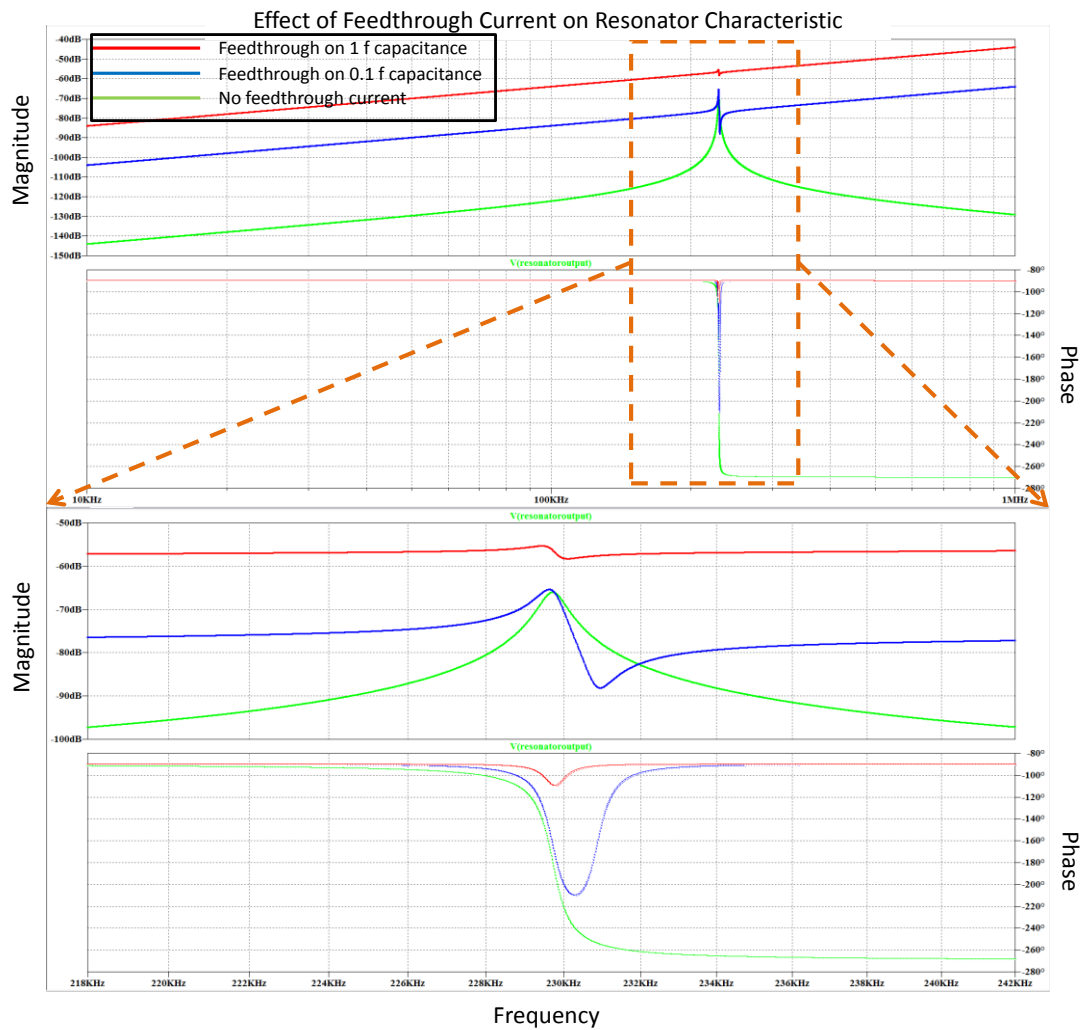
Figure 2-6 Green line denotes the AC response of the resonator only, whereas blue and red lines show the contribution of feedthrough current on 0.1 fF and 1 fF of capacitance, respectively.

Barkhausen stability criterion says that closed loop oscillation at a certain frequency occurs if the phase response of a closed loop system is 0° and magnitude response is at least 1. Feedthrough effect prevents the closed loop oscillation at resonance frequency by introducing higher gain for the higher frequencies and by disrupting the phase response.

In this thesis, two different feedthrough current cancellation techniques are investigated[30].

2.1.3.1 Feedthrough elimination with dummy signal

The first technique is based on creating two out of phase feedthrough current on the same sense port. In the ideal case, two feedthrough current with the same magnitude and 180° phase difference cancels each other. Figure 2-7 illustrates the technique.
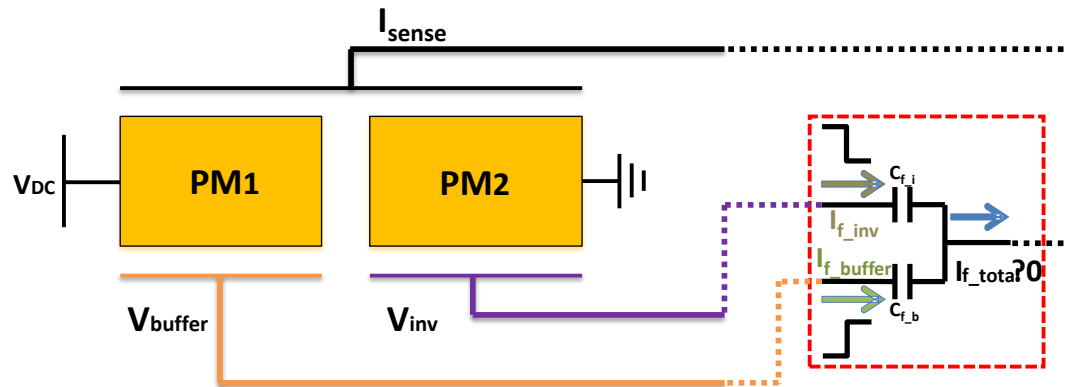
Figure 2-7 Two out of phased feedthrough currents cancel each other on sense port.

A DC voltage (V_{DC}) is applied on the proof mass 1 (PM1) but proof mass 2 (PM2) is grounded. Therefore, PM1 is able to move with an AC potential (V_{buffer}) however PM2 is not. V_{buffer} does not only create a displacement on the PM1 but also a feedthrough current on the sense port. On the other hand, V_{inv} which has the same magnitude but opposite phase with V_{buffer}, creates only the feedthrough current on the sense port. Since these two feedthrough currents are opposite phased, they exterminate each other at the sense port. [31]

There are some disadvantages of this technique. First of all there may be mismatches in feedthrough capacitances between sense port and the two drive ports. In order to compensate this mismatch, amplification is necessary for one of the signals. However, it is not easy to have exactly out of phase signals when one of them is amplified by a factor of ten or hundred (as gain increases, the bandwidth response changes). Assume $V_{buffer}cos(w_0t)$ and $V_{inv}cos(w_0t+\Theta)$ is applied to the two drive ports. Then I_{f_inv} , I_{f_buffer} and I_{f_total} can be expressed as in Equation (2.23)-(2.25) in Laplace domain.

$$I_{f_{buffer}}(s) = V_{buffer} \frac{s}{s^2 + w_0^2} sC_{fb} = K_b \frac{s^2}{s^2 + w_0^2} \qquad (2.23)$$

$$I_{f_{inv}}(s) = V_{inv} \frac{scos(\theta) - w_0 \sin(\theta)}{s^2 + w_0^2} sC_{fi}$$

$$= K_i \frac{s^2 cos(\theta) - sw_0 \sin(\theta)}{s^2 + w_0^2} \qquad (2.24)$$

$$I_{f_{total}}(s) = \left(K_b + K_i cos(\theta)\right) \frac{s^2}{s^2 + w_0^2} - K_i \frac{sw_0 \sin(\theta)}{s^2 + w_0^2} \qquad (2.25)$$

Now I_{f_total} to I_{f_buffer} ratio will emphasize the feedthrough elimination success. As seen in Equation (2.26), in an exact feedthrough cancellation, where K_i is equal to K_b and Θ is 180°, R becomes zero.

$$R = \frac{I_{f_{total}}(s)}{I_{f_{buffer}}(s)} \Big|_{s=jw_0} = \left(1 + \frac{K_i}{K_b} cos(\theta)\right) + j \frac{K_i}{K_b} sin(\theta) \qquad (2.26)$$

Figure 2-8 shows the effect of phase and magnitude mismatches on feedthrough elimination. Y axis shows the ratio of total feedthrough current to the single drive feedthrough current, X axis shows the phase difference between the two drive signals (Θ). There are five lines for five different values of signal magnitude ratios (K_i over K_b).
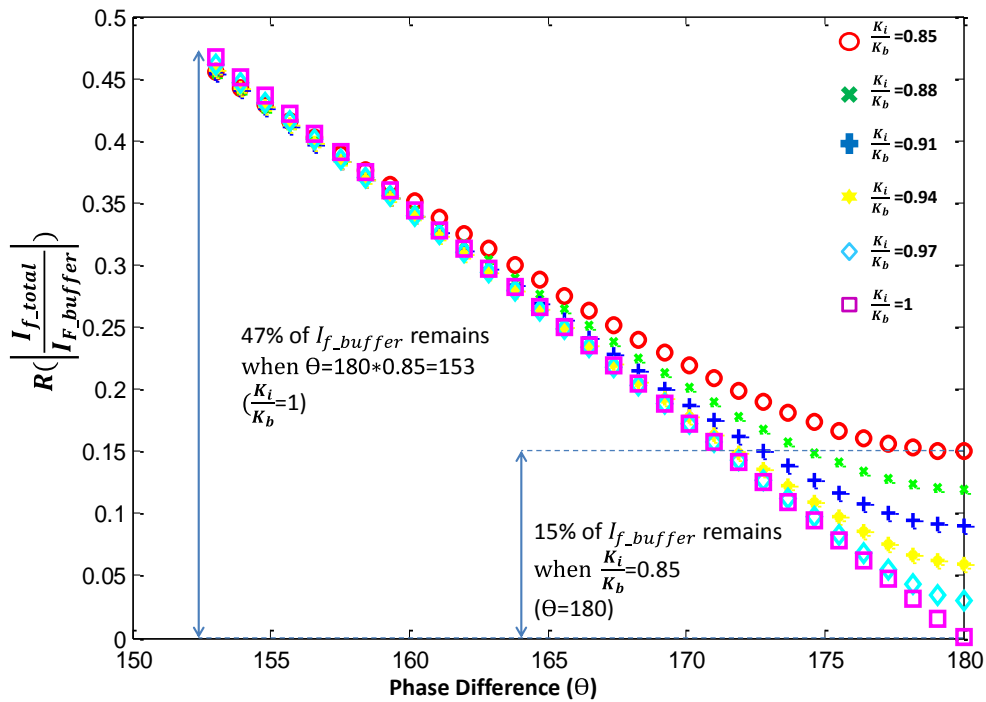
Figure 2-8. Largest effect of the magnitude mismatch is at Θ=180° and amount of remaining current percentage is equal to the deviation percentage. Whereas effect of phase deviation is maximum at fully matched gain case and remaining current percentage is approximately three times of deviation percentage of Θ from 180°

K_i and K_b consists of capacitor and applied voltage multiplication. In the case of mismatching feedthrough capacitors, applied voltage should be adjusted to equalize the K_i and K_b. However, amplifying one of the signals changes the frequency response of the amplifier which means arranging magnitudes may change the Θ. As a result, setting phase and magnitude of the dummy signal for feedthrough elimination can be problematic in case of feedthrough capacitance mismatch.

The second disadvantage is the power consumption. There is a signal which has no role in the actuation of the resonator. Not only the dummy signal but also the electronics necessary to obtain the dummy signal consumes power that has no contribution to the actuation of the mass sensing resonator.

30

2.1.3.2 Feedthrough elimination with differential sense ports

In the second feedthrough current elimination method, there are two different sense ports. These two ports should have $\frac{\partial C}{\partial x}$ terms of opposite signs and feedthrough currents have same sign at the same displacement. So that by taking difference of these outputs, the two feedthrough currents cancel each other and the resonator outputs are added. The structure in Figure 2-8 is an illustration of the methodology. Two output currents converted into voltage and their difference is taken by the voltage subtractor.
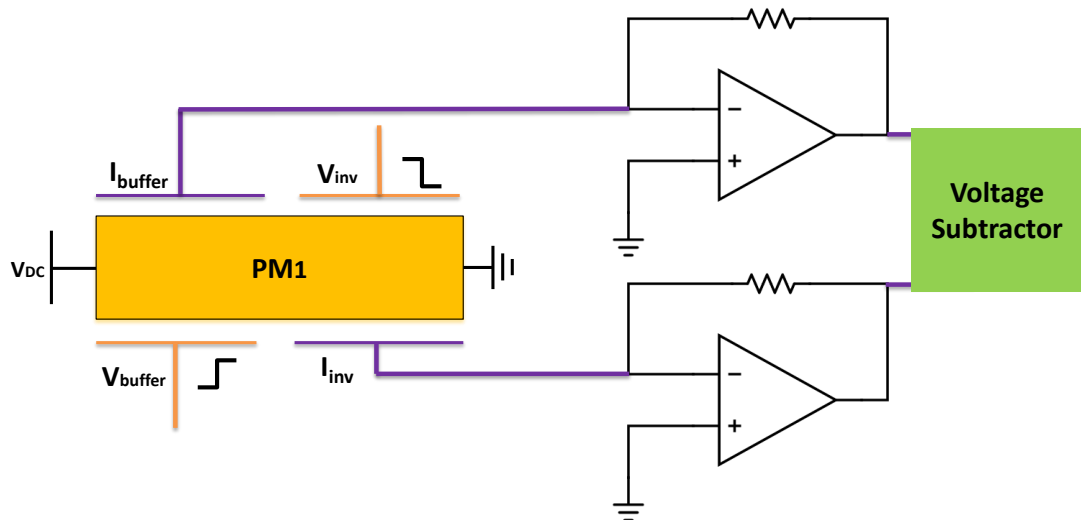
Figure 2-9 Taking difference of the two output currents cancels the same phased feedthrough current out and adds up oppositely phased resonator related currents.

In the perfect symmetry case, feedthrough capacitances between each drive and the two sense ports are the same. On the other hand, the proof mass (PM) displacement creates opposite signed electrical currents in the two sense ports, since capacitive changes of the two sense ports are opposite signed at the same displacement. Therefore, the difference of these two signals does not include feedthrough term but has contribution of proof mass displacement related signals from both sense capacitors.

31

In case of the mismatch in feedthrough capacitances, not the resistance in transimpedance amplifier but in the voltage subtractor is arranged to adjust the coefficients in the subtraction. Moreover, unlike the previous method, both signals are used to actuate the resonator.

2.2 Device Structures and Design Strategies

The resonance frequency of a resonator has an inverse quadratic relation with the resonating mass. Therefore, added mass can be found by using natural frequencies of before and after mass addition in Equation (2.27).

$$\Delta m = k(\frac{1}{w_1^2} - \frac{1}{w_2^2}) \qquad (2.27)$$

Variety of resonators with comb finger were designed, fabricated and tested previously for the purpose of the mass sensing [22], [32], [33]. One of the biggest design achievements was handled by parylene coating. In order to make the resonator functional in liquid environment, resonators were parylene coated. Since parylene is a hydrophobic material, it prevents the liquid flow through to gaps up to 4-5 μm [23].

The most important design trade-off is the necessity of wide surface area to collect target cells and the request of smaller resonating mass to increase the mass detectability. These two criteria forces to increase the cell capture surface area to capacitive surface area ratio. To minimize the resonating mass, active layer of SOI was also selected as small as possible (5μm is selected since it is the lowest limit for uniform fabrication). Outcome of these concerns is small output current and the measurements of the previously designed sensors also showed that the gain of the transfer function is too small that it can be suppressed by the feedthrough current. In order to discuss the detailed reasons of this situation, previously designed resonant based capacitive gravimetric sensor (RCGS#1) will be investigated in section 2.2.1.

In order to increase the mass sensing performance of the system, four new resonant based capacitive gravimetric sensor designs are proposed. The purpose of the RCGS#2 and RCGS#3 is to increase gain of the resonator without increasing the total mass of the sensor. Moreover, RCGS#4 and RCGS#5 have the ability of differential sensing which is designed to eliminate the feedthrough current. For the sake of design comparison, each design utilizes the same anchor structure (to have same spring constant) and the first three have the same cell capture area dimensions with the previously proposed design.

Finite element modeling simulations of each design is also presented. Resonance frequencies, resonant modes of the sensors including the fundamental one and displacement amounts are extracted from simulations. Comsol Multiphysics is employed as simulation tool. Eigenvalue solver of electromechanics physics interface is used. 100 V and 0 V are selected as boundary conditions for proof mass and electrodes, respectively, to include stationary electrostatic forces. Ten times exaggerated displacement at fundamental frequencies are given for each design.

2.2.1   RCGS#1

The first design is one of the previously designed resonators that have comb finger structure [33]. Before suggesting new device structures, it is important to analyze the previous one to understand the design drawbacks. In this design, comb finger structures were presented as capacitive plates. Figure 2-10 shows the illustration of the sensor. Fundamental vibration mode is presented in Figure 2-11.
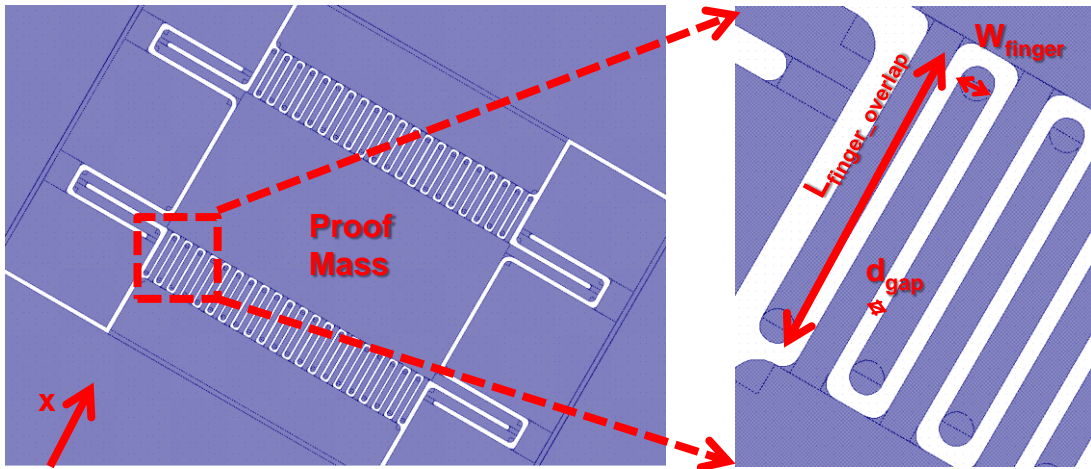
Figure 2-10 Layout of RCGS#1
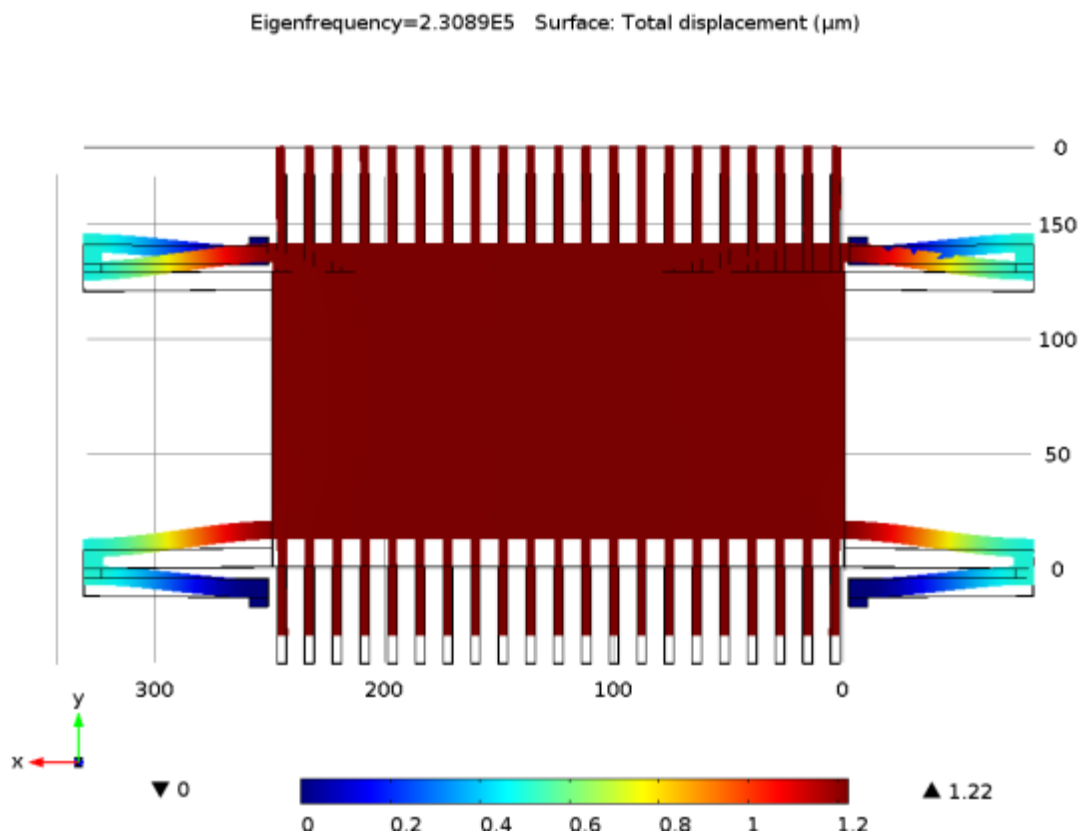
Figure 2-11 Fundamental vibration mode of RCGS#1 is at 230 kHz

Direction of displacement is along the finger direction. Therefore, overlap area of the capacitive plates changes with the displacement. Although the purpose of the fingers is to create varying overlap area capacitance, there is also a varying gap

34

capacitance at fingers ends. While there is a motion, distance between the end of a finger and the surface across the finger changes. Since the width of the finger is comparable with the gap between finger ends and across, varying gap capacitive change is comparable with the varying overlap part. Change of capacitance with displacement for the varying overlap and varying gap capacitors are calculated to figure out the contributions of the different capacitive interfaces. Related calculations can be seen in Equation (2.28) & (2.29). There are 20 fingers in each side and the length of the finger overlap, $L_{finger\_overlap}$, is 42 µm, the gap between capacitive plates, d_{gap}, is 2 µm, the height of the structure, h, is 5 µm, the length of the proof mass is equal to 248 µm and the width of the proof mass is 128 µm.

$$\frac{\partial C}{\partial x} = \frac{\partial \left(\varepsilon \dfrac{(L_{finger\_overlap} + x) * h}{d_{gap}} + \varepsilon \dfrac{(w_{finger}) * h}{d_{gap} - x} \right)}{\partial x} \tag{2.28}$$

$$\frac{\partial C}{\partial x} = \varepsilon \frac{h}{d_{gap}} + \varepsilon \frac{(w_{finger}) * h}{\left(d_{gap} - x \right)^2} \tag{2.29}$$

The red terms in the equation denote the contribution of varying overlap capacitance and the black terms refer to varying gap related part.

Overall transfer function includes two $\frac{\partial C}{\partial x}$ terms one for sense and the other for actuation. Note that these two terms differ because of the sign of the displacement, x.

$$\left(\frac{\partial C}{\partial x}\right)_{sense} \left(\frac{\partial C}{\partial x}\right)_{act.}$$

$$= \varepsilon^2 \left(\frac{h}{d_{gap}} + \frac{(w_{finger}) * h}{\left(d_{gap} - x\right)^2} \right) \left(\frac{h}{d_{gap}} \right.$$

$$\left. + \frac{(w_{finger}) * h}{\left(d_{gap} + x\right)^2} \right) \qquad (2.30)$$

Equation (2.30) is calculated with MATLAB for different displacement values and multiplication of displacement derivatives of capacitive changes at sense and actuation ports versus displacement is drawn in the Figure 2-12 with the red line. Moreover, the same multiplication is also calculated and drawn with the assumptions of there is only varying gap capacitance and only varying overlap capacitance separately, to see the weight of their contributions. The dashed black line represents the part that contains only varying gap term and the solid black line represents the part that contains only varying overlap term.

Figure 2-12 $\left(\frac{\partial C}{\partial x}\right)_{sense} \left(\frac{\partial C}{\partial x}\right)_{act.}$ vs displacement for RCGS#1 is drawn where the red line shows the total result, the dashed black line is the contribution of only varying gap related term and the solid black line is the contribution of only varying overlap related term.

Calculation results show that varying gap is far more effective while comparing varying overlap due to the small gap at the ends of the fingers. To decrease the varying gap effect, the gap between the finger end and the opposite plate should be increased. Figure 2.13 shows the overall total capacitive sensitivity versus displacement for different gaps at fingers ends.
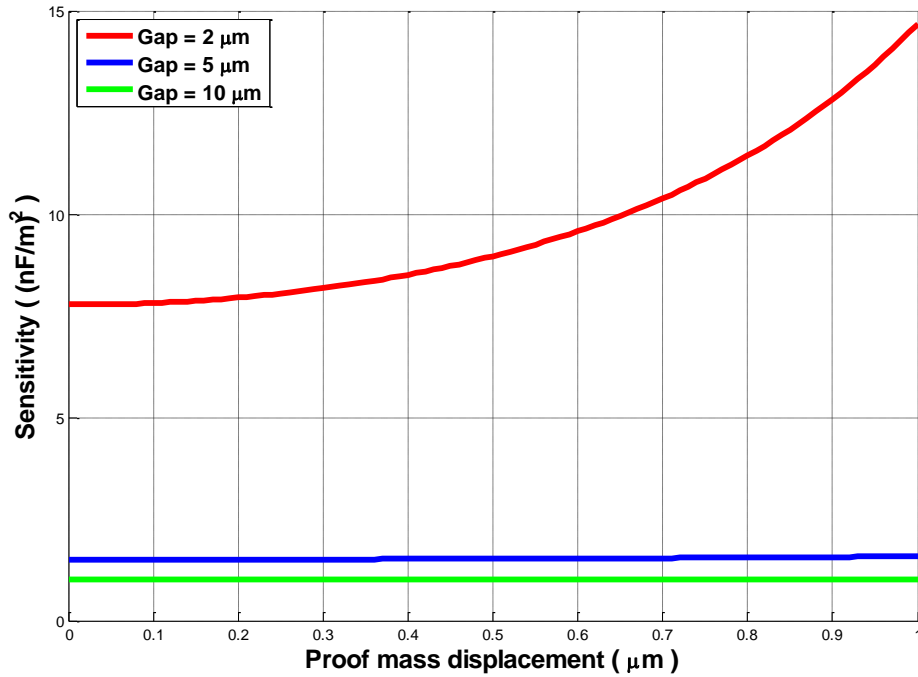
Figure 2-13 $\left(\frac{\partial C}{\partial x}\right)_{sense} \left(\frac{\partial C}{\partial x}\right)_{act.}$ vs displacement of RCGS#1 for different gaps at finger ends

In order to make the sensor behave as varying overlap capacitance, gap after finger end should be wider than 5μm. However, parylene hydrophobicity cannot prevent liquid flow through the gaps wider than 5μm. There is also a significant drop at the sensitivity for larger widths.

To conclude, it is seen that contribution of the comb finger to the sensitivity is limited in this design. Therefore, fingers removal to have fully varying gap capacitive interface is chosen as the first design idea.

2.2.2 RCGS#2

Calculations in the previous part showed that impact of fingers to the sensitivity is not very strong. Apart from this, fingers increase damping by increasing the surface area against the movement [34]. Adding extra mass is another drawback for the mass sensitivity.

Figure 2-14 shows the proposed resonator which has the same anchor and proof mass structure with the RCGS#1.
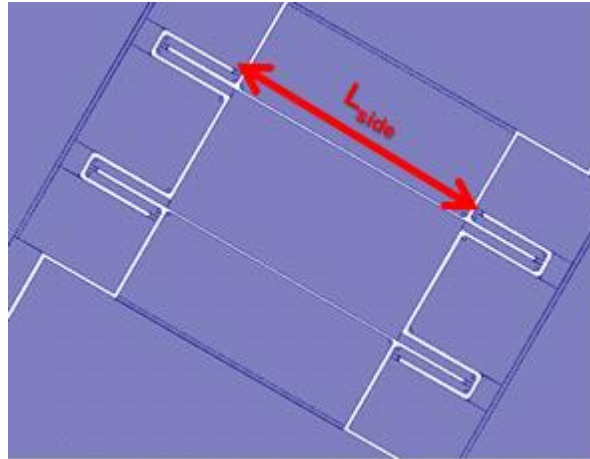
Figure 2-14 Resonator without finger

Fundamental vibration mode is presented in figure 2-15.
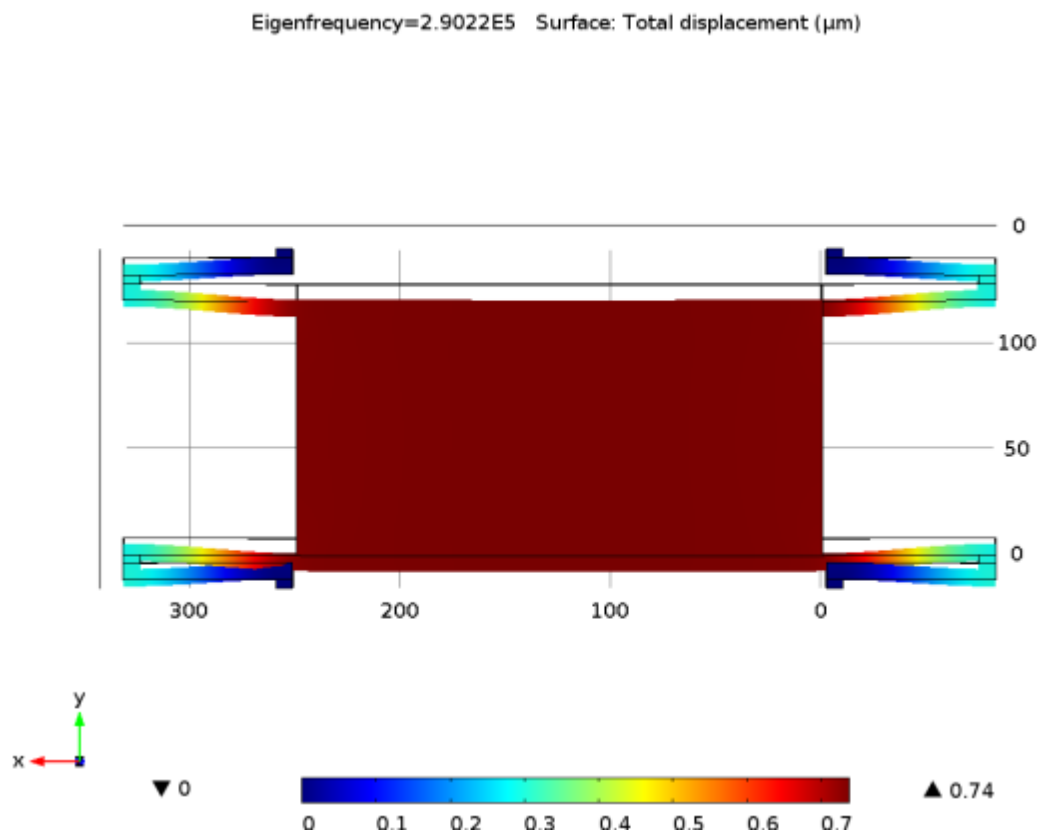
Figure 2-15 Fundamental vibration mode of RCGS 1 is at 290 kHz

Equation (2.31) expresses the change of capacitance with displacement.

$$\frac{\partial C}{\partial x} = \frac{\partial \left(\varepsilon \frac{L_{side} * h}{d_{gap} - x} \right)}{\partial x} = \varepsilon \frac{L_{side} * h}{\left(d_{gap} - x \right)^2} \tag{2.31}$$

Since the overall transfer function includes two $\frac{\partial C}{\partial x}$ terms, one for sense and the other for actuation Equation (2.32) is used for the representation of capacitive sensitivity.

$$\left(\frac{\partial C}{\partial x} \right)_{sense} * \left(\frac{\partial C}{\partial x} \right)_{act.} = \varepsilon^2 \left(\varepsilon \frac{L_{side} * h}{\left(d_{gap} - x \right)^2} \right) * \left(\varepsilon \frac{L_{side} * h}{\left(d_{gap} + x \right)^2} \right) \tag{2.32}$$

Equation (2.32) is calculated and the result is compared with the result of RCGS#1. Figure 2-16 combines the results in the same graphics. The red line denotes the result of the RCGS#1 and the blue line denotes the RCGS#2.
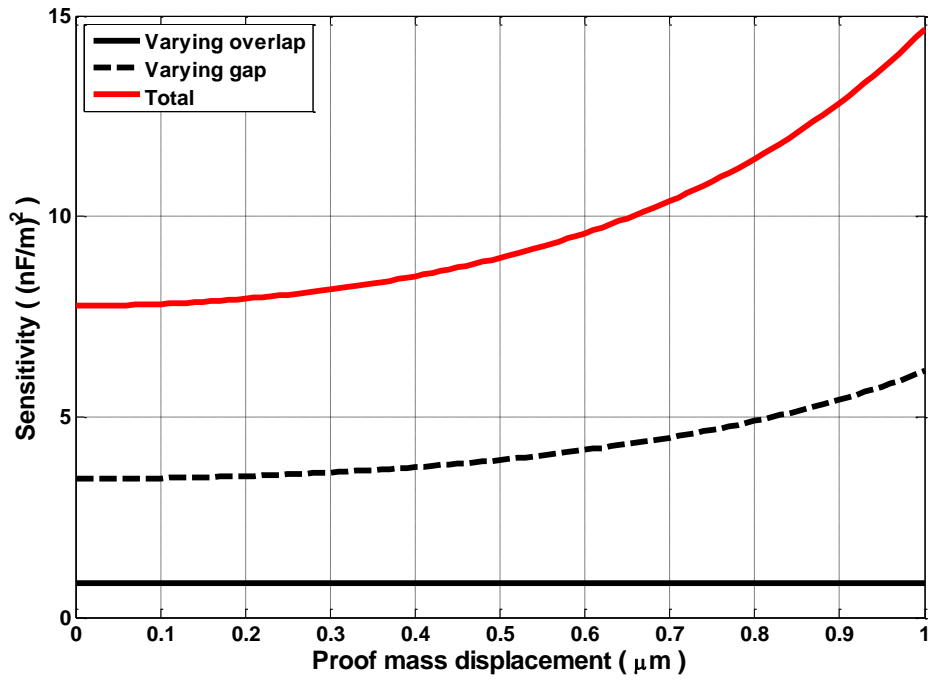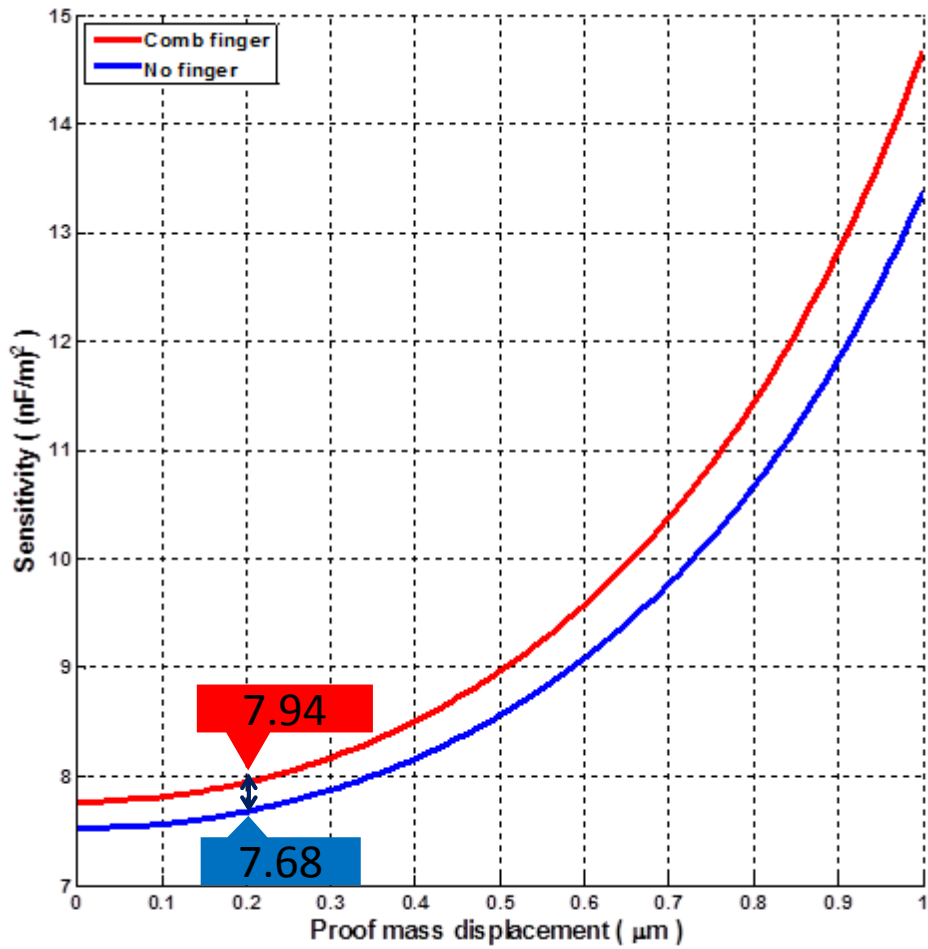
Figure 2-16 $\left(\frac{\partial C}{\partial x}\right)_{sense}$ $\left(\frac{\partial C}{\partial x}\right)_{act.}$ vs displacement is drawn for RCGS#1 (the red line) and RCGS#2 (the blue line).

Figure 2-16 shows that finger removal decreases the capacitive sensitivity around only 3% for the same displacement. Please note that, the total mass of the sensor and the damping factor is decreased, too. To see the overall effect, gain of transfer functions of RCGS#1 and RCGS#2 versus frequency is drawn in Figure 2-17 in MATLAB.

41
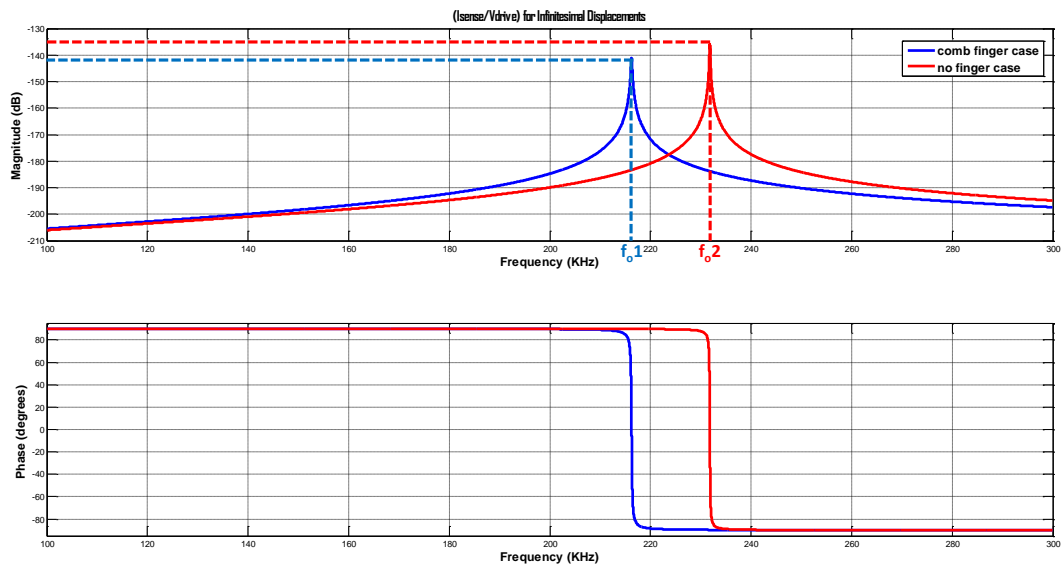
Figure 2-17 Overall transfer function for resonator with no finger (the red line) and resonator with comb finger (the blue line)

It can be seen from Figure 2-17 that the resonance frequency, the peak gain at resonance frequency and the quality factor is increased.

2.2.3 RCGS#3

Analysis of the first two designs shows that the comb fingers do not improve the output current magnitude but they increase the mass and the damping. If it is possible to use the removed finger in such an orientation to increase the varying gap area, an increase in gain will be achieved without any decrease in the resonance frequency or quality factor. This achievement will also reduce the effect of the feedthrough current by simply increasing the resonator current to feedthrough current ratio.

Figure 2-18 illustrates the proposed design. All of the four sides of the resonating structure are employed to place the fingers. The finger structures are placed so that the gap between the fingers changes with the displacement. Finger dimensions are selected so that to make them have the same weight with the fingers of RCGS#1.

While a finger getting close to one of its neighbor fingers, it also moves away from its other neighbor. Therefore displacement creates two opposite signed current at two neighbor finger that cancel each other. In order to prevent this effect, one of the

42

gaps is selected as three times of the other one and it is called anti-gap. Since the square of the gap is important and anti-gap to gap ratio is three, only 1/9 of the current is lost. The ratio is upper bounded by liquid flow protection of parylene (parylene coating prevents the liquid flow through a gap of upon 4-5 µm [23]. The gap between the fingers (d_{gap}) is chosen as 1.5µm and the anti-gap (d_{anti_gap}) as 4.5µm.
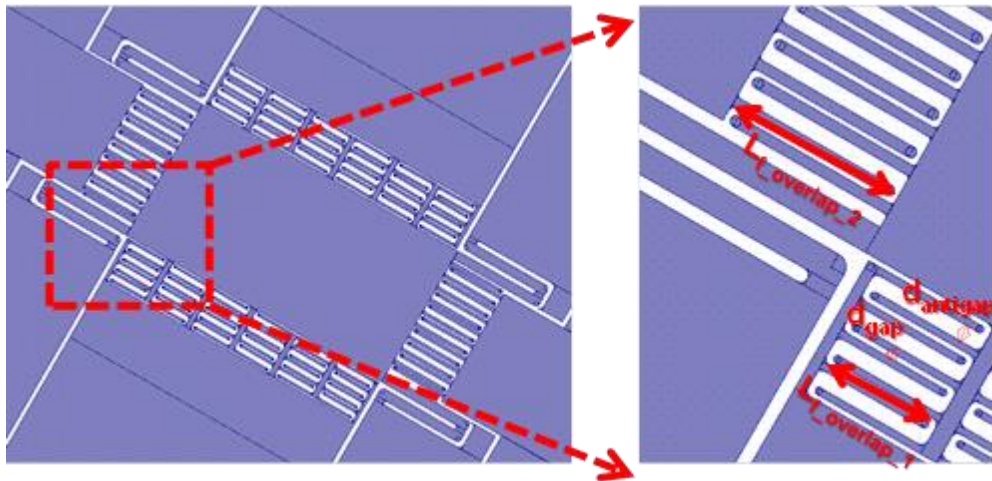
Figure 2-18 Resonator with tree structured finger

Fundamental vibration mode of the sensor is illustrated in figure 2-19.
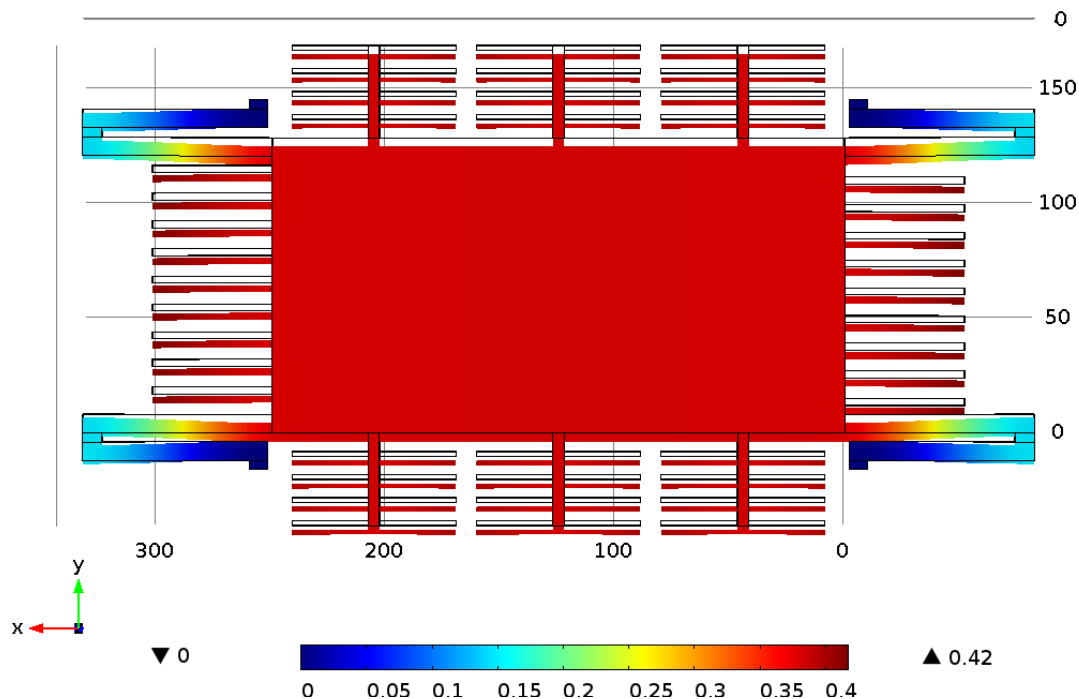
Figure 2-19 Fundamental vibration mode of RCGS 1 is at 239 kHz

Equations (2.33)-(2.35) show the transfer function calculations. There are 30 fingers at tree structured finger branch with an overlap length of ($L_{f\_overlap\_2}$) 30 µm and 9 fingers at each side with an overlap length ($L_{f\_overlap\_1}$) of 40µm.

$$\frac{\partial C}{\partial x} = \frac{\partial \left(\varepsilon \frac{L_{f\_overlap\_1} * h}{d_{gap} - x} * 30 + \varepsilon \frac{L_{f\_overlap\_2} * h}{d_{gap} - x} * 9 \right)}{\partial x} * (1 - \left(\frac{d_{gap}}{d_{anti-gap}} \right)^2)$$	(2.33)
$$\frac{\partial C}{\partial x} = (\varepsilon \frac{L_{f_{overlap_1}} * h * 30}{\left(d_{gap} - x\right)^2} + \varepsilon \frac{L_{f_{overlap_2}} * h * 9}{\left(d_{gap} - x\right)^2}) * (1 - \left(\frac{d_{gap}}{d_{anti-gap}} \right)^2)$$	(2.34)
$$\left(\frac{\partial C}{\partial x} \right)_{sense} * \left(\frac{\partial C}{\partial x} \right)_{act.}$$ $$= \varepsilon^2 * (1 - \left(\frac{d_{gap}}{d_{anti-gap}} \right)^2)^2 * \left(\frac{L_{f_{overlap_1}} * h * 30}{\left(d_{gap} - x\right)^2} + \frac{L_{f_{overlap_2}} * h * 9}{\left(d_{gap} - x\right)^2} \right)$$ $$* \left(\frac{L_{f_{overlap_1}} * h * 30}{\left(d_{gap} + x\right)^2} + \frac{L_{f_{overlap_2}} * h * 9}{\left(d_{gap} + x\right)^2} \right)$$	(2.35)

44

Equation (2.35) is calculated and compared with the resonator with comb finger in Figure 2-15.
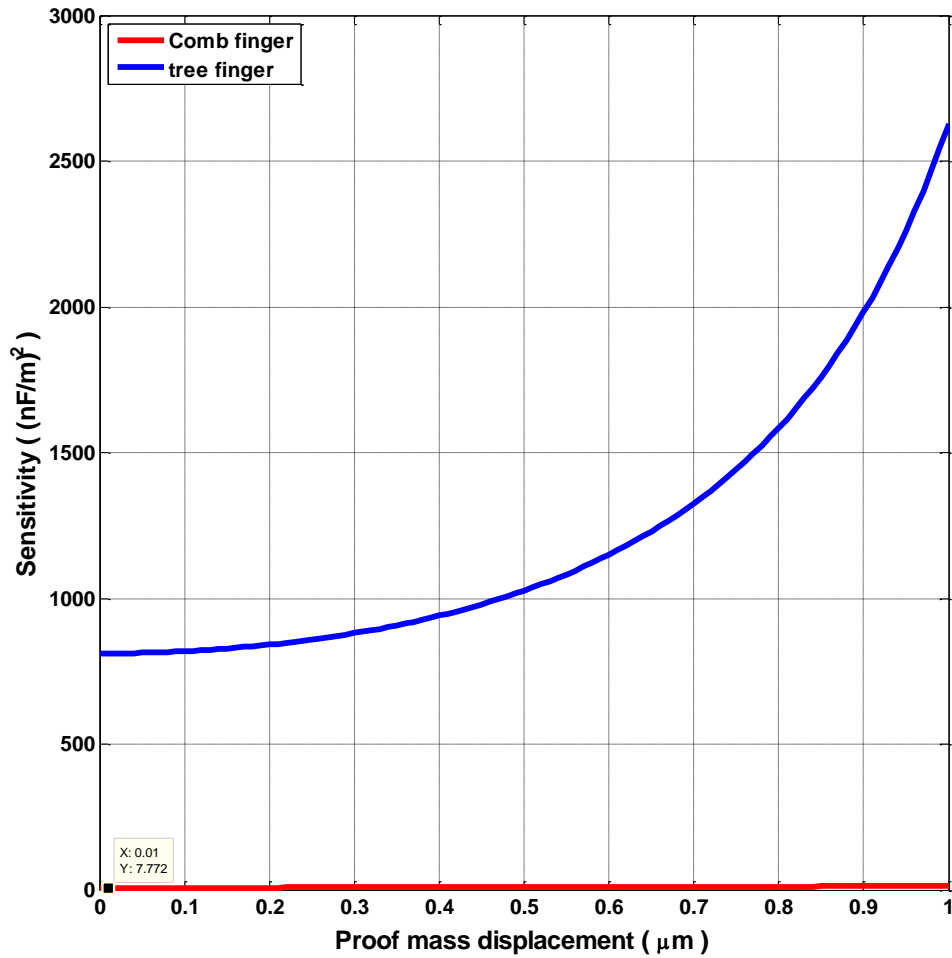
Figure 2-20 for $\left(\frac{\partial C}{\partial x}\right)_{sense}$ $\left(\frac{\partial C}{\partial x}\right)_{act.}$ vs displacement graph for comb finger and tree structured finger.

At the displacement of 0.01 μm sensitivity ratio is 104.4. Since the mass and the anchors are identical for the resonators with comb finger and tree finger structures, gain ratio of transfer function is nearly the same with the capacitive sensitivity ratio. As a result, by arranging comb finger as in this design, gain is increased around 40 dB without any change in resonance frequency and quality factor.

40 dB increments in gain should also decrease the feedthrough effect by increasing the displacement related output current to feedthrough current ratio by 100 times.

2.2.4 RCGS#4

Apart from boosting the output current of the sensor, decreasing the feedthrough current is also a good method that can be applied to eliminate the drawbacks of the feedthrough effect. In the section 2.1.3 two different feedthrough current elimination methods are described. In this design, the second method is used.

In order to eliminate the feedthrough current, a resonator structure with side finger in Figure 2-21 is designed. Two longitudinal sides are used for actuation signals and side fingers are for creating capacitive sensing currents. Note that the actuation signals should be opposite signed and the sense signals have 180° degree of phase difference due to opposite orientations of gap and anti-gap. Taking difference of the sense currents eliminates the feedthrough current and adds up the displacement related currents.
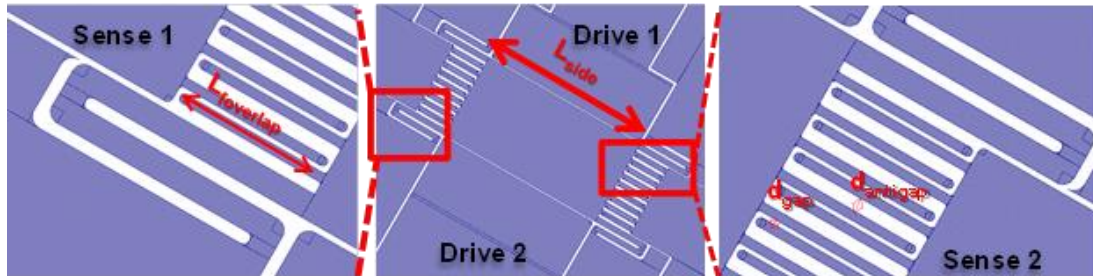
Figure 2-21 Resonator with side fingers

Fundamental mode of related sensor is given in Figure 2-22.

Eigenfrequency=2.5795E5 Surface: Total displacement (µm)
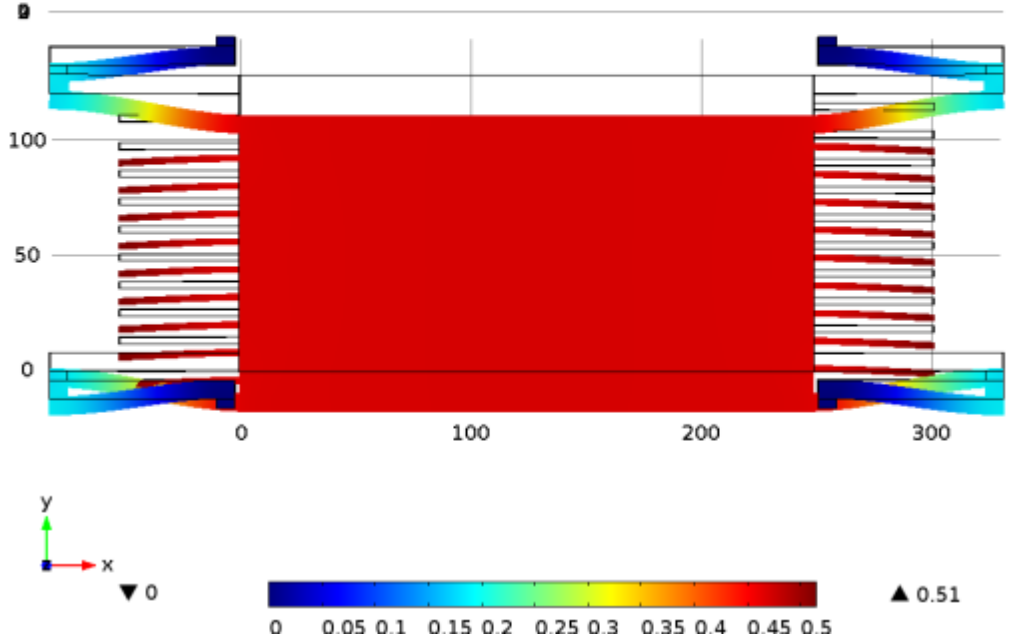
Figure 2-22 Fundamental vibration mode of RCGS 1 is at 257.9 kHz

Let's derive the transfer function of the sensor:

$$H_{total}(s) = \frac{I(s)}{V(s)} = \frac{s(V_{DC})^2 (\frac{\partial C}{\partial x})_{sense}(\frac{\partial C}{\partial x})_{drive}}{ms^2 + bs + k}$$

(2.36)

$$\left(\frac{\partial C}{\partial x}\right)_{act.} = 2 * \varepsilon \frac{L_{side} * h}{\left(d_{gap} - x\right)^2}$$

(2.37)

$$\left(\frac{\partial C}{\partial x}\right)_{sense} = 2 * (\varepsilon \frac{L_{f_{overlap}} * h * 9}{\left(d_{gap} - x\right)^2}) * (1 - \left(\frac{d_{gap}}{d_{anti-gap}}\right)^2)$$

(2.38)

Thanks to side fingers, RCGS#4 has higher gain than the RCGS#1 and RCGS#2. Although it has less gain than RCGS#3, damping and mass of this resonator is smaller.

2.2.5 RCGS#5

It is mentioned that finger structures increases the damping by increasing the resistive surface against the movement direction. In order to improve the resonator with side fingers in terms of damping (quality factor and mass sensitivity), a sensor without finger structure is also designed.

The feedthrough current elimination method used in RCGS#4 needs four different ports where two of them are for the sense and two of them are for the actuation. Moreover, the displacement of the resonator must create opposite signed capacitive change on the sense ports.

Creating a varying gap capacitive interface by tilting the right and left edges of the moving part, as it is seen in the Figure (2-23), is the proposed design solution. Please note that, suspended mass moves away from one tilted sense electrode as it gets closer to the other sense electrode. This is the reason of the opposite signed capacitive change at the two sense ports.
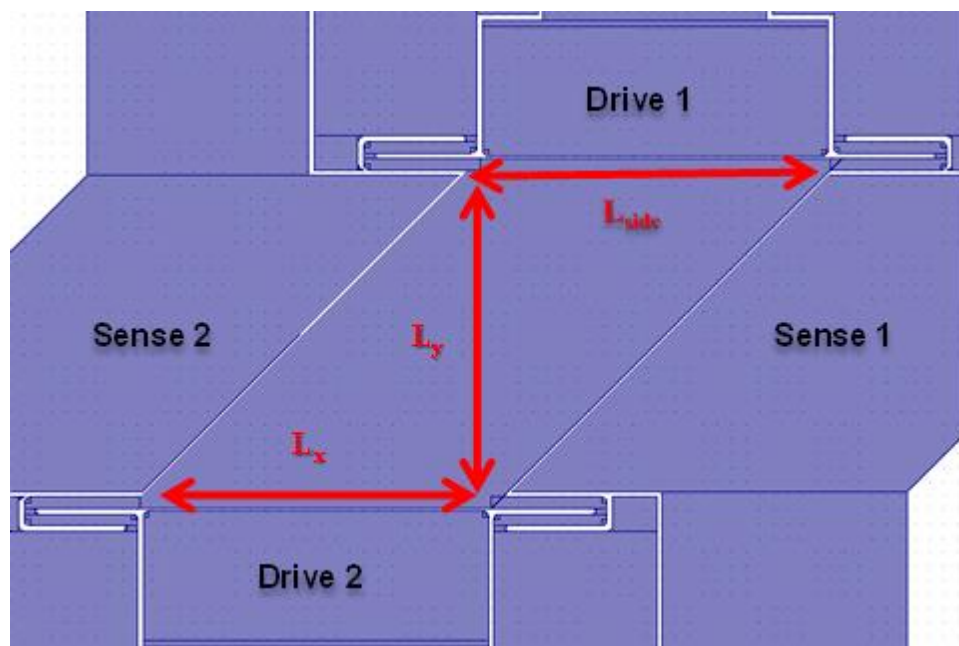
Figure 2-23 Diamond shaped resonator

Fundamental mode of RCGS4 is given in Figure 2-24.
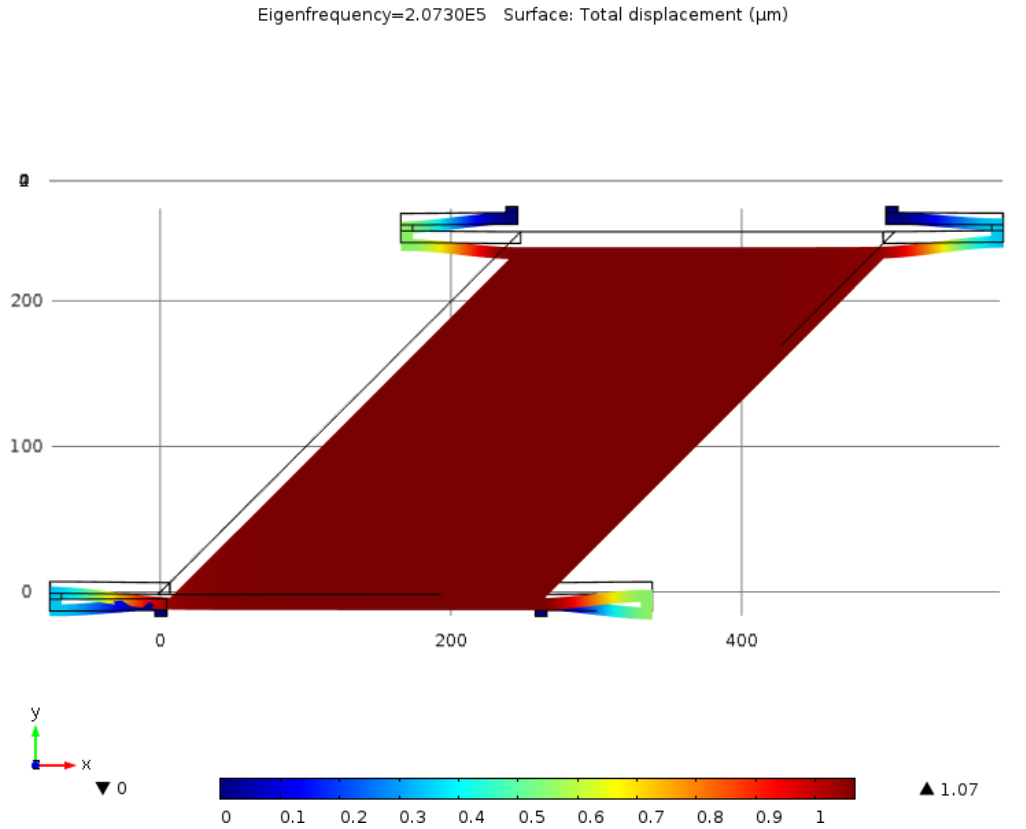
Figure 2-24 Fundamental vibration mode of RCGS 1 is at 207.3 kHz

Equations (2.39-2.41) simply show the related transfer function.

$$H_{total}(s) = \frac{I(s)}{V(s)} = \frac{s(V_{DC})^2(\frac{\partial C}{\partial x})_{sense}(\frac{\partial C}{\partial x})_{drive}}{ms^2 + bs + k} \qquad (2.39)$$

$$\left(\frac{\partial C}{\partial x}\right)_{drive} = 2 * \varepsilon \frac{L_{side} * h}{\left(d_{gap} - x\right)^2} \qquad (2.40)$$

$$\left(\frac{\partial C}{\partial x}\right)_{sense} = 2 * \left(\varepsilon \frac{L_y * h}{\left(d_{gap} - x\right)^2}\right) \qquad (2.41)$$

For the sake of symmetry, length and width of the proof mass are chosen as the same length with the previous resonators. Therefore, the mass of the resonator is approximately twice of the resonator without finger.

2.2.6 Design Procedure Summary

It is inevitable for design of the proposed gravimetric sensor to have a wide surface area for cell capturing. It is also straightforward that the mass of the sensor should be as small as possible to increase the mass sensibility. These two design criteria limits the surface area of the sense and drive capacitances. Therefore, an optimization to increase the effectiveness of the capacitive surface has been done. Another important issue that is considered during the design procedure is the feedthrough current. To eliminate the feedthrough current two methods were investigated.

In order to show the validity of the theoretical work experimentally, four new sensors were designed. Purpose of the RCGS#2 is to show that the comb fingers of the previously proposed sensor do not contribute to actuation and sensing significantly but decrease the mass sensitivity by increasing the mass and damping. RCGS#3 is proposed to show that by just changing the orientation of the finger mass, it is possible to increase the gain almost two orders of magnitude. By increasing the output current, it is aimed to reduce the effect of feedthrough current and make self-oscillation feasible. RCGS#3 and RCGS#4 have two differential sense ports to eliminate the feedthrough current. RCGS#3, that employs side fingers, has anchor symmetry of both on x and y axis whereas RCGS#4, diamond shaped resonator, has only one axis symmetry. On the other hand, RCGS#4 has less damping due to lacking of the fingers.

Table 2.1 compares the four new designs and one previous design in terms of mass, resonance frequency, quality factor and gain at resonance frequency. It is purposely avoided to give specific numbers related with fabricated sensor in comparison chart. Condition of having same proof mass and anchor dimensions (only the diamond

shaped resonator has larger proof mass) is enough for the correctness of the following table.

Table 2-1 Important parameters of different resonator designs.

Sensor	Mass	Resonance Frequency	Quality Factor	Max. Gain	Sense Type
RCGS#1	m	f	Q	G	Single
RCGS#2	<m	>f	>>Q	~G	Single
RCGS#3	m	f	Q	>>G	Single
RCGS#4	<m	>f	>Q	>>G	Differential
RCGS#5	~2m	<f	>>Q	>G	Differential

In the next chapter fabrication process of the designed sensor is investigated.

CHAPTER 3

FABRICATION

In this chapter, the microfabrication methods and process flow of the cell detection device are presented. There have been several process flows for different generations of resonators during the studies conducted for the resonant based cell detection sensors in BioMEMS group [22], [32], [33]. In this thesis the previous generation process flow is utilized due to its high mechanical yield [33]. Besides, a newly developed process flow is presented to solve the problems encountered during the previous generation fabrication is presented.

Proposed process flows employ the SOI (Silicon-on-Insulator) technology, glass micromachining, wafer bonding, and polymer micromachining.

3.1 Previous Generation Process Flow

Figure 3.1 shows the previous fabrication process flow which is the base of the newly proposed process flow in the scope of this thesis [33].

1. Lithography and wet metal etch to pattern bioactivation metal

2. Lithography to pattern PR as Si etch mask

3. Active Si layer patterning by DRIE with oxide as an etch stop

4. Metal coating and lithography on glass wafer for metal mask of HF etch (recess)

5. Wet etch for metal layer, HF etch for glass

6. Metal coating and lithography on glass wafer for metal mask of HF etch (microchannel)

7. Metal coating and lithography on glass wafer for metal mask of HF etch (microchannel)

8. Metal coating and lithography on glass wafer for contact pads and routing metal patterning

9. Glass wafer after routing metals and contact pads patterning

10. Anodic bonding

11. Handle layer removal with DRIE

12. Oxide layer removal with BHF and parylene coating
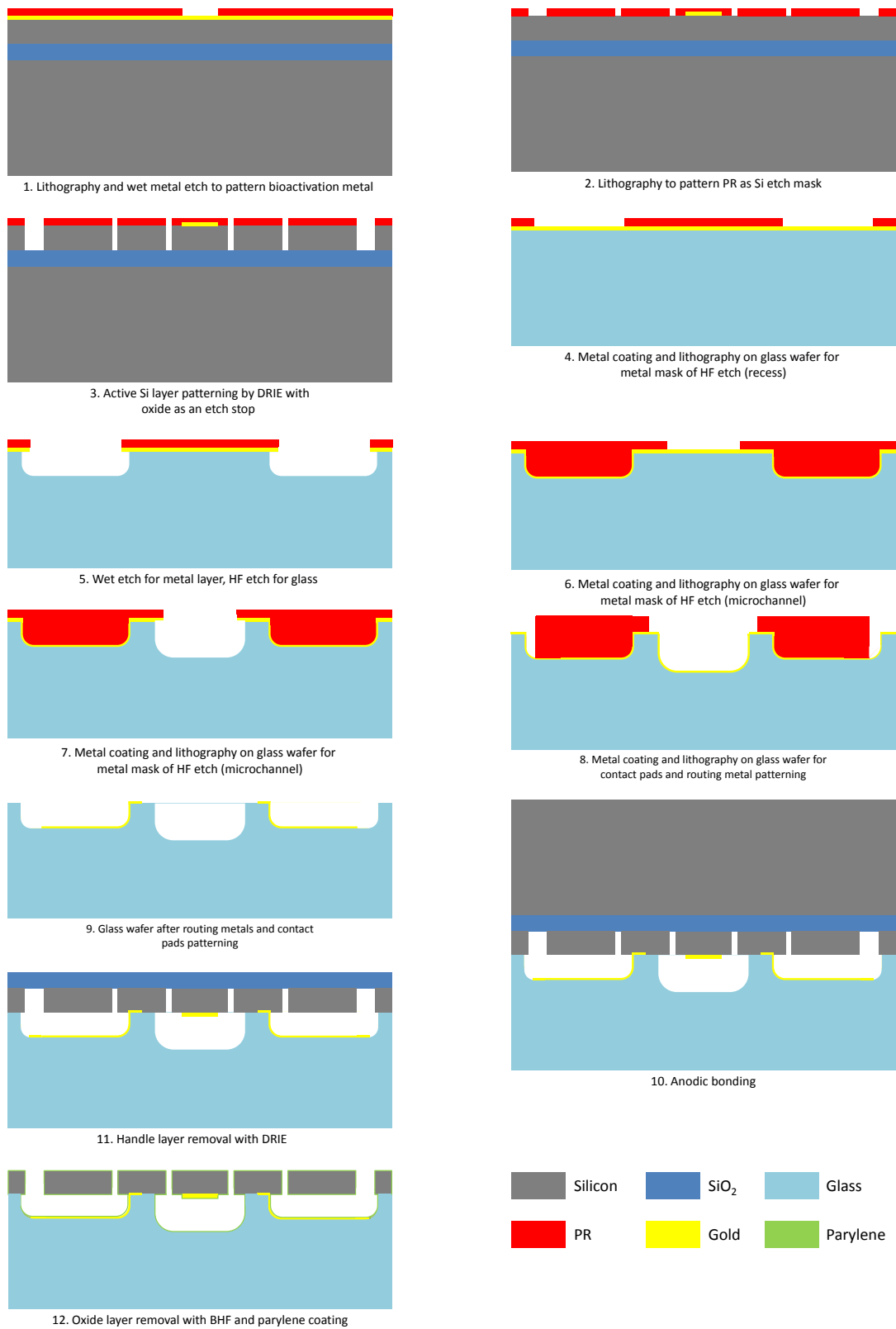
Silicon SiO$_2$ Glass
PR Gold Parylene

Figure 3-1 Previous generation process flow

In the previous generation fabrication flow, the resonators were fabricated with the two wafers; SOI (Silicon-on-Insulator) wafer for the resonator structures and the glass wafer to form the microchannel and a base for the suspended resonators.

SOI wafer which is used to form the structural layer; has a structural silicon layer thickness of 5 µm, oxide thickness of 2 µm, and handle layer thickness of 350 µm. The SOI process starts with the Cr/Au deposition (30nm/300nm) on the structural silicon layer. Deposited Cr/Au is wet etched with the commercial etchants to pattern the bioactivation area. The next step of the SOI process is Deep Reactive Ion Etching (DRIE). DRIE is chosen as it is an anisotropic etching method for the silicon and enables creating sharp vertical structures. Besides this, oxide layer of the SOI wafer behaves as an etch stop layer for DRIE. Although oxide is an etch stop layer, time optimization is still important to prevent the "notching" effect. Microposit S-1813 type photoresist is used as the masking layer in both Cr/Au etching and DRIE processes. The purpose of using this photoresist is to have relatively small deposition thickness (~1.5 µm at 4000 rpm). In order to produce critical dimensions around 1 to 2 µm having thin photoresist layers is essential. It is also important that before photoresist coating, the wafer should be dehydrated and exposed to nitrogen flow in desiccators to improve surface adhesion. Figure 3-2 shows the microscope image after the SOI process is finished.
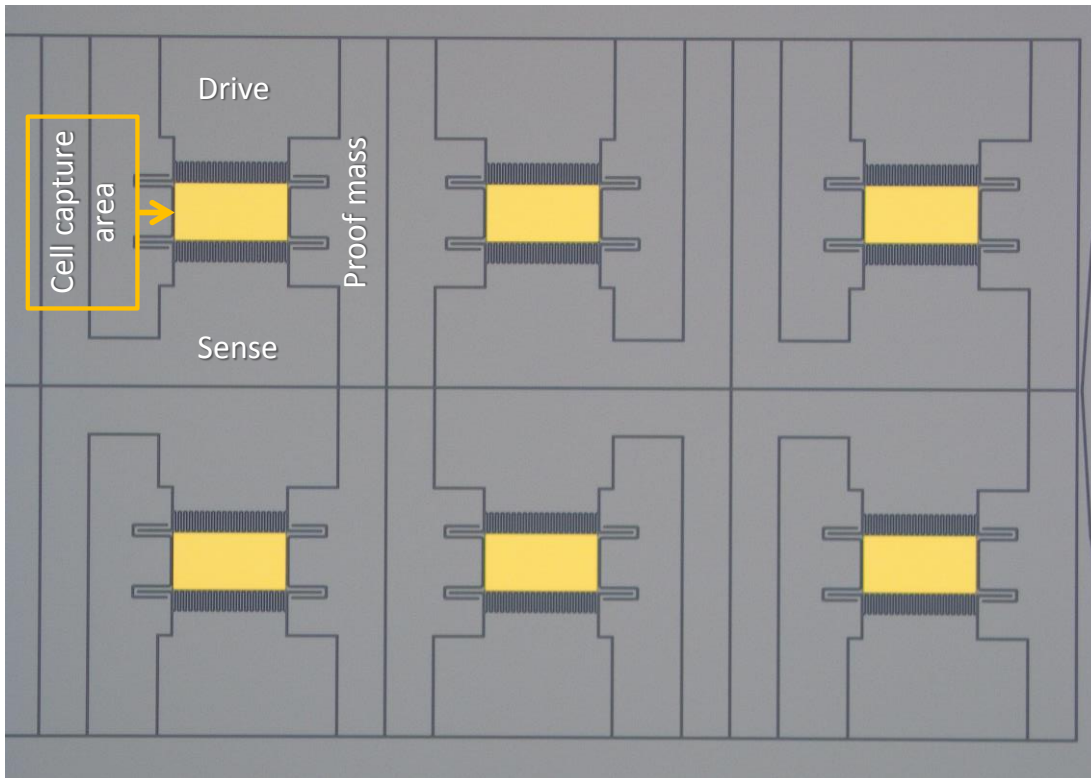
Figure 3-2 Microscope image of the resonator site of the SOI wafer

Glass wafer is processed in parallel with the SOI wafer process. Fabrication flow on the glass wafer starts with Cr/Au sputtering and patterning. Metal layers serve as a mask for pure Hydrofluoric acid (HF) wet glass etching. Similar with SOI process, metal is patterned with commercial wet etchants after photolithography. When the mask is ready, glass wafer is etched with pure HF to form the recess gap. Photoresist and metal layers are stripped of once wet HF etch is finished.

Glass wafer is etched to shape cavities for both recess gap of metal routings and resonators, and microchannel consecutively with different masks. These two etchings are done separately since the depth of the gaps is different. Therefore, the same steps are repeated for the microchannel gap, only HF etch time of recess gap is longer.

When glass etchings finished, wafer is coated with Cr/Au (30nm/300nm) to pattern metal routing lines and contact pads. Photolithography of the second metal mask and metal routing lines is done with a photoresist with high film thickness (spray coating

56

of S1813 photoresist around 5.5 µm thick film) as there are deep trenches in the glass wafer and it is essential for resist to protect these features. This enables proper development of the photoresist film inside the recess gaps with fine borders formed. Figure 3.3 shows microscope view of the glass wafer after related process is finished.
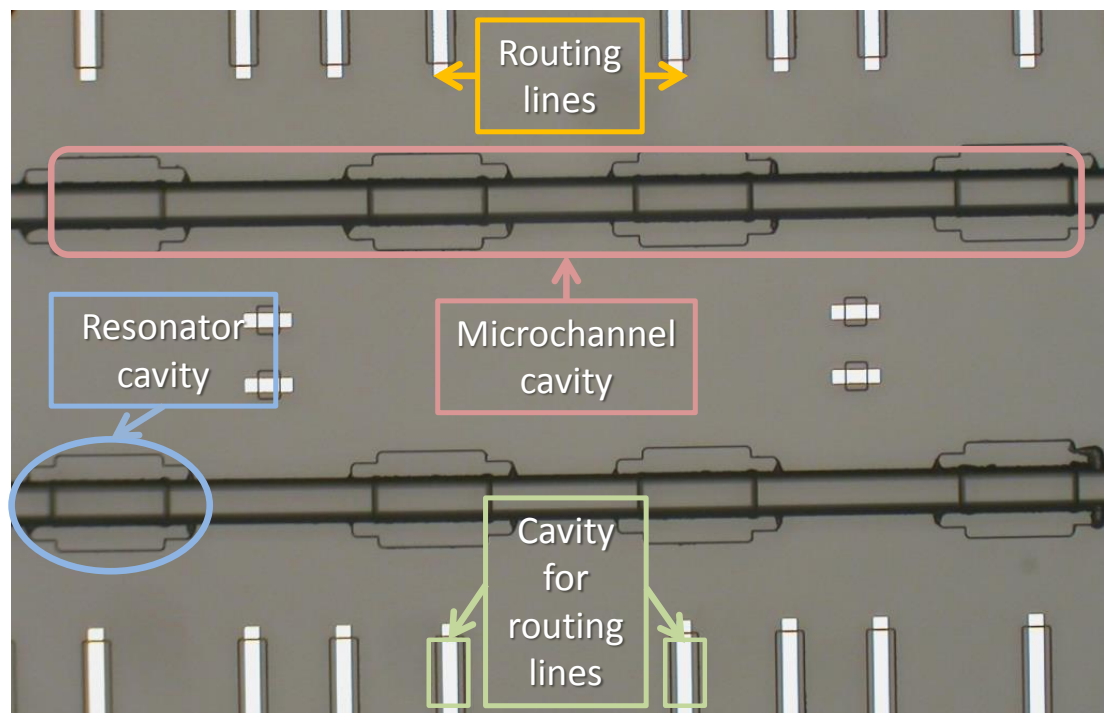
Figure 3-3 Microscope image of Glass wafer

After finalizing the processes on both of the wafers, SOI and glass wafers are anodic bonded. Before bonding, a cleaning procedure in piranha and buffered HF (HF diluted in NH_4F) is necessary to remove any particle between the wafers. Bonding process is done with the EVG 501 brand universal wafer bonder system by applying a bias voltage of 1200V, piston force of 1500 N, and bonding temperature of $370^{\circ}C$ on the wafers. Microscope view through glass side after bonding can be seen in Figure 3-4.
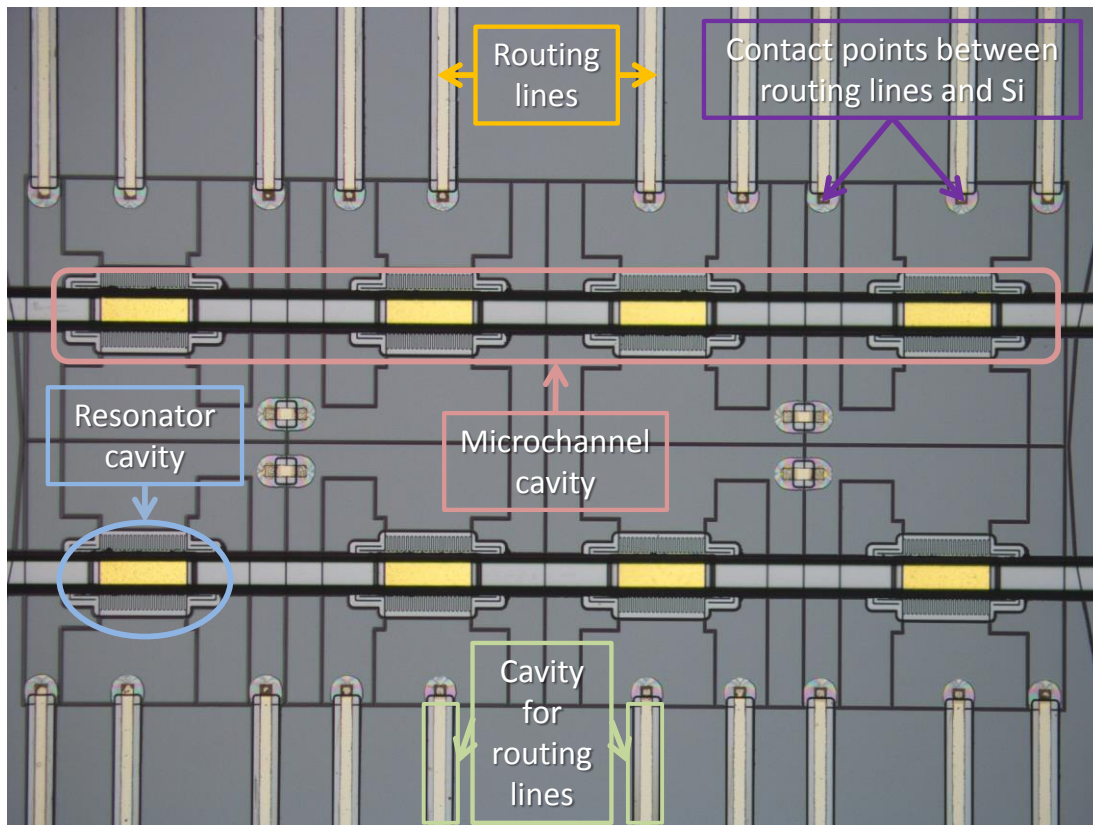
Figure 3-4 Microscope view through glass wafer after anodic bonding

In order to release the resonators, handle and oxide layers of the SOI wafer should be removed. DRIE is used for removal of the handle layer of the SOI wafer. After that, the oxide layer is etched with BHF solution (1:5). In order to remove the BHF, wafer is cleaned in DI water for a long time. Vaporization of water is harmful for the suspended resonators due to surface tension. Instead of vaporizing, drying process is done by bathing the resonator in the order of acetone, isopropyl alcohol (IPA), and methanol. As a last step of drying, methanol is vaporized on a hot plate at 70°C.

The last part of the fabrication is parylene layer coating with CVD. Wafer is coated with 0.5µm of Parylene-C. During deposition, parylene vapor flows through all gaps and coats the whole surfaces including sides of fingers and top and bottom of the resonator. However, parylene is not desired on top of the bioactivation gold to make surface activation for selective cell capture possible to direct contact with the gold layer. To etch the parylene on bioactivation gold, wafer is placed inside oxygen plasma for an optimized short period . Parylene thickness is thinner inside the

channel while comparing with the surface of the fingers. Therefore, parylene on bioactivation gold is etched by oxygen plasma before the parylene on the surface of the fingers.

Figure 3-5 shows the one die after dicing the wafer.
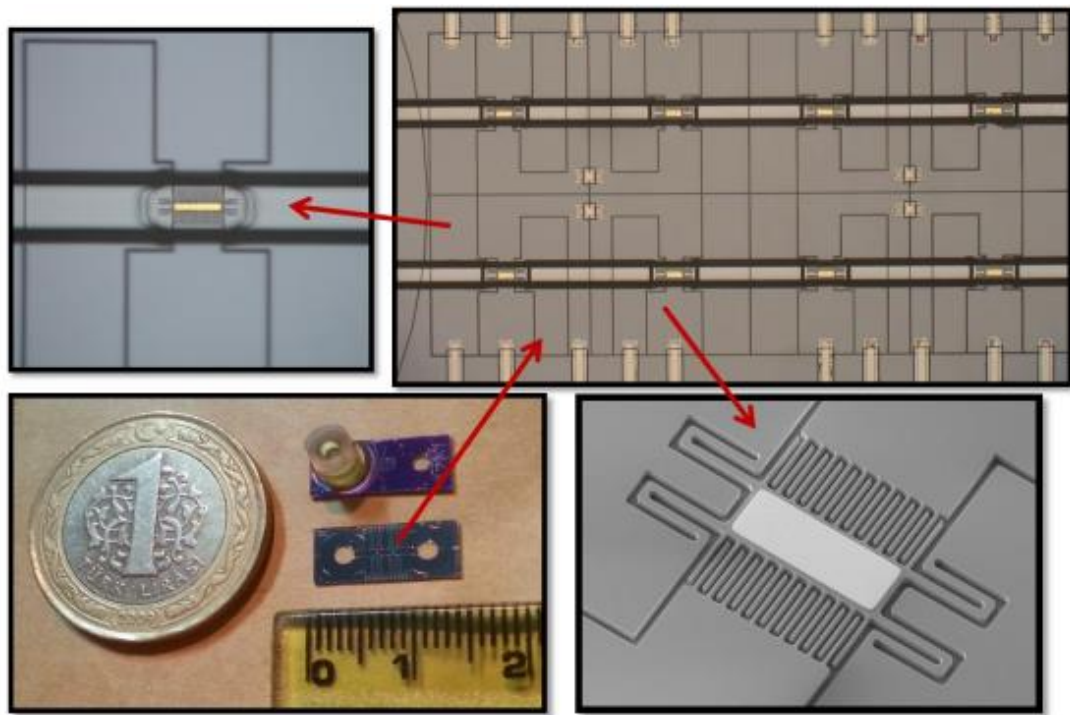
Figure 3-5 Photograph of a microresonator device fabricated with previous generation process flow [33].

3.1.1 Problems related with previous fabrication process flow

Although this fabrication flow works with mechanically high yield, there are still some problems. Following parts describes the fabrication process and masks originated problems that some solutions are proposed.

3.1.1.1 Undesired contacts between separate silicon islands

During the experiments of the resonators that were fabricated with the previous process flow, it is observed that the proof mass pulls current when a DC voltage is applied. Theoretically, the proof mass cannot pull current since it is isolated from other parts, which means there should be no resistive contact between proof mass and ground potential. The only reason for this to happen is a contact between the

59

proof mass and the other ports that are DC-grounded. In order to understand the place of the contact, laser cutter is used. Cr/Au lines were cut at the edges of the each separate silicon island. After cutting the lines at the edges of the drive, sense, and proof mass parts, current on proof mass was disappeared. This result shows that there are some particles inside the recess gaps that create a resistive path through metal line to substrate silicon. Figure 3.6 shows the contact point of gold lines to the proof mass, sense and drive parts of the resonator and the part that broken with laser cutter.
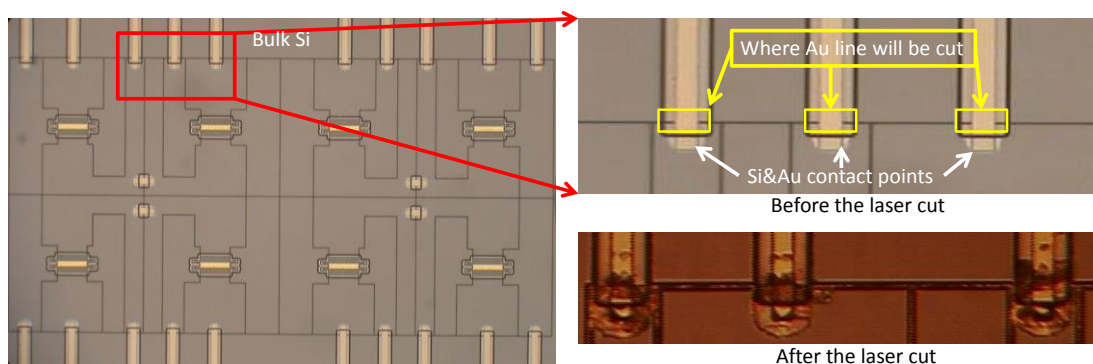
Figure 3-6 Gold lines in recess gap creates undesired resistive path between Si islands. Yellow rectangles show the parts that would be broken by laser cutter in order to prevent proof mass current leakage.

3.1.1.2 High feedthrough current

As described in chapter 2, high feedthrough current causes operational troubles. Results of tests conducted on the resonators fabricated with the previous flow shows that the feedthrough capacitance is about 50 fF, which causes relatively high current on high frequencies. As seen from the Figure 3-7, contact pads for drive and sense ports of a resonator is on the same side of the die. Since wirings of these two ports are very close to each other, a high feedthrough capacitance is formed between them.
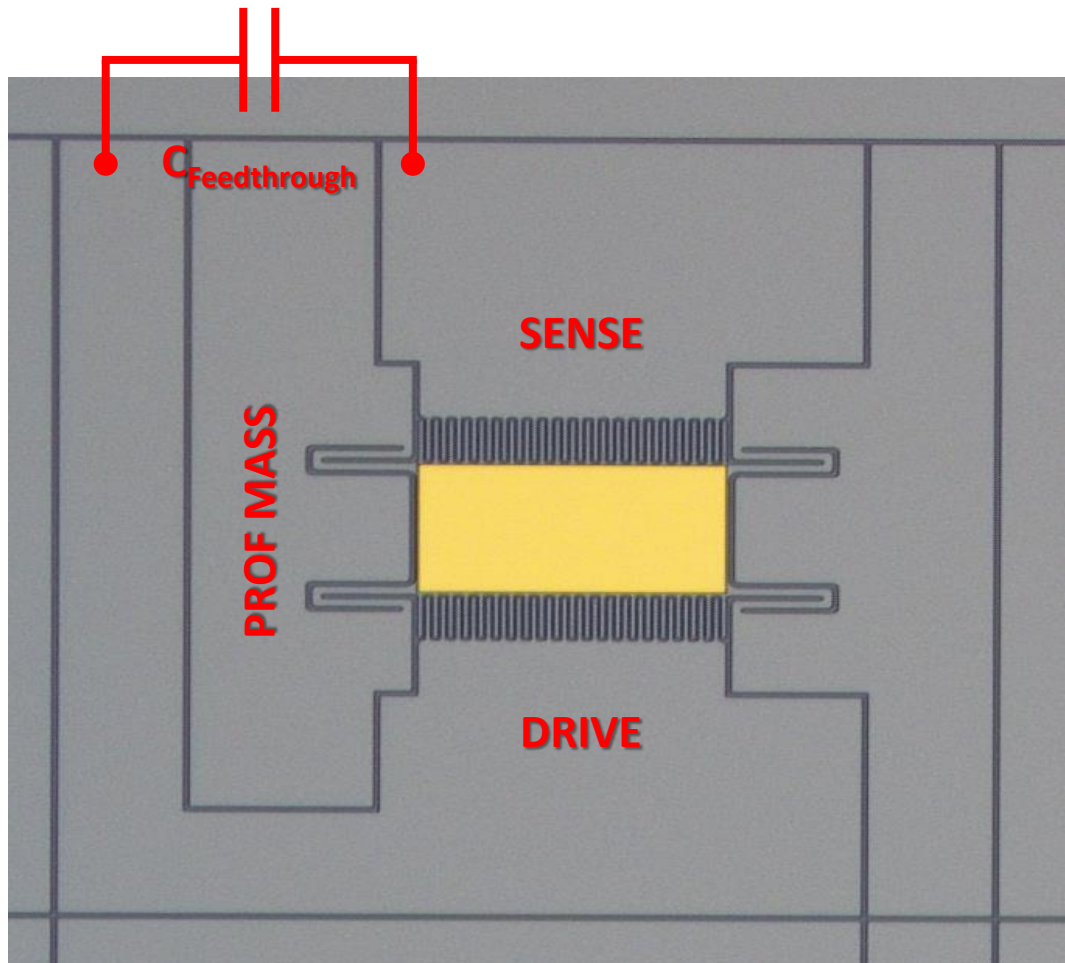
Figure 3-7 Illustration of feedthrough capacitor on resonator

3.2 New Generation Process Flow

To overcome the problems related with the previous generation fabrication flow, a modified process flow with the new mask set was proposed. In this flow, metal routings are removed from the inside of the recess gaps of glass wafer to prevent the contacts between separate silicon islands. Moreover, the orientation of the contact pads is changed to reduce the feedthrough current. Figure 3-8 illustrates the process flow.

1. Lithography and wet metal etch to pattern bioactivation metal and metal lines

2. Lithography to pattern PR and Si etch by DRIE

3. Metal coating and lithography on glass wafer for metal mask of HF etch (microchannel & recess)

4. Wet etch of metal mask, HF etch of glass for recess and microchannel patterning

5. Wet etch for metal to pattern metal routings and contact pads

6. Anodic bonding

7. Handle layer removal with DRIE

	Silicon		SiO$_2$		Glass
	PR		Gold		Parylene

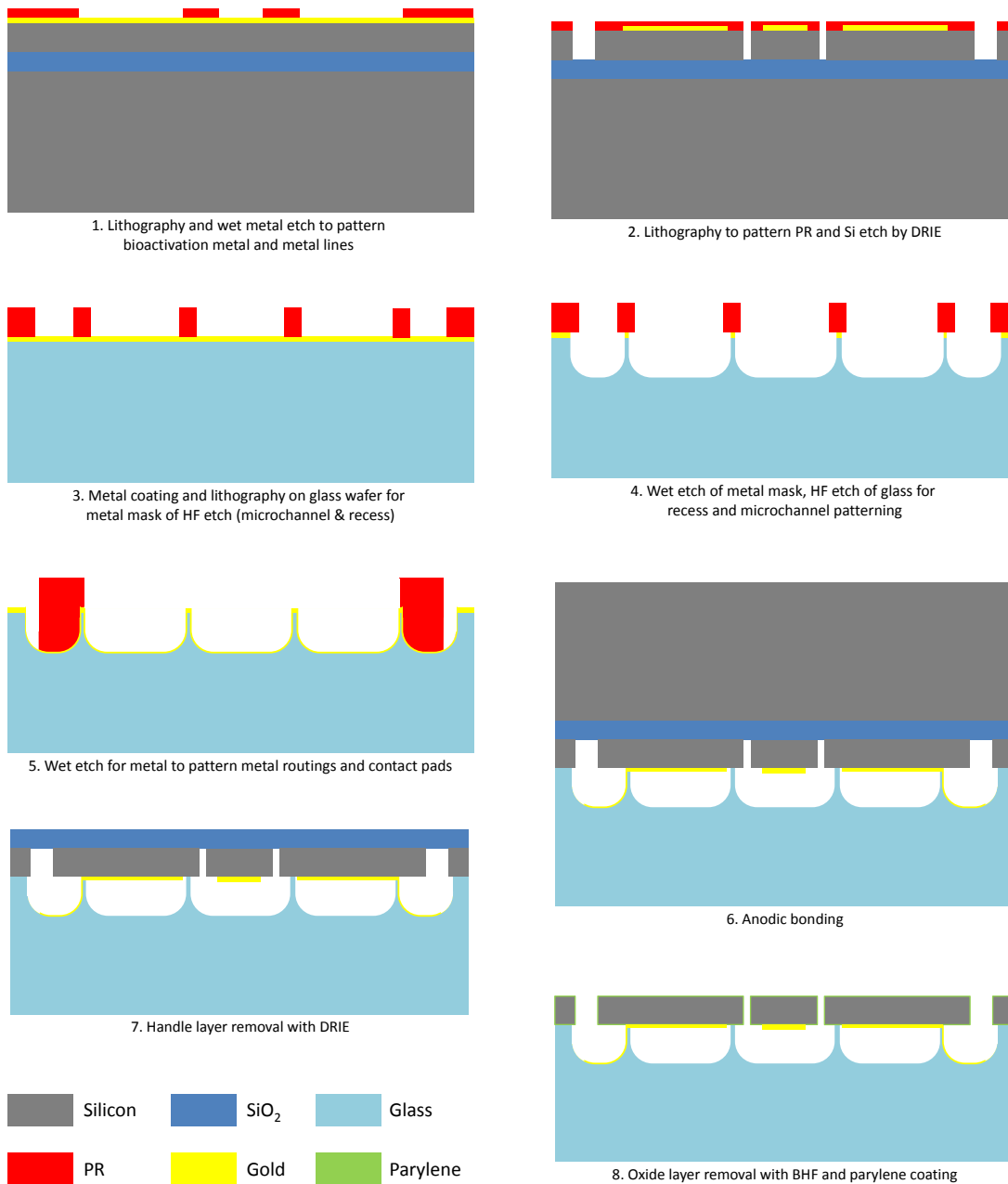8. Oxide layer removal with BHF and parylene coating

Figure 3-8 New generation fabrication flow

The fabrication process of the SOI wafer starts with the bioactivation Cr/Au (30nm/300nm) deposition and the SOI patterning with DRIE as in the previous generation process flow. However, in this case silicon islands of drive, sense, and proof mass continues until contact pad area. Note that in the previous flow, resonators are circled by the bulk Si and the metal routings are placed inside the

glass wafer to connect the resonator parts to the related contact pads. The purpose of this change is to avoid the resistive path between silicon islands due to metal routings and substrate silicon interaction. Possible drawback of relatively long silicon path is high series resistance between contact pad and actuation/sensing capacitors. In order to drop the resistivity, Cr/Au lines are deposited on top of the silicon paths in the bioactivation metal patterning steps. Figure 3-9 shows the microscope image of the SOI wafer after the related processes are finished.
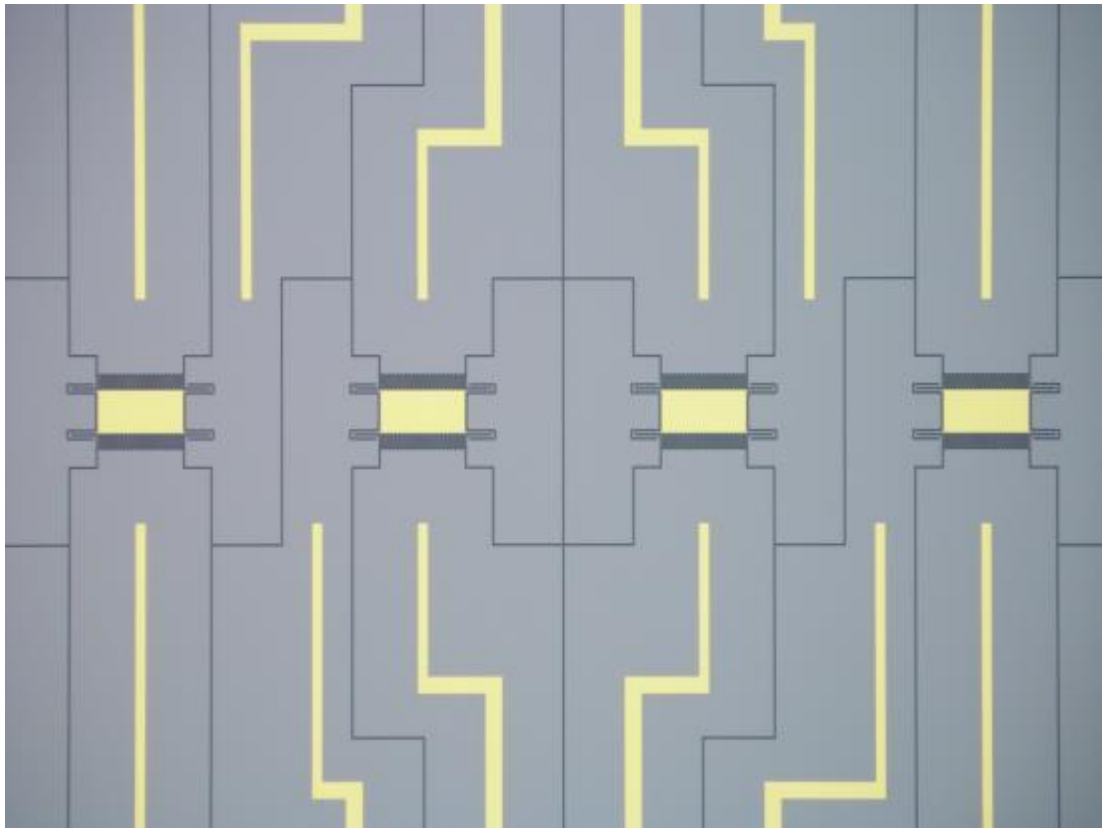

Figure 3-9 Microscope image of SOI wafer

SEM images of each resonator after SOI process are presented in Figure 3-10.

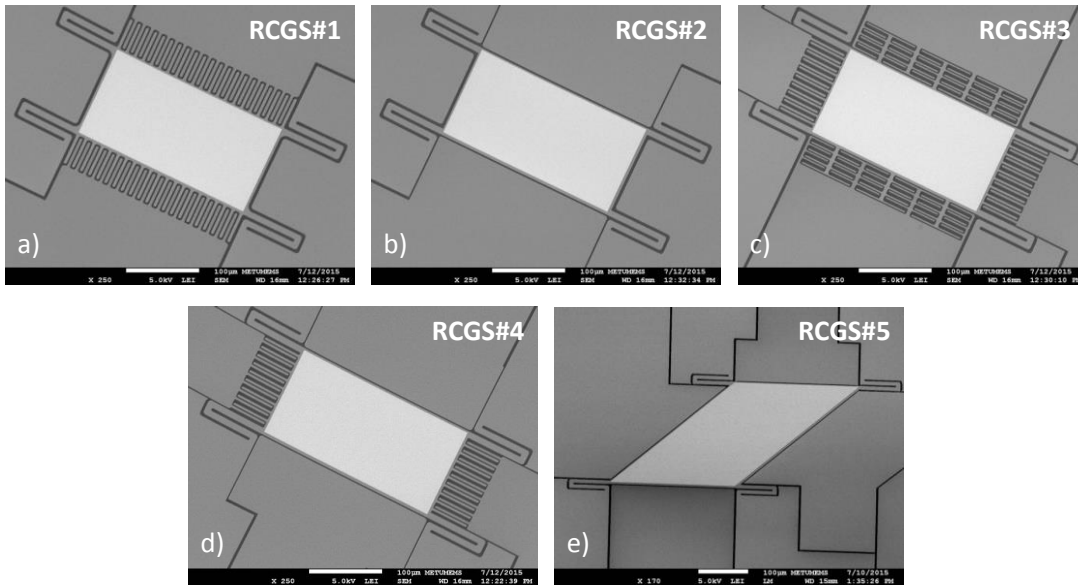Figure 3-10 SEM images of each resonator type

Another difference from the previous generation process flow is the locations of the contact pads. As seen from the SEM images of the SOI on Figure 3-11, drive and sense ports are placed across the die to reduce the feedthrough capacitance. Experimental results show that feedthrough current drops to about 500 aF (1/100 of the previous generation resonators).
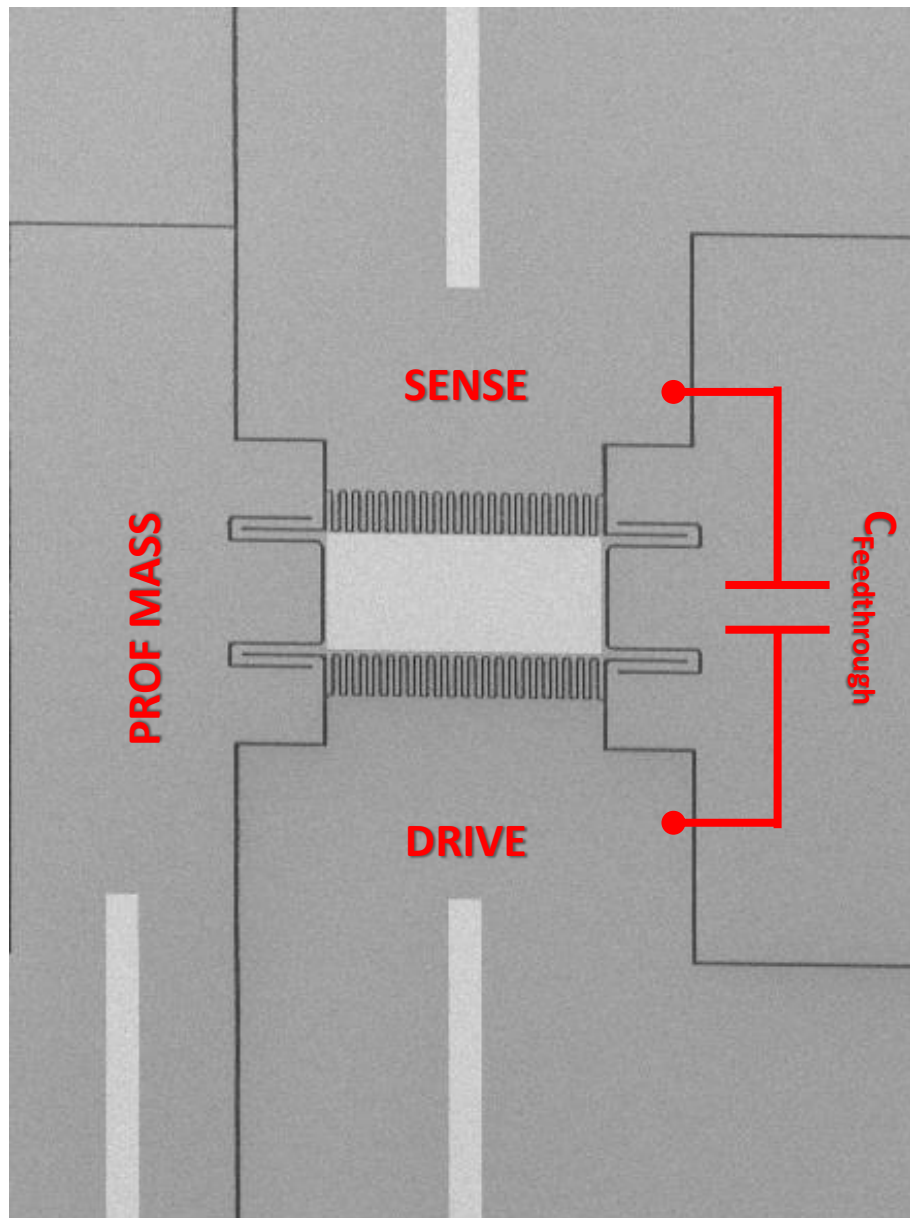
Figure 3-11 Scanning electron microscope (SEM) view of a resonator after structural DRIE step

During the glass process, two different etch for recess gaps and microchannel is no more necessary since there are no metal wirings inside the recesses. Only the wire bond pad and the related routing lines are patterned inside the recess gaps. Therefore, single pure HF wet glass etch is enough. Metal patterning is done to create a mask for the HF etch. After the glass etch, the metal mask is stripped and the sharp trenches created by the aggressive pure HF etch is smoothened in BHF.

Then, the glass wafer is coated with Cr/Au (30nm/300nm). As in the previous generation fabrication flow, wet etch of metal layers are done after photolithography to form contact pads. An image of the glass wafer after related processes is presented in Figure 3-12.
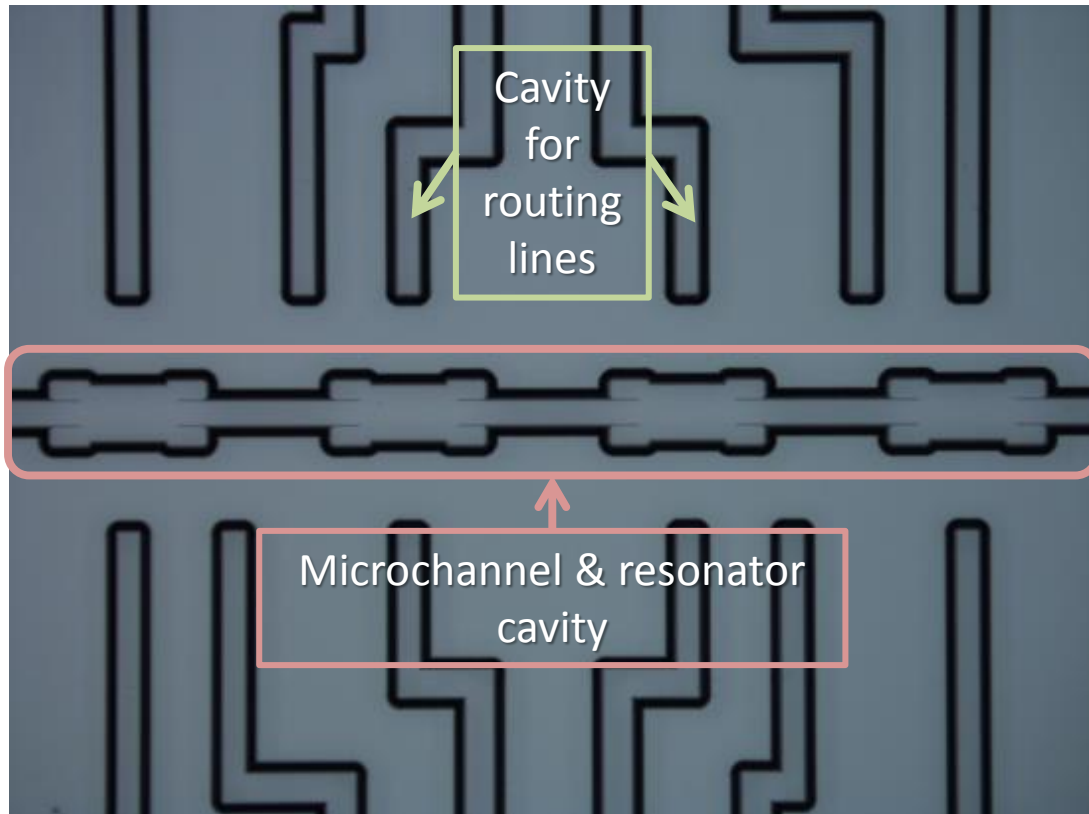

Figure 3-12 Microscope image of glass wafer after process completed

Remaining parts are the same with the previous fabrication flow (Anodic bonding, handle layer removal and parylene coating).

3.3 Fabrication Summary

Used fabrication process flows during the fabrication of resonators have been given in this chapter. Previously proposed flow investigated and related problems and possible solutions have been analyzed. In the light of these analyses, an updated process flow is used to fabricate designed resonator. After fabrication, wafers diced into single dies and input/output ports were mounted to let liquid inside the microchannels. Figure 3-14 shows the final form of a die.
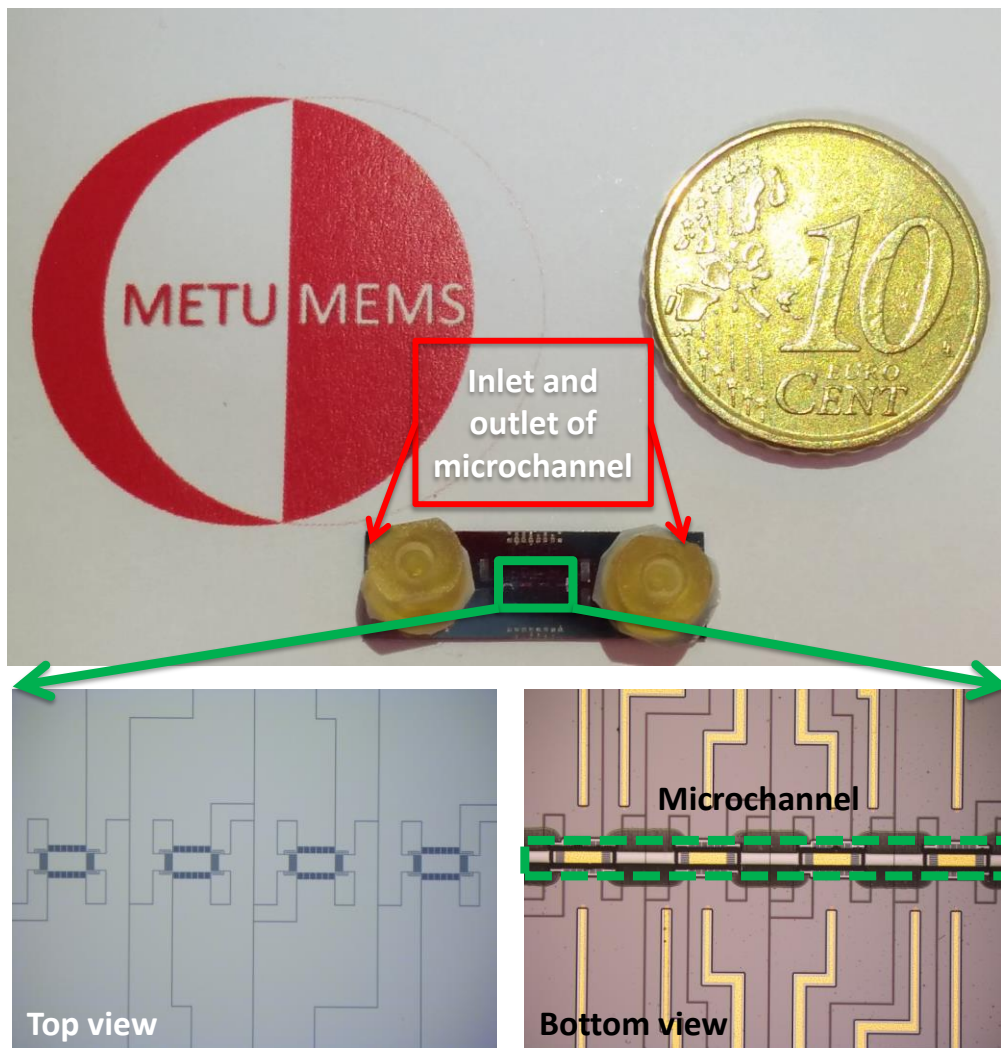
Figure 3-13 Photograph of resonant mass sensor device integrated with microfluidic channel cap and fluidic connections.

Next chapter presents the experimental data of the fabricated sensors along with experimental setup.

CHAPTER 4

EXPERIMENTAL RESULTS

This chapter provides information about the experimental work on the fabricated sensors. First, designed interface circuit is presented. Then the experimental setup is shown. Next, the resonance characterization results of the devices in air are given. After that feedthrough elimination results are emphasized. Finally, chapter is concluded with mass sensing result of a microbead.

4.1   Interface Electronics

Interface electronics have been designed for the characterization of sensors. Implementation of electronics was done on printed circuit board (PCB). Designed board gives the opportunity of working both open and closed loop. Moreover, it includes feedthrough elimination electronics for different types of sensors. Let's look into parts of the read-out electronics in detail.

The first part of the interface electronics is the transimpedance amplifier (TIA). The purpose of the TIA is to convert the output current of the resonator to electrical potential. Beside the current to voltage conversion, it also forces output node of the resonator to the ground potential and eliminates the parasitic capacitive effects. Figure 4-1 shows the basic design for TIA.
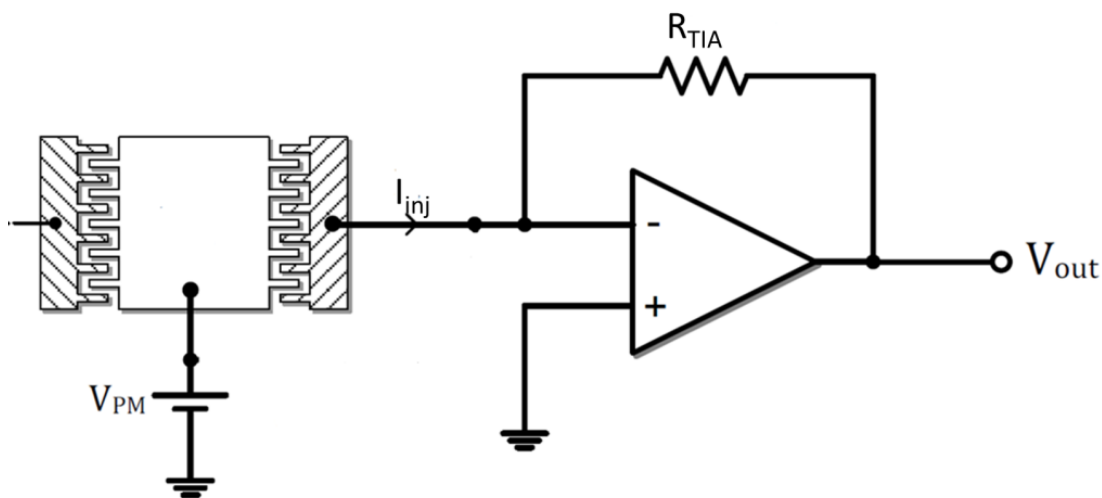
Figure 4-1 Transimpedance amplifier architecture

It is important to select an OPAMP with low input current noise since the injected current from the resonators is at the order of nanoamperes. In order to decrease the current noise, feedback resistance should also be selected as big as possible since the noise current is inversely proportional. These two conditions force us to select an OPAMP with low current noise and high gain-bandwidth product. OPA 656 of Texas Instruments satisfies both conditions. Current noise performance is around 200 fg/$\sqrt{Hz}$ and gain-bandwidth product is close to 1 GHz.

TIA is sufficient for the open loop measurement of resonator. However, for a proper closed loop oscillation more parts are necessary. Barkhausen criteria say that closed loop transfer function should have magnitude of 1 and phase of 0 at oscillation frequency. In order to achieve these two criteria, a voltage comparator and a phase shifter is used. Using voltage comparator as a last stage sustains gain of 1 and phase shifter manipulates the phase response of the system. As previously described an ideal resonator changes phase response from +90 to -90 and at resonance frequency phase response of the resonator is exactly 0. However, feedthrough current prevents the phase change of 180°. Therefore, phase response of the system is no more 0 at resonance frequency. At this point, phase shifter is used to change the phase response of the system to ensure phase of 0 at resonance frequency. Figure 4-2 shows the used phase shifter topology. Changing potentiometer value changes the phase response of the system.
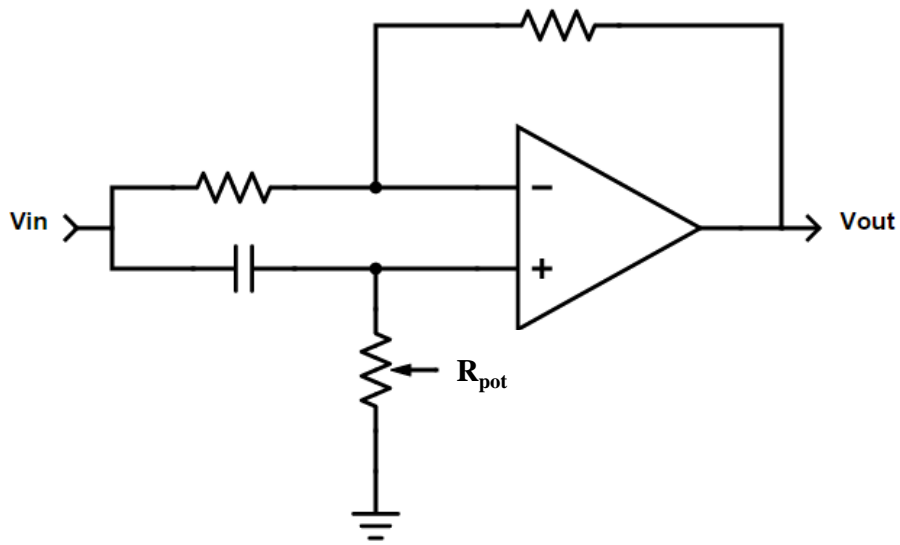
70

Figure 4-2 Phase shifter topology

In this thesis, two different feedthrough elimination methods are suggested and tested. For the resonators that have single sense port applying two opposite phased signal is chosen as feedthrough current elimination method. Therefore creating two signals that have opposite phases is necessary. To have exactly inverted signals, instrumentational amplifiers are chosen since they have high common mode rejection ratio (CMRR). Figure 4-3 shows the topology that implemented on PCB.
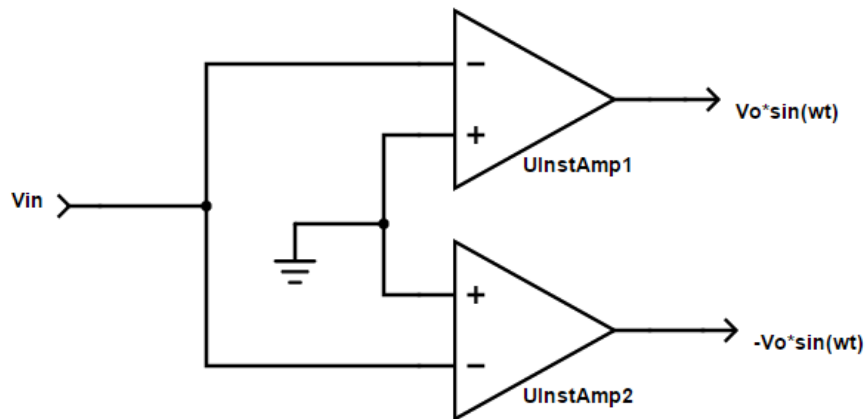
Figure 4-3 Electronics that presents two out-of-phased output by utilizing instrumentation amplifiers

In order to eliminate the feedthrough current of the resonators that have two differential sense ports electronics for voltage subtraction is necessary. Topology in Figure 4.4 is used to subtract the output voltage that obtained from two different sense ports. By changing R1, subtraction ratios of the V1 and V2 can be changed. So that mismatches of feedthrough capacitance between two sense ports and drive ports can be overcome.

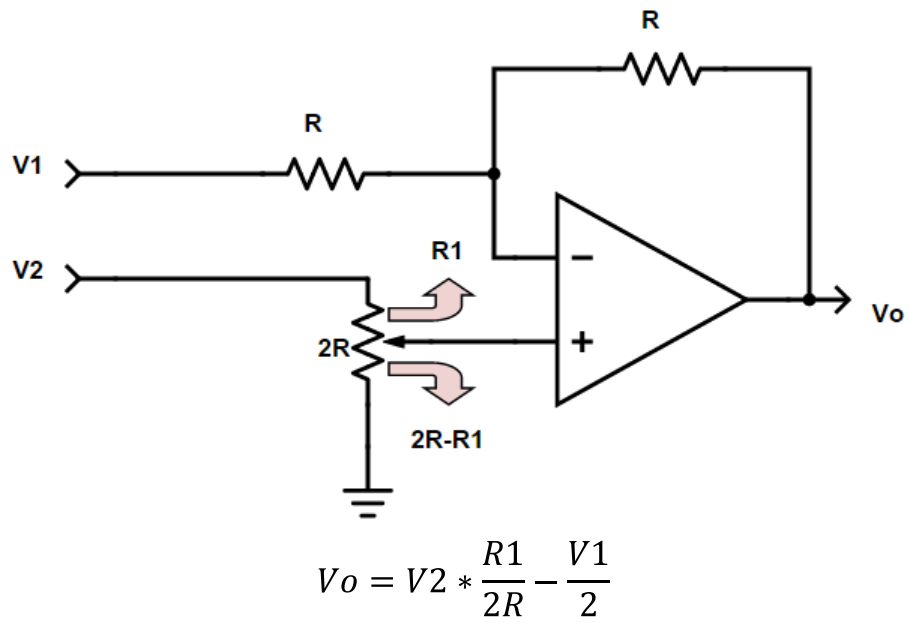$$Vo = V2 * \frac{R1}{2R} - \frac{V1}{2}$$

Figure 4-4 Voltage subtractor electronic that is used to eliminate the feedthrough current

An image of the read-out PCB and device under test can be seen in Figure 4-5.
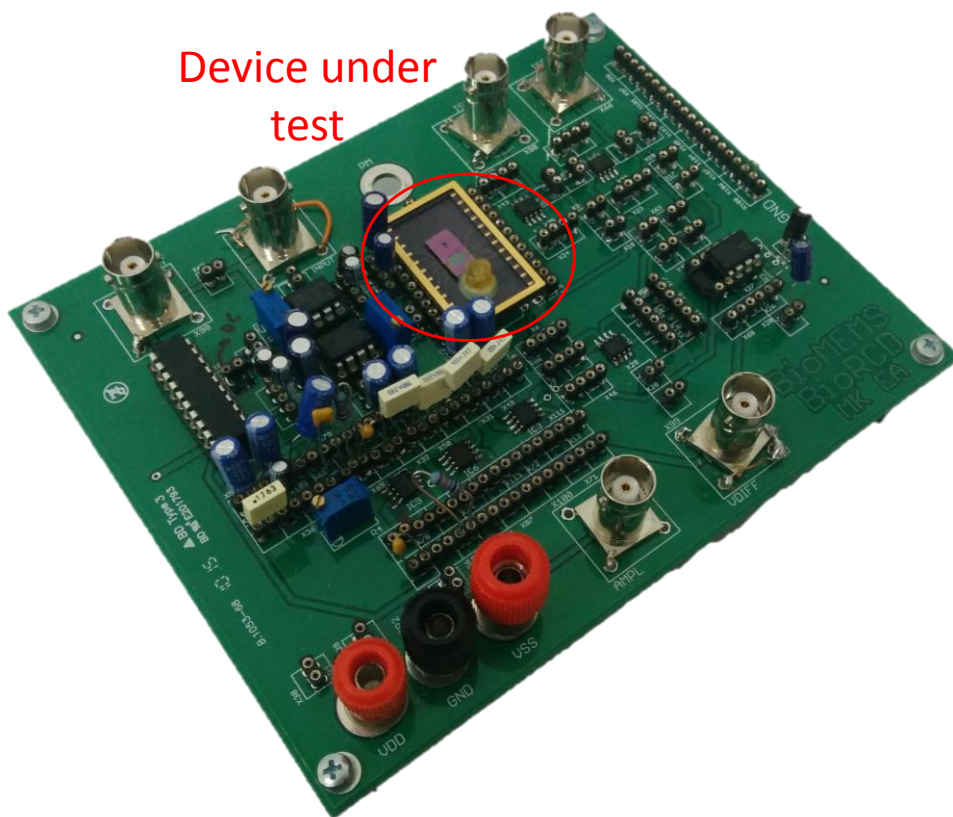

Device under test

Figure 4-5 A closer look of designed electronics with device under test

4.2 Experimental Setup

Image of the test setup is illustrated in Figure 4-6. Probe station is used to take contact from sensor, network analyzer extracts the spectrum analyses of the device under test, and DC supply gives the necessary proof mass bias voltage.
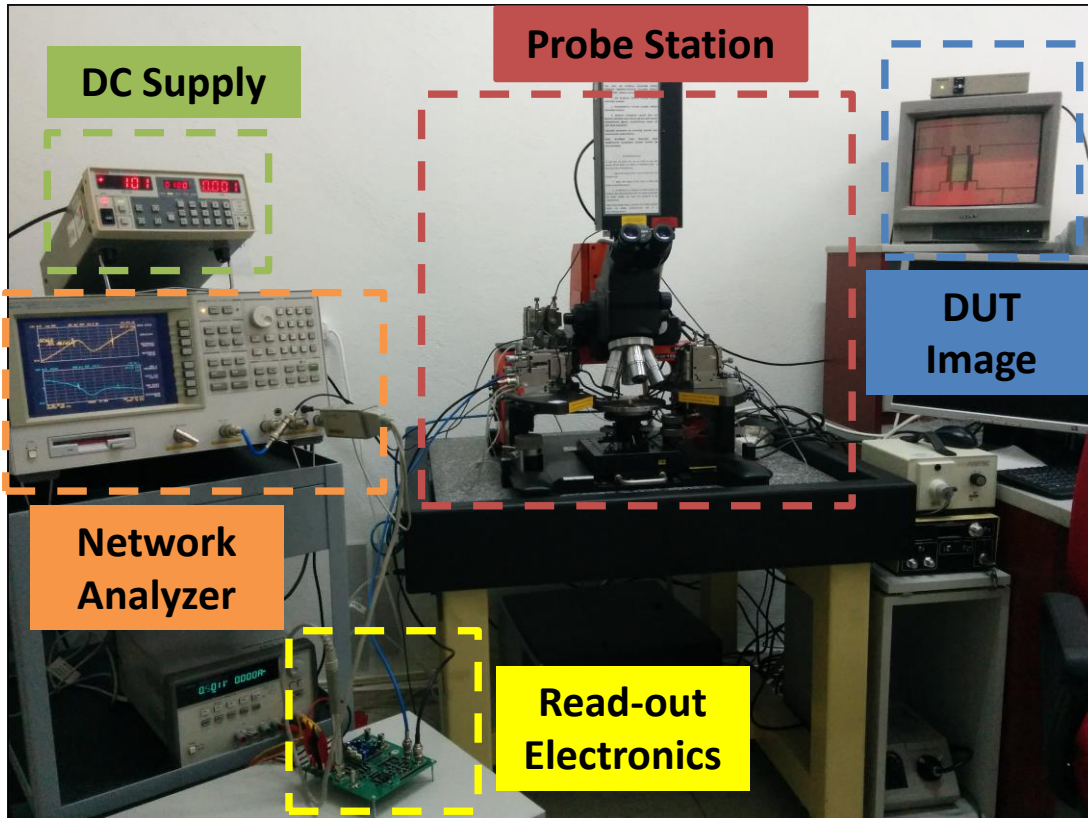

Figure 4-6 Image of the test setup.

Figure 4-7 illustrates the experimental setup for open and close loop operation of the devices. Black path that includes the network analyzer illustrates the open loop test circuitry. Resonator characterization (obtaining quality factor and resonance frequency) is done with this configuration. Actuation signal of the resonator is given from the network analyzer and output current of the resonator converted to voltage and given back to the network analyzer. Basically, network analyzer divides received signal from electronics to the signal that it gives for actuation of the resonator to find response of the system. Since the network analyzer spans the frequency of the actuation signal in the given range, frequency response of the system can be seen in between the desired frequency span. On the other hand blue

path illustrates the closed loop circuitry. There is an additional phase shifter, which manually helps system to lock-in resonance frequency. Oscilloscope is used to observe the waveform of the self-oscillation.
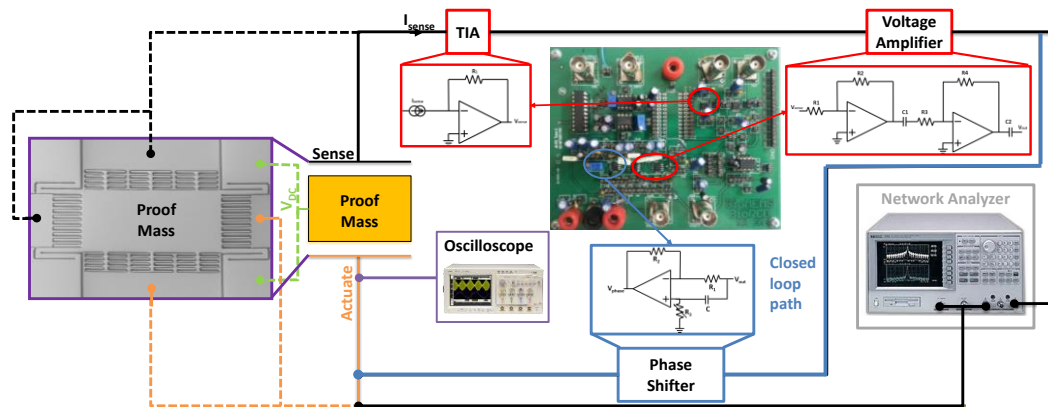

Figure 4-7 Illustration of the experimental setup for open (black line) and close loop (blue line) operation of devices.

4.3 Resonator Characterization

AC responses of all resonators have been measured in air. For each sensor two figures are presented. The first one is direct output of the network analyzer that shows the magnitude and phase response of the overall system. Therefore, this result includes the feedthrough effect. The second figure is the post-processed data with the aim of getting response of the only displacement related output current. To do so results were gathered from the network analyzer in the polar form for both when the sensor is active (DC bias applied) and passive (DC bias not applied). Data that contain only the capacitive feedthrough signal (output signal when DC voltage is not applied on the proof mass) is subtracted from the overall system response (output signal when DC voltage is applied on the proof mass) in vector domain. Basically subtraction of the feedthrough output from the total output is done.

4.3.1 RGCS#1

Figure 4-8 is taken from the network analyzer and it shows the open loop magnitude and phase response of the system with RGCS#1 and TIA. Resonance frequency is around 204.5 kHz. Note that it is impossible to find the quality factor since 3dB drop

does not occur due to feedthrough current effect. Phase drop at resonance frequency is also no more than 2°.
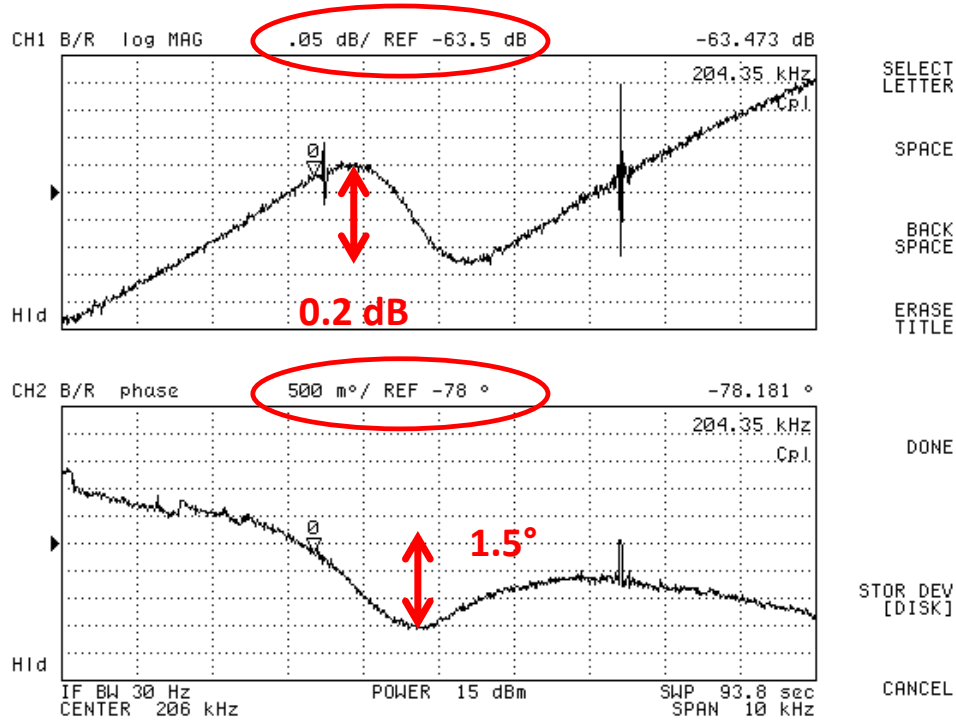

Figure 4-8 Magnitude and phase response of system with RGCS#1 (Screen of the network analyzer)

Figure 4-9 shows the post-processed data that shows only the mechanical response of the resonator. It can be detected from the graph that resonance frequency is 206 kHz and quality factor is 111.
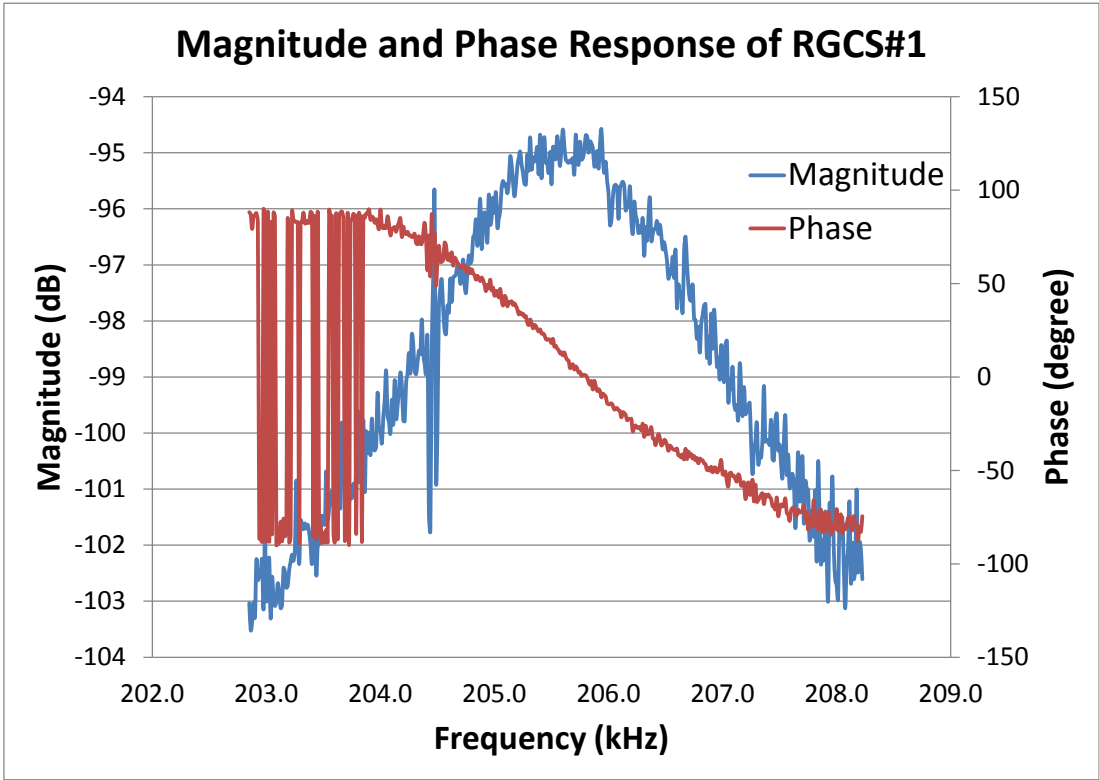
Figure 4-9 Magnitude and phase response of RGCS#1 (post-processed data)

4.3.2   RGCS#2

Figure 4-10 illustrates the magnitude and phase response of the system that consists of RGCS#2 and TIA. Resonance frequency is 226.4 kHz. Quality factor improvisation can also be extracted from the sharpness of the peak, although post-processing is necessary for the exact result. Phase drop of almost 15° simply shows the higher resonator gain against to feedthrough gain compared to RGCS#1.

Figure 4-10 Magnitude and phase response of system with RGCS#2 (Screen of the network analyzer)

Post-processed data in Figure 4-11 can be used to calculate quality factor. Quality factor of the resonator is found as 1131.8.
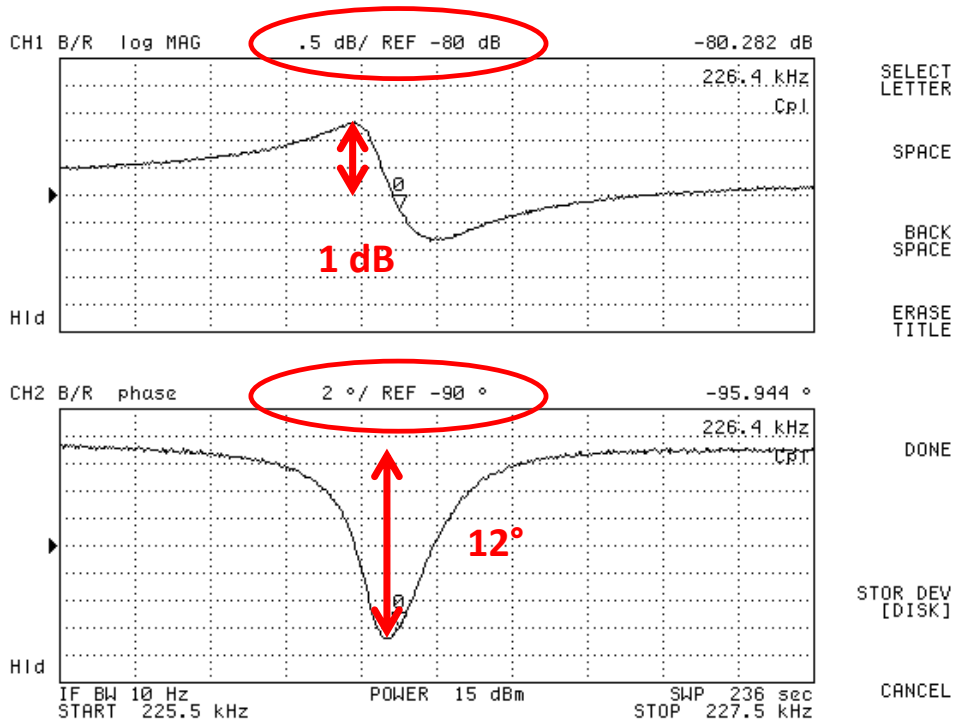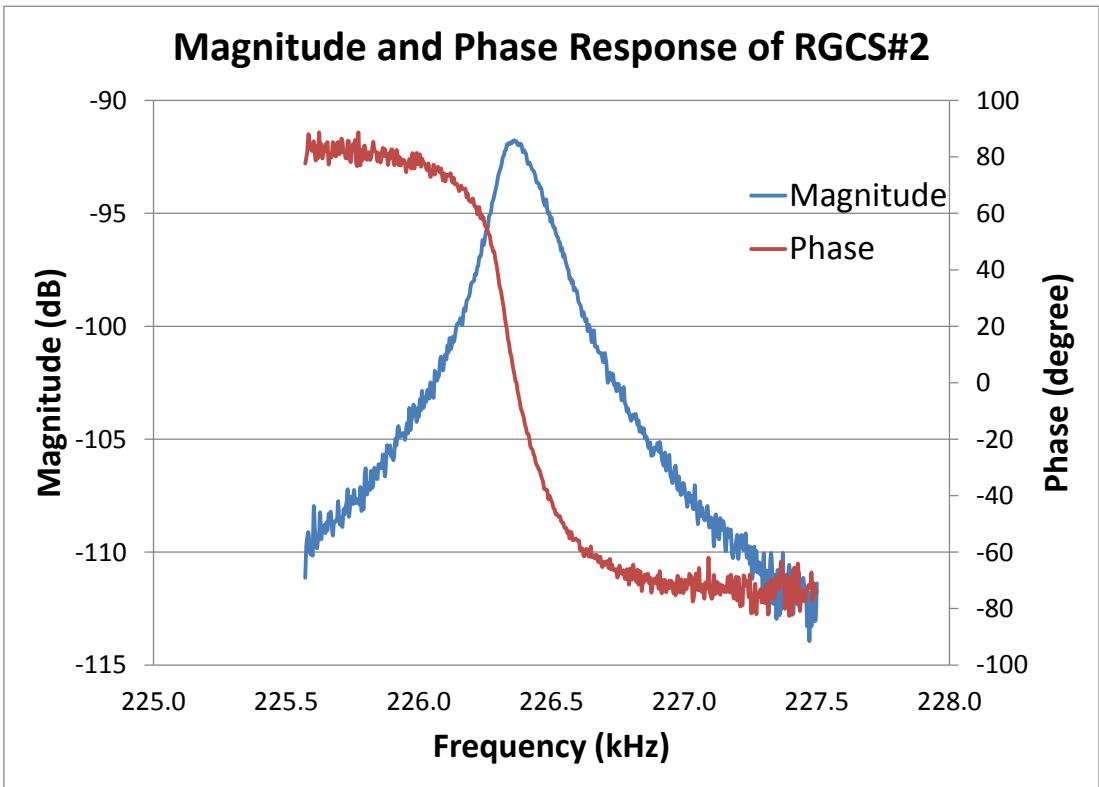
Figure 4-11 Magnitude and phase response of RGCS#2 (post-processed data)

4.3.3 RGCS#3

Figure 4-11 shows the frequency response of the related sensor and TIA system. Resonance frequency is 199 kHz, magnitude peak at resonance is around 8 dB and phase change is around 80°. That means even there is no feedthrough current elimination, feedthrough effect decreases seriously while comparing previous sensors.

Figure 4-12 Magnitude and phase response of system with RGCS#3 (Screen of the network analyzer)

Figure 4-12 illustrates the post processed data that does not include feedthrough current. Quality factor is found as 98. Note that it is expected that RGCS#1 and RGCS#3 have the same resonance frequency and quality factor due to same mass and spring utilization in both sensors. Test results shows that these two sensors have close resonance frequency and quality factor values. Minor differences are caused from fabrication non-uniformities (i.e. Au thickness). One more important point is the peak gain of the sensor. RGCS#3 has gain of -38 dB whereas it is around -90 dB for the previous two sensors.
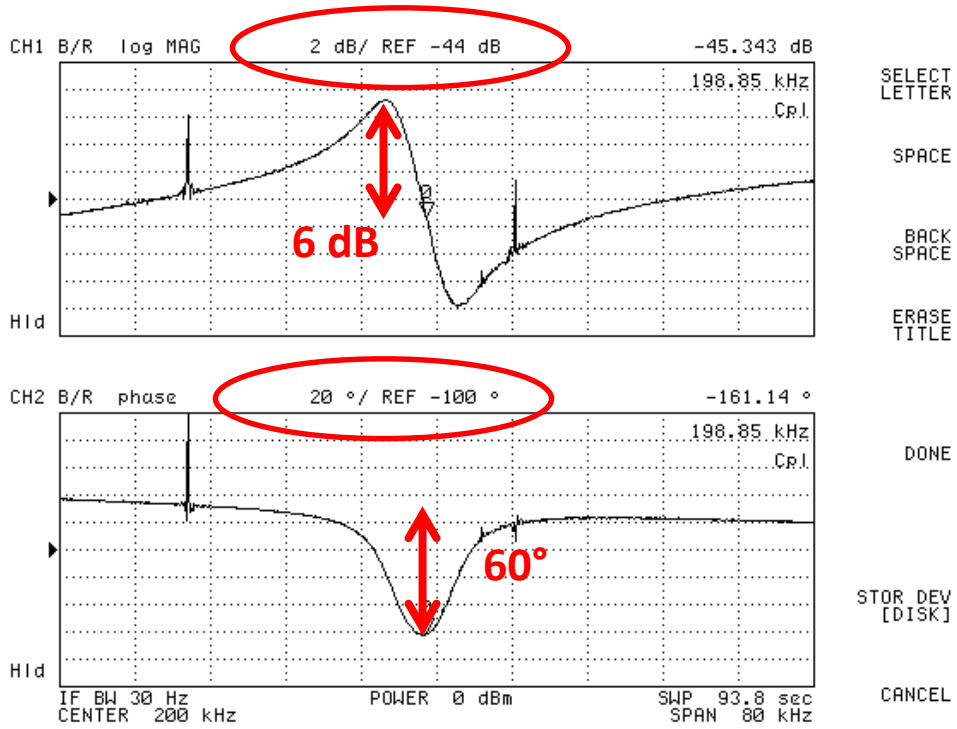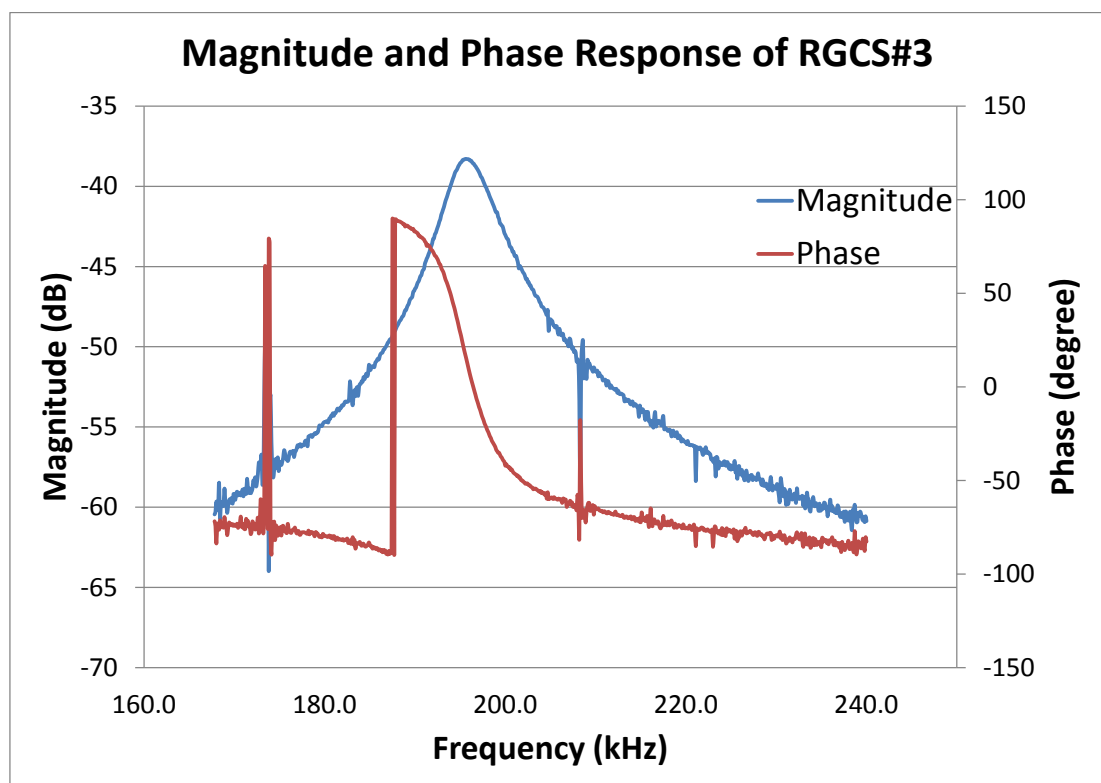

Figure 4-13 Magnitude and phase response of RGCS#3 (post-processed data)

4.3.4 RGCS#4

Purpose of the RGCS#4 is to eliminate feedthrough current by taking difference of opposite-phased output signals. Figure 4-14 shows that effect of feedthrough current on system response is very small comparing previous designs. Phase shift around resonance frequency is more than 100°.
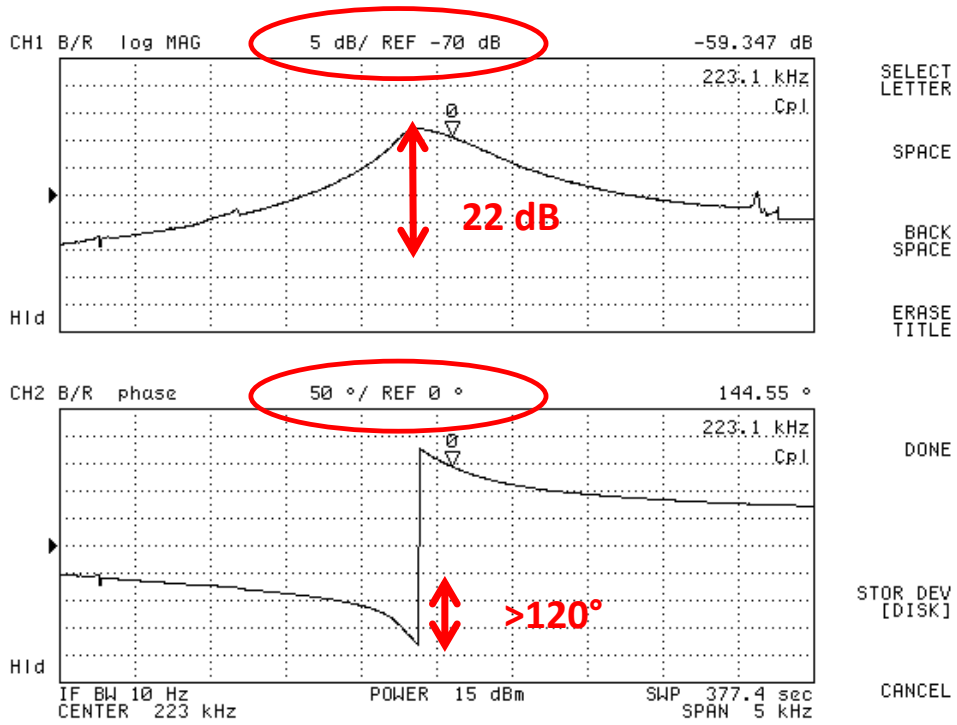
Figure 4-14 Magnitude and phase response of system with RGCS#4 (Screen of the network analyzer)

Figure 4-15 shows the post processed data that exactly eliminates the feedthrough current. Quality factor of this resonator is found as 414.

Figure 4-15 Magnitude and phase response of RGCS#4 (post-processed data)

4.3.5 RGCS#5

RGCS#5 also eliminates the feedthrough current. Figure 4-16 clearly indicates that resonance characteristic is more dominant than feedthrough effect. Similar with RGCS#5 phase change is around 100°.
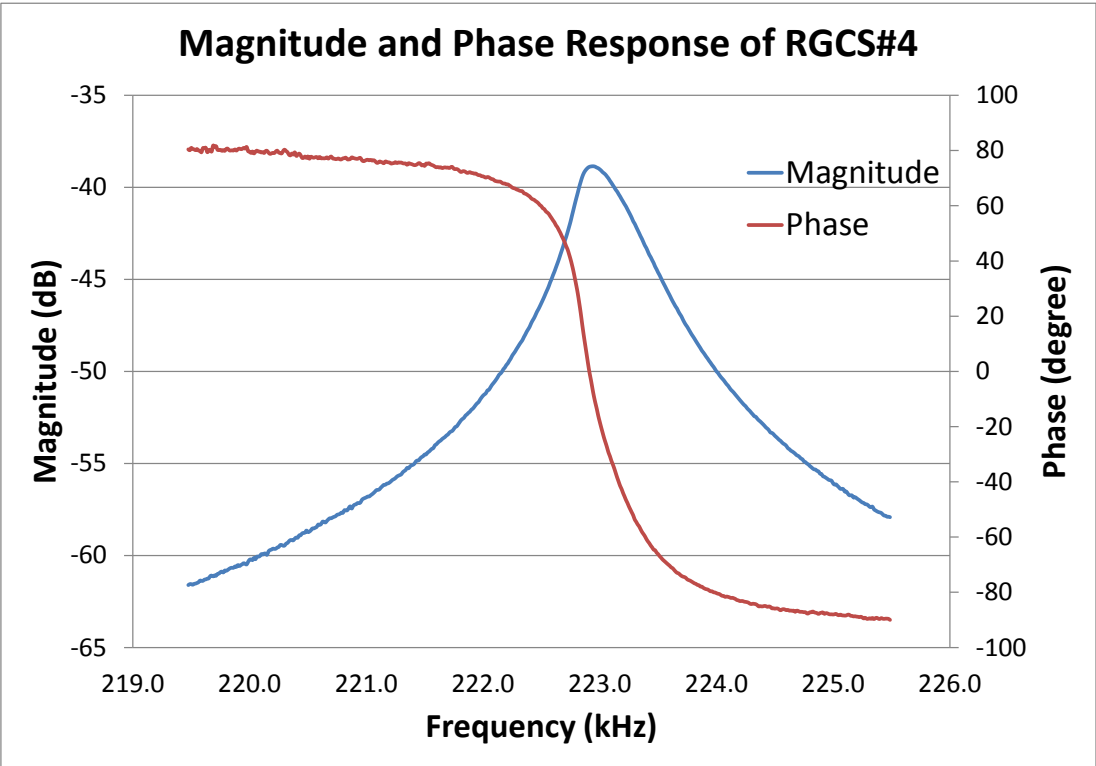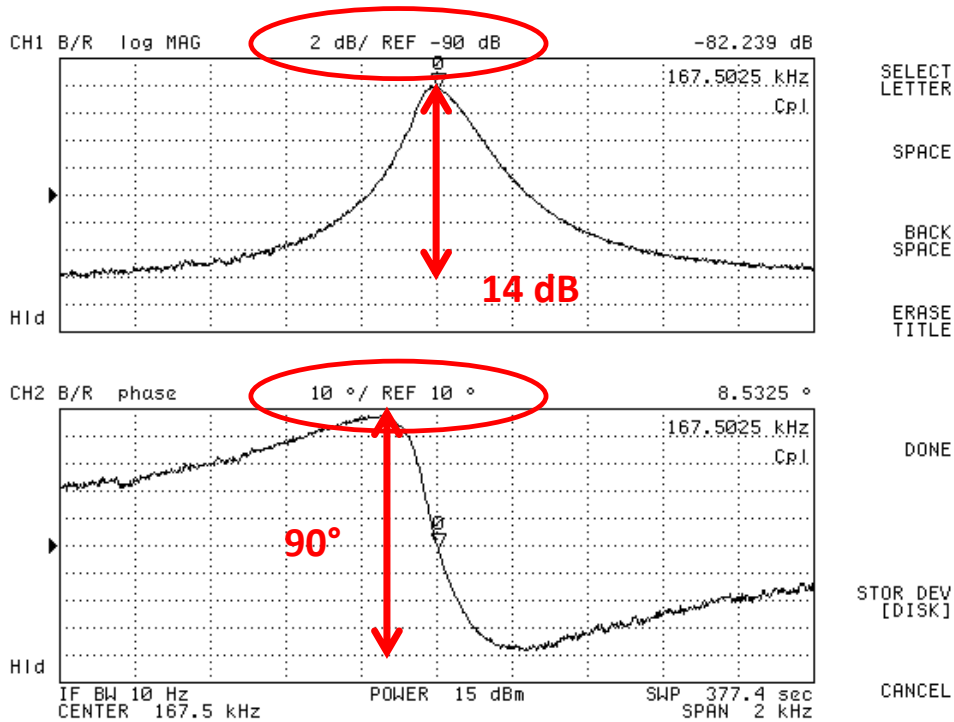
Figure 4-16 Magnitude and phase response of system with RGCS#4 (Screen of the network analyzer)

RGCS#5 is designed to increase the quality factor comparing to RGCS#4. Figure 4-17 shows that quality factor of the resonator is 1015.8. Eventhough the resonance frequency is smaller than the other resonators (the mass is twice of the resonator without finger), it has the highest quality factor. It is also important that the post-processed data that do not include feedthrough current is nearly same with the direct output of the network analyzer that includes the feedback current. This result emphasizes the success of feedthrough current elimination method.
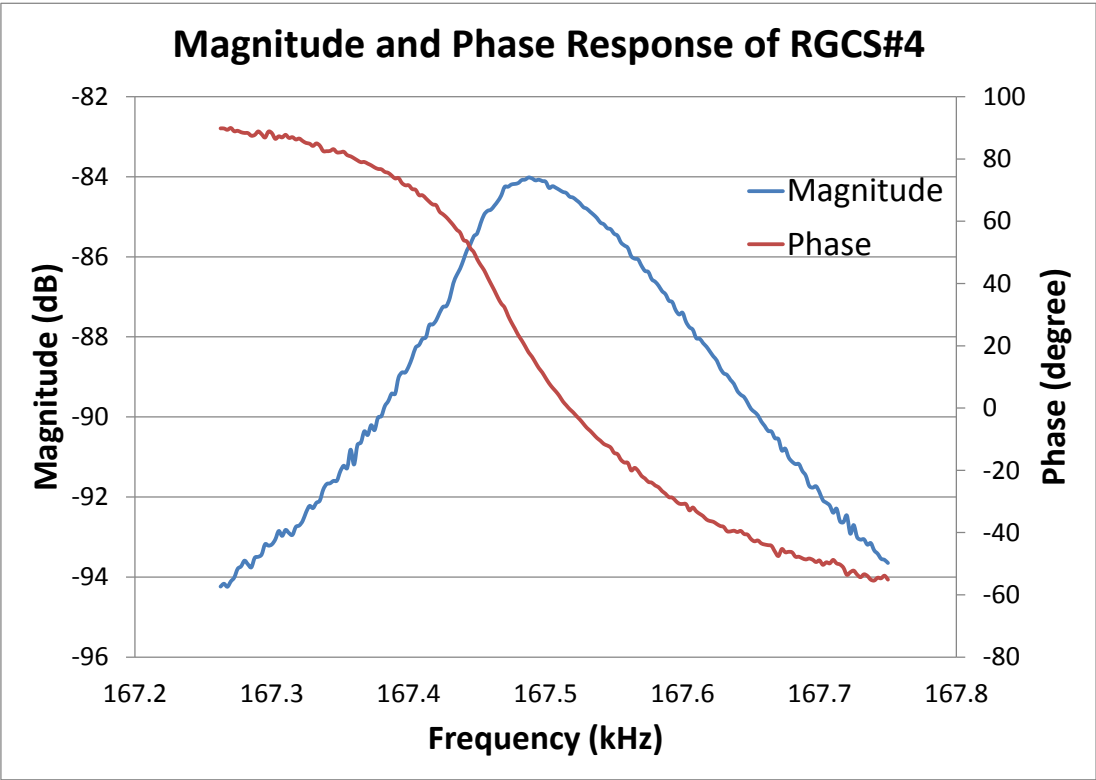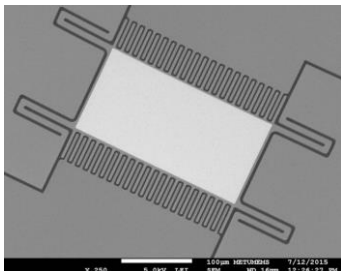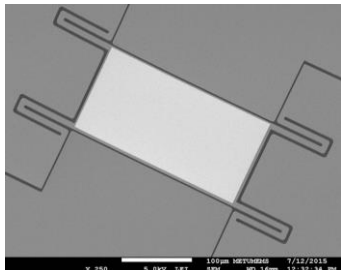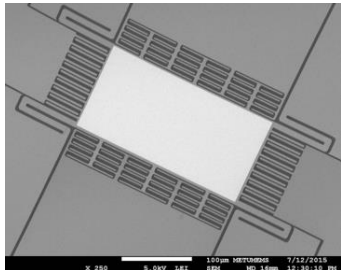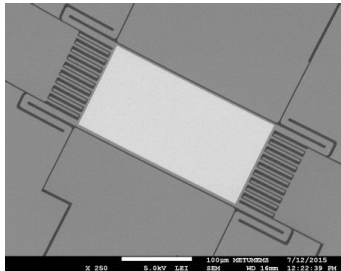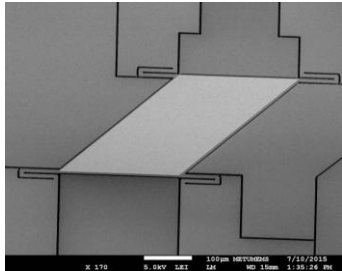
Figure 4-17 Magnitude and phase response of RGCS#4 (post-processed data)

Summary of resonance characterization is presented in the Table 4.1. Maximum gain data is the gain between the input voltage of the resonator and the output voltage of the TIA. Since the resistance of the TIA is 1 MΩ, gain of the resonator (between input voltage and output current) can be found by dividing the given gain to 10^6. However for the RCGS#4 and RCGS#5 voltage subtractor which is established for the feedthrough current elimination adds additional gain. Since the gain of the voltage subtractor is feedthrough current mismatch dependent, maximum gain data for these two sensors is not meaningful for comparison.

Table 4-1 Important measured parameters of different resonator designs.

Sensor	Resonance Frequency	Quality Factor	Max. Gain	Sense Type
RCGS#1	206 kHz	111	-95 dB	Single
RCGS#2	226.4 kHz	1132	-92 dB	Single
RCGS#3	199 kHz	98	-38 dB	Single
RCGS#4	223 kHz	414	NM	Differential
RCGS#5	167.5 kHz	1016	NM	Differential

4.4 Results of feedthrough elimination with dummy signal

For the feedthrough elimination two different methods were investigated in the theory chapter. Success of the differential sense method is already emphasized in the previous section.

The other method that uses two opposite-phased drive signals (one is not for actuation) was tested on previously fabricated sensors [33]. Figure 4.18 shows the tested sensor and related results. There is a dramatic decrease in feedthrough effect when the two feedthrough signals are exactly opposite phased. Effect of phase mismatch, which is theoretically calculated, can be seen from the results (Figure 4-18 c-d). However, it should be noted that, capacitive mismatches in the resonator may raise a problem in achieving exactly opposite phased signals, and hence the feedthrough current may not be perfectly eliminated.
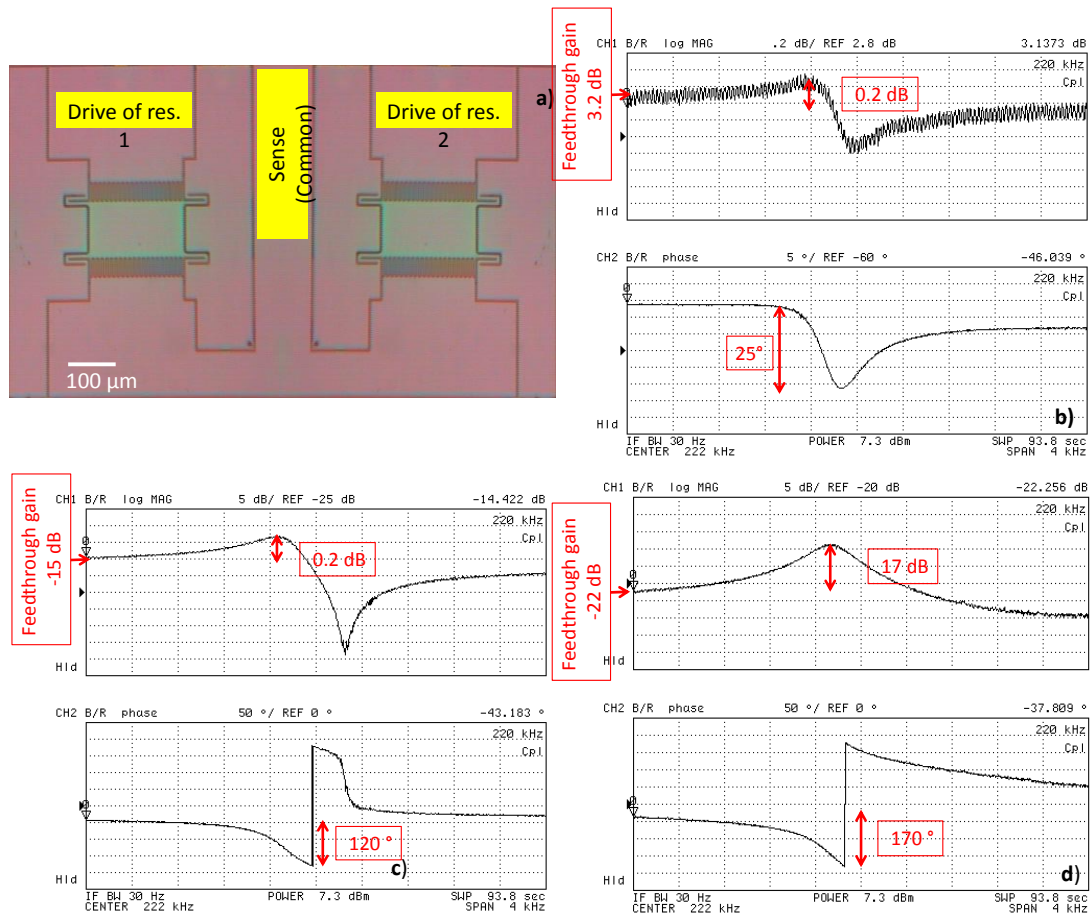
Figure 4-18 AC response of the gravimetric cell sensor (a) under different test conditions is given. In part b) the resonator is driven using single drive electrode and very small resonance peak is observed. In part c) the resonator is driven using differential driving method but phases of drive signals are roughly out-of-phase. Feedthrough current decreased 15 dB and 7dB resonance peak is observed. In part d) phases of drive signals are enforced to be exactly 180° and feedthrough current is decreased 7dB compared to that in part c.

4.5 Mass sensing

In order to test the mass sensitivity, 10 μm (±10%) diameter latex beads of Sigma-Aldrich® were selected as load. The mass density of these beads is very close to the density of water. Mass of a bead is calculated as 550 fg. Figure 4-19 shows the bead placed on the sensor. An RCGS#4 resonator is used for these tests.
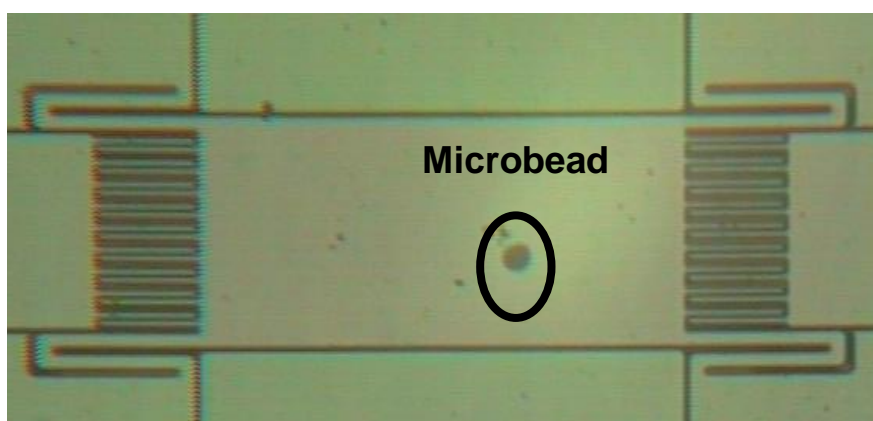
Figure 4-19 Microbead loaded sensor.

Loaded and unloaded resonance frequencies of the sensor were measured. Square of the ratios of these frequencies gives the mass ratios of loaded and unloaded sensor. Figure 4-20 shows the frequency responses of loaded and unloaded sensor. Resonance frequency of the unloaded sensor is 207.34 kHz and the loaded sensor is 207.28 kHz. Mass of the unloaded sensor is calculated as 909 ng including Si, Cr/Au and parylene. In the light of these data, mass change due to the added micro bead is experimentally found as 0.526 ng, corresponding to 60 Hz resonance frequency shift.
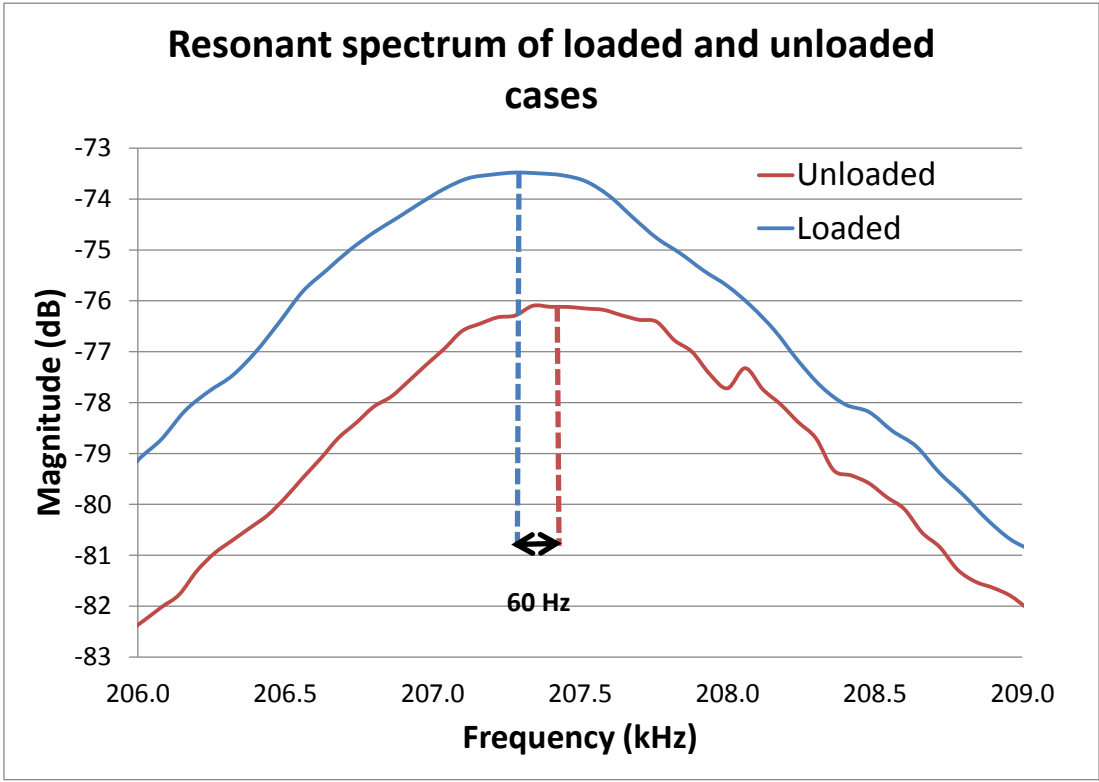
Figure 4-20 Resonant spectrum of loaded and unloaded cases

4.6   In-liquid resonant characterization

It has been already reported that parylene coated lateral resonant structures remains functional in-liquid despite a quality factor drop [22], [32]. Verification of this claim has been done by RCGS#2. Resonant spectra of the sensor were extracted for dry and wet cases. Figure 4-21 & 4-22 show the resonant spectrum comparisons of magnitude and phase, respectively. Quality factors and resonance frequencies are found as 402 and 219.7 kHz for the dry case, and 183 and 219.6 kHz for the wet case.
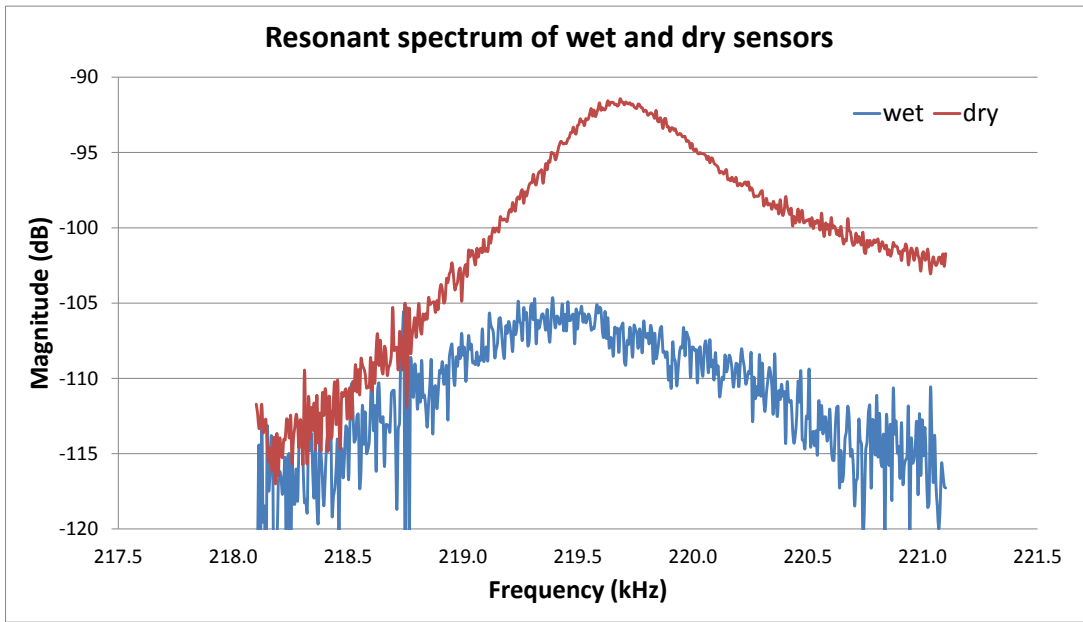
Figure 4-21 Resonant spectrum of wet and dry sensors (magnitude comparison)
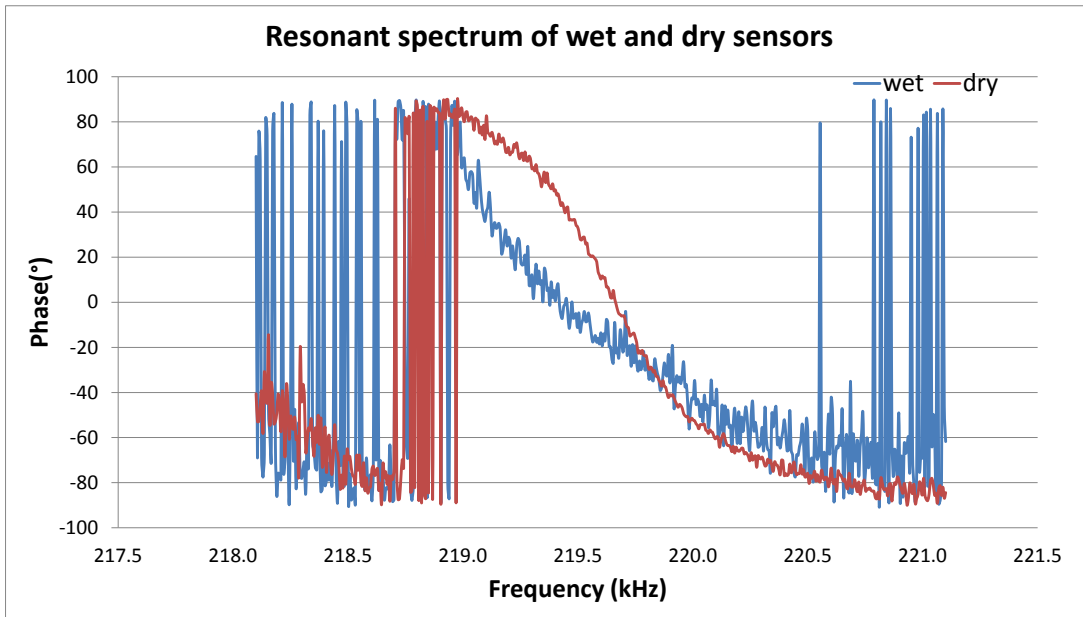
Figure 4-22 Resonant spectrum of wet and dry sensors (phase comparison)

This result concludes the experimental section. Next section concludes the thesis and gives the suggestions of future works.

CHAPTER 5

CONCLUSIONS AND FUTURE WORK

The main objective of this thesis is to enable real-time mass measurement for cell detection applications. Analysis of the benchmark design, which is previously developed in METU BioMEMS research group, is done to emphasize the inefficient comb finger structure that prevents the real-time detection. In the light of these analyses four new sensors are implemented. Proposed sensors did not only improved the quality factor and sensor gain but also eliminated the feedthrough current effect to ensure self-oscillation. RCGS#3 showed that optimizing the sensor gain enables a safe margin for self-oscillation of the resonator. On the other hand, RCGS#5 has less gain but thanks to high quality factor and differential sense ports it is able to detect smaller masses.

Summary of the achieved objectives throughout this study can be listed as follows:

- The theory behind the operation of mechanical resonant structures is studied by using the second order spring, mass and damper systems. Electrostatic capacitive actuation and sensing mechanisms are analyzed and used method in the designs is verified. Feedthrough effect is introduced and two different solutions are proposed.

- Design considerations, including fabrication limitations and application trade-offs are discussed. New device designs are presented. Mathematical analysis of each design is shown and important gain equations of different designs are calculated and drawn on MATLAB for the purpose of comparison.

- Previously proposed fabrication process flow is investigated. Fabrication related problems have been detected and proper solutions have been

proposed. In the light of this analysis, a new process flow is proposed. Device fabrication including SOI, glass and polymer micromachining has been successfully completed.

- A discrete interface circuit, which is implemented with high performance off-the-shelf components on a PCB, is used for resonant characterization of the sensors, realization of feedthrough elimination methods, and closed-loop self-oscillation.

- Resonance characterization experiments in air have been performed. Two order of magnitude gain increase and 10 times quality factor increase have been achieved without increasing the sensor mass.

- Feedthrough current elimination with two methods has been accomplished.

- Mass detection experiments have been done with fabricated sensors. Polystyrene microbeads have been used as mass load. Mass of micro bead is experimentally found as 0.526 ng, corresponding to 60 Hz resonance frequency shift.

- Resonance characterization of sensor in water has been done to verify the effect of parylene layer. The quality factor of measured sensor decreased only to 183 in water, form 402 in air.

- Real time cell detection in liquid environment is enabled in the light of the reported improvements.

Future work on this topic can be summarized as:

- Parylene coating of the wafers were done after the anodic bonding due to high bonding temperature. Therefore, parylene patterning and selective etch could not be done. As a solution, parylene bonding can be used instead of anodic bonding. Both SOI and glass wafers can be parylene coated and parylene can be etched selectively with RIE. Although bonding quality decreases comparing to anodic bonding, this method brings the opportunity of parylene patterning [35].

- In-liquid real-time cell detection tests can be conducted.

- Bioactivation for different analytes can be performed to widen the application areas.

92

- Device can be integrated with the cell separation purposed MEMS devices to increase the detection success.

REFERENCES

[1]   Y. Demircan, "Detection of Imatinib and Doxorubicin Resistance in K562 Leukemia Cells by 3D-Electrode Contactless Dielectrophoresis," Middle East Technical University, 2013.

[2]   R. Bashir, "BioMEMS: State-of-the-art in detection, opportunities and prospects," *Adv. Drug Deliv. Rev.*, vol. 56, no. 11, pp. 1565–1586, 2004.

[3]   R. Bashir, *An Introduction to BioMEMS and Bionanotechnology*. 2005.

[4]   K. Menon, R. A. Joy, N. Sood, and R. K. Mittal, "The Applications of BioMEMS in Diagnosis, Cell Biology, and Therapy: A Review," *Bionanoscience*, vol. 3, no. 4, pp. 356–366, 2013.

[5]   W.-T. Liu, L. Zhu, Q.-W. Qin, Q. Zhang, H. Feng, and S. Ang, "Microfluidic device as a new platform for immunofluorescent detection of viruses.," *Lab Chip*, vol. 5, no. 11, pp. 1327–1330, 2005.

[6]   J. H. Wang, C. H. Wang, W. S. Ling, L. Jheng, S. W. Wang, and G. Bin Lee, "Integrated microfluidic system for HIV detection," *Proc. IEEE Int. Conf. Micro Electro Mech. Syst.*, vol. 1, no. February, pp. 961–964, 2012.

[7]   C. W. Huang, H. T. Hsueh, Y. J. Huang, H. H. Liao, H. H. Tsai, Y. Z. Juang, T. H. Lin, S. S. Lu, and C. T. Lin, "A fully integrated wireless CMOS microcantilever lab chip for detection of DNA from Hepatitis B virus (HBV)," *Sensors Actuators, B Chem.*, vol. 181, pp. 867–873, 2013.

[8]   J. Chen, J. Li, and Y. Sun, "Microfluidic approaches for cancer cell detection, characterization, and separation," *Lab Chip*, vol. 12, no. 10, p. 1753, 2012.

[9]   K. Takahashi, R. Ozawa, H. Oyama, M. Futagawa, F. Dasai, M. Ishida, and K. Sawada, "A CMOS-MEMS-based label-free protein sensor for high-sensitive and compact system," *Tech. Dig. - Int. Electron Devices Meet. IEDM*, pp. 553–556, 2012.

[10]   Z. Mei, S. H. Cho, A. Zhang, J. Dai, T. F. Wu, and Y. H. Lo, "Counting leukocytes from whole blood using a lab-on-a-chip coulter counter," *Proc. Annu. Int. Conf. IEEE Eng. Med. Biol. Soc. EMBS*, pp. 6277–6280, 2012.

[11]   S. Bhattacharya, J. Jang, L. Yang, D. Akin, and R. Bashir, *Rapid Detection of Biological Entities*, vol. 15. 2007.

[12] U. E. Keller, *Chemical Sensors and Biosensors for Medical and Biological Applications*. 1998.

[13] J. Liu and B. Mattiasson, "Microbial BOD sensors for wastewater analysis," *Water Res.*, vol. 36, no. 15, pp. 3786–3802, 2002.

[14] M. J. Heller, a H. Forster, and E. Tu, "Active microeletronic chip devices which utilize controlled electrophoretic fields for multiplex DNA hybridization and other genomic applications.," *Electrophoresis*, vol. 21, no. 1, pp. 157–164, 2000.

[15] R. Bhatia, J. W. Dilleen, a. L. Atkinson, and D. M. Rawson, "Combined physico-chemical and biological sensing in environmental monitoring," *Biosens. Bioelectron.*, vol. 18, no. 5–6, pp. 667–674, 2003.

[16] Ö. S. LAÇIN, "A High Throughput Parylene Microchannel Coulter Counter For Cell Sizing And Cell Counting Applications," Middle East Technical University, 2014.

[17] N. V. Lavrik, M. J. Sepaniak, and P. G. Datskos, "Cantilever transducers as a platform for chemical and biological sensors," *Rev. Sci. Instrum.*, vol. 75, no. 7, pp. 2229–2253, 2004.

[18] H. S. Wasisto, S. Merzsch, A. Waag, E. Uhde, T. Salthammer, and E. Peiner, "Airborne engineered nanoparticle mass sensor based on a silicon resonant cantilever," *Sensors Actuators, B Chem.*, vol. 180, pp. 77–89, 2012.

[19] T. P. Burg, M. Godin, S. M. Knudsen, W. Shen, G. Carlson, J. S. Foster, K. Babcock, and S. R. Manalis, "Weighing of biomolecules, single cells and single nanoparticles in fluid.," *Nature*, vol. 446, no. 7139, pp. 1066–1069, 2007.

[20] S. Olcum, N. Cermak, S. C. Wasserman, K. S. Christine, H. Atsumi, K. R. Payer, W. Shen, J. Lee, A. M. Belcher, S. N. Bhatia, and S. R. Manalis, "Weighing nanoparticles in solution at the attogram scale.," *Proc. Natl. Acad. Sci. U. S. A.*, vol. 111, no. 4, pp. 1310–5, 2014.

[21] K. Park, J. Jang, D. Irimia, J. Sturgis, J. Lee, J. P. Robinson, M. Toner, and R. Bashir, "'Living cantilever arrays' for characterization of mass of single live cells in fluids.," *Lab Chip*, vol. 8, no. 7, pp. 1034–1041, 2008.

[22] E. Bayraktar, D. Eroglu, A. T. Ciftlik, and H. Kulah, "A MEMS based gravimetric resonator for MASS sensing applications," *Proc. IEEE Int. Conf. Micro Electro Mech. Syst.*, pp. 817–820, 2011.

[23] D. Eroglu and H. Kulah, "JMEMS Letters in Liquid Media by Hydrophobic Coating," vol. 20, no. 5, pp. 1068–1070, 2011.

[24] D. Eroglu, E. Bayraktar, and H. Kulah, "A laterally resonating gravimetric sensor with uniform mass sensitivity and high linearity," *2011 16th Int. Solid-State Sensors, Actuators Microsystems Conf. TRANSDUCERS'11*, pp. 2255–2258, 2011.

[25] A. Rahafrooz and S. Pourkamali, "High-frequency thermally actuated electromechanical resonators with piezoresistive readout," *IEEE Trans. Electron Devices*, vol. 58, no. 4, pp. 1205–1214, 2011.

[26] A. Hajjam, A. Rahafrooz, and S. Pourkamali, "Sub-100ppb/??C temperature stability in thermally actuated high frequency silicon resonators via degenerate phosphorous doping and bias current optimization," *Tech. Dig. - Int. Electron Devices Meet. IEDM*, no. 303, pp. 170–173, 2010.

[27] T. Wavering, S. Meller, M. Evans, C. Pennington, M. Jones, R. Van Tassell, K. Murphy, P. Drive, and E. Valdes, "Interferometric Optical Fiber Microcantilever Beam Biosensor," vol. 4200, no. 2000, pp. 10–16, 1872.

[28] B. R. Ilic, S. Krylov, M. Kondratovich, and H. G. Craighead, "Optically actuated nanoelectromechanical oscillators," *IEEE J. Sel. Top. Quantum Electron.*, vol. 13, no. 2, pp. 392–398, 2007.

[29] A. T. Lin, J. E. Lee, J. Yan, and A. A. Seshia, "ENHANCED TRANSDUCTION METHODS FOR ELECTROSTATICALLY DRIVEN MEMS RESONATORS A . T-H . Lin , J . E-Y . Lee , J . Yan , A . A . Seshia Cambridge , UNITED KINGDOM MEASUREMENT THEORY & SETUP," pp. 561–564, 2009.

[30] S. E. Alper, "An Analysis To Improve Stability of Drive-Mode Oscillations in Capacitive Vibratory MEMS Gyroscopes," in *Transducers*, 2011, pp. 817–820.

[31] J. E. Y. Lee and a. a. Seshia, "Parasitic feedthrough cancellation techniques for enhanced electrical characterization of electrostatic microresonators," *Sensors Actuators, A Phys.*, vol. 156, no. 1, pp. 36–42, 2009.

[32] D. Eroglu, "Development of a Resonant Mass Sensor for MEMS Based Cell Detection Applications," Middle East Technical University, 2012.

[33] T. B. TÖRAL, "Development of a High Yield Fabricatiom Process for MEMS Based Resonant Mass Sensors for Cell Detection Applications," MIDDLE EAST TECHNICAL UNIVERSITY, 2014.

[34] Y. H. Cho, A. P. Pisano, and R. T. Howe, "Viscous damping model laterally oscillating microstructures," *J. Microelectromechanical Syst.*, vol. 3, no. 2, pp. 81–87, 1994.

[35]   H. Kim and K. Najafi, "Characterization of low-temperature wafer bonding using thin-film parylene," *J. Microelectromechanical Syst.*, vol. 14, no. 6, pp. 1347–1355, 2005.